공학박사학위논문

Synthesis and Characterization of Ion-conducting Cross-linked Polymeric Materials and Their Applications to Electrolytes and Binders for Lithium Secondary Batteries

이온 전도성을 갖는 가교 고분자 재료의 합성과 분석 및
리튬 이차 전지 전해질, 바인더로의 응용

2023년 2월

서울대학교 대학원

화학생물공학부

홍 동 기

Synthesis and Characterization of Ion-conducting Cross-linked Polymeric Materials and Their Applications to Electrolytes and Binders for Lithium Secondary Batteries

by

Dong Gi Hong

Adviser: Professor Jong-Chan Lee, Ph. D.

Submitted in Partial Fulfillment
of the Requirements for the Degree of
DOCTOR OF PHILOSOPHY

February, 2023

School of Chemical and Biological Engineering
College of Engineering
Graduate School
Seoul National University

이온 전도성을 갖는 가교 고분자 재료의 합성과 분석 및 리튬 이차 전지 전해질, 바인더로의 응용

Synthesis and Characterization of Ion-conducting Cross-linked Polymeric Materials and Their Applications to Electrolytes and Binders for Lithium Secondary Batteries

지도교수 이 종 찬 박사

이 논문을 공학박사학위 논문으로 제출함.

2023년 2월

서울대학교 대학원

화학생물공학부

홍 동 기

홍동기의 박사학위논문을 인준함.

2023년 2월

위원장 (인)

부위원장 (인)

위 원 (인)

위 원 (인)

위 원 (인)

Abstract

Synthesis and Characterization of Ion-conducting Cross-linked Polymeric Materials and Their Applications to Electrolytes and Binders for Lithium Secondary Batteries

홍 동 기 (Dong Gi Hong)

공과대학 화학생물공학부 (Chemical and Biological Engineering)

고분자 합성 전공 (Polymer Synthesis)

The Graduate School

Seoul National University

This study presents synthesis and characterization of ion-conducting cross-linked polymeric materials and their applications to electrolytes and binders for lithium secondary batteries. Firstly, cross-linked solid polymer electrolytes (SPEs) based on ion-conducting poly(ethylene glycol) (PEG), flexible polysiloxane, and anion-trapping boron cross-linker (BPC) were prepared *via* thiol-ene click reaction for lithium metal batteries. Various thermal and electrochemical properties of SPEs were systematically investigated by varying the content of BPC. Thermally stable free-standing SPE systems could be obtained due to the cross-linked structure, while relatively high ionic conductivity of about 1.3×10^{-4} S cm^{-1} at 60 °C was obtained at the same time by the flexible polysiloxane moiety. The boron

moiety in BPC could increase the lithium ion transference number compared to the corresponding boron-free SPE due to the anion-trapping capability of boron atom. The formation and growth of lithium dendrites were effectively suppressed by the anion-trapping capability and mechanically stable cross-linked structure of the SPE.

Secondly, a cross-linked polyphosphazene-based polymeric material was prepared using NH_3-neutralized poly[bis(4-carboxyphenoxy)phosphazene] (PCPP-NH_3) as the base polymer and poly(ethylene glycol) bisamine (PEG-NH_3) as a cross-linker for use as a silicon (Si) anode binder in lithium-ion batteries. PCPP was prepared by two step polymer modification reactions from poly(dichlorophosphazene). When an optimum amount of PEG-NH_3 (7.5 wt% of PCPP-NH_3) was used as the cross-linker, the resulting cross-linked polyphosphazene exhibited the highest glass transition temperature, elastic modulus, and peeling force values. The battery performance of the cells with the Si anode fabricated with this cross-linked polyphosphazene-based binder was found to be better than that of cells with Si anodes fabricated with PAA binder. The better performance of the cell with the polyphosphazene-based binder was ascribed to the composition and structure of the binder material: the flexible polyphosphazene backbone, carboxylic acid group with hydrogen bonding

ability, and the cross-linked network structure maintained the electrode structure during charge/discharge cycling of the cell. Furthermore, the ion-conducting PEG moieties increased ion transfer conductivity inside the Si anode.

Keywords: Cross-linked polymer, solid polymer electrolytes, anion-trapping, silicon anode binder, polyphosphazene, lithium metal batteries, lithium-ion batteries

Student Number: 2017-27567

TABLE OF CONTENTS

Abstract ..... **i**

List of Figures ..... **vii**

List of Tables ..... **xii**

Chapter 1

Introduction

1.1. Challenges of Lithium Rechargeable Batteries **2**

1.2. Solid Polymer Electrolytes in Lithium Metal Batteries **4**

1.3. Polymeric Binders for Silicon Anodes **5**

1.4. Motivation **6**

1.5. References **8**

Chapter 2

Solid Polymer Electrolytes Based on Polysiloxane with Anion-Trapping Boron Moieties for All-Solid-State Lithium Metal Batteries

2.1. Introduction **19**

2.2. Experimental **22**

2.3. Results and Discussion **30**

2.4. Conclusions **40**

2.5. References **41**

Chapter 3

Ion-Conducting Cross-linked Polyphosphazene Binders for High-Performance Silicon Anodes in Lithium-Ion Batteries

3.1. Introduction **85**

3.2. Experimental **89**

3.3. Results and Discussion **96**

3.4. Conclusions **104**

3.5. References **106**

Abstract in Korean **135**

List of Figures

Figure 1.1. Anion-trapping cross-linked solid polymer electrolytes for lithium metal battery and ion-conductive cross-linked polyphosphazene binder for Si anode. 17

Figure 2.1. The synthetic scheme of (a) BPTS and (b) BPC. 57

Figure 2.2. GPC profile of BPTS. 58

Figure 2.3. Repeating units and end group of BPTS. 59

Figure 2.4. ^{1}H NMR spectrum of BPTS. 62

Figure 2.5. ^{1}H NMR spectra of BPC and PEGMA. 63

Figure 2.6. Preparation of solid polymer electrolytes based on hyper-branched polysiloxane (BPTS) and anion-trapping boron cross-linker (BPC). 64

Figure 2.7. FT-IR spectra of CSPE-Bs and PE-B0 in the range of 2750–1600 cm^{-1}, (b) photograph of free-standing CSPE-B60. 65

Figure 2.8. FT-IR spectra of BPTS, BPC, allyl PEG, and CSPE-B60 in the range of 2650–1600 cm^{-1}. 66

Figure 2.9. SEM and EDS images of CSPE-B60. 67

Figure 2.10. Preparation of CSPE-BFs. 68

Figure 2.11. (a) DSC thermograms of CSPE-Bs and PE-B0 ($[Li^{+}]$/[EO unit]

= 0.07). (b) Glass transition temperatures of CSPE-B60 with various lithium salt concentrations. (c) Ionic conductivities of CSPE-B60 with various lithium salt concentrations at 30 °C and 60 °C. (d) Ionic conductivities of CSPE-Bs at various temperatures ([Li^+]/[EO unit] = 0.07). 69

Figure 2.12. TGA curves of (a) CSPE-Bs with PE-B0 and (b) CSPE-BFs. 70

Figure 2.13. Linear sweep voltammogram of (a) CSPE-Bs and (b) CSPE-BFs at 60 °C with a scan rate of 1 mV s^{-1}. 71

Figure 2.14. Chronoamperometric curves of (a) Li/CSPE-B50/Li cell, (b) Li/CSPE-B60/Li cell, and (c) Li/CSPE-BF40/Li cell (inset: corresponding electrochemical impedance spectra before and after polarization). 72

Figure 2.15. t_{Li^+} of polymer electrolytes at 60 °C. 73

Figure 2.16. Components of CSPEs with different PEG chain length. 74

Figure 2.17. (a) Ionic conductivities of CSPEs with different PEG chain length at various temperatures. (b) t_{Li^+} values of CSPEs with different PEG chain length at 60 °C. 76

Figure 2.18. (a) Specific discharge capacity and Coulombic efficiency of the V_2O_5/CSPE/Li cells cycled at 60 °C with a rate of 0.1 C.

(b) Surface SEM images of bare lithium metal before cycling and those of the cells with CSPE-BF40, CSPE-B50, and CSPE-B60, respectively, after 50 cycles. XPS spectra of (c) N 1s and (d) F 1s from the lithium metal anode of the V_2O_5/CSPE/Li cells with CSPE-B60 and CSPE-BF40 after cycling for 50 cycles at 60 °C with a rate of 0.1 C. 77

Figure 2.19. Nyquist plot of V_2O_5/CSPE-B60/Li cell at 60 °C. 78

Figure 2.20. Ionic conductivities of CSPE-BF40, CSPE-B50, and CSPE-B60 at various temperatures ($[Li^+]$/[EO unit] = 0.07). 79

Figure 2.21. Storage modulus profiles of CSPE-B50 and CSPE-B60. 80

Figure 2.22. Specific discharge capacity of the V_2O_5/PP separator-LE/Li cells cycled at 60 °C with a rate of 0.1 C. (LE: 1M $LiPF_6$ EC/DMC, 1:1 v/v) 81

Figure 2.23. Charge-discharge profiles of V_2O_5/CSPE-B60/Li cell cycled at 60 °C with various rates. 82

Figure 2.24. XPS spectra of (a) C 1s, (b) O 1s, and (c) S 2p from the lithium metal anode of the V_2O_5/CSPE/Li cells with CSPE-B60 and CSPE-BF40 after cycling for 50 cycles at 60 °C with a rate of 0.1 C. 83

Figure 3.1. The illustration for lithiation/delithiation of Si anode with ion-

conducting cross-linked poly[bis(4-carboxyphenoxy)phosphazene] binder. 118

Figure 3.2. GPC profile of PEPP. 119

Figure 3.3. Schematic illustration for the preparation of binder solution and the formation of binders with cross-linked structures (PCG-Xs). 120

Figure 3.4. Synthetic scheme of (a) PEPP and (b) PCPP. 121

Figure 3.5. (a) ^{1}H NMR spectrum and (b) ^{31}P NMR spectrum of PEPP. 122

Figure 3.6. (a) ^{1}H NMR spectrum and (b) ^{31}P NMR spectrum of PCPP. 123

Figure 3.7. FT-IR spectra of PEPP and PCPP in the range of 4000–600 cm^{-1}. 124

Figure 3.8. DSC thermograms of (a) PEPP and (b) PCPP. 125

Figure 3.9. TGA curves of PEPP and PCPP. 126

Figure 3.10. FT-IR spectra of PEPP, PCPP, *i*-PCG-7.5, and PCG-7.5 in the range of 1800–1200 cm^{-1}. 127

Figure 3.11. DSC thermograms of PCG-Xs. 128

Figure 3.12. (a) Elastic moduli of PCG-Xs. (b) Load–displacement curves and (c) SAICAS data of Si anodes with PCG-Xs. 129

Figure 3.13. (a) Specific discharge capacity of the Si half-cells with PCG-Xs and PAA binders cycled at a rate of 0.2 C after two activation cycles at 0.05 C. (b) Rate capability test of cells with PCG-7.5 and PAA binders. (c) Linear fits for the cathodic peak currents versus the square root of the scan rates for anodes with PCG-7.5 and PAA binders. 130

Figure 3.14. (a) Ionic conductivities and (b) electrolyte uptake of PCG-Xs and PAA at 25 °C. (c) Electrochemical stability of PCG-Xs at 25 °C. 131

Figure 3.15. Nyquist plots of the cells with Si anode using PAA and PCG-7.5 binders (a) before and (b) after cycling. 132

Figure 3.16. Cyclic voltammetry curves of the cells with Si anode using (a) PAA and (b) PCG-7.5 binders at different scan rates. 133

Figure 3.17. Top-view SEM images of Si anodes with (a) PAA and (b) PCG-7.5 binders before cycling. Top-view SEM images of Si anodes with (c) PAA and (d) PCG-7.5 binders after 50 cycles. Cross-sectional SEM images of Si anodes with (e) PAA and (f) PCG-7.5 binders before cycling. Cross-sectional SEM images of Si anodes with (g) PAA and (h) PCG-7.5 binders after 50 cycles. 134

List of Tables

Table 2.1. Sample composition and properties of CSPE-Bs and CSPE-BFs 56

Table 3.1. Preparation of aqueous binder solutions and properties of the binder materials (PCG-Xs) 117

Chapter 1

Introduction

1.1 Challenges of Lithium Rechargeable Batteries

After the industrial revolution, the population explosion and the developments of electronic devices have resulted in the dramatic increase in energy consumption. [1-3] Lithium rechargeable batteries have been extensively investigated for several decades along with the growth of portable devices, electric vehicles, and energy storage system. [4, 5] The conventional lithium rechargeable batteries consisting of lithium metal oxide cathode, graphite anode, and a liquid electrolyte with polyolefin-based separator have been continuously researched and developed to increase energy density since the first commercialization of lithium-ion batteries in 1991. [6] However, the current battery system composed of the lithium metal oxide cathode and the graphite anode does not satisfy the demand for higher capacity and safety. [7] As a result, interest in next-generation battery systems with higher energy density and safety is increasing day by day. In order to achieve high energy density, it is necessary to use electrode materials with high specific capacity such as lithium metal anode and silicon anode. [8]

Lithium metal batteries (LMBs) have been substantially studied for several decades due to the advantages of lithium metal such as extremely high theoretical capacity (3860 mAh g^{-1}), low density (0.58 g cm^{-3}), and lowest negative electrochemical potential (−3.040 V vs. hydrogen standard electrode). [9, 10] However, the practical application of LMBs is hampered

by several disadvantages of the lithium metal as an anode material such as unstable solid electrolyte interface (SEI) layer and lithium dendrite formation. [11-13] The unstable SEI layer leads to the continuous electrolyte consumption and low Coulombic efficiency, resulting in poor long-term stability of LMBs. [14] The lithium dendrite formation, which is regarded as the main cause of the battery failure, results in the lithium metal penetration through separator, internal short-circuit of the battery, and finally thermal runaway. [13]

Graphite-based anode materials, which are currently used in commercial lithium-ion batteries (LIBs), are limited in achieving high energy density because of a relatively low theoretical capacity (372 mAh g^{-1} based on LiC_6). [15] On the other hand, silicon (Si) has been regarded as a promising anode material due to its high theoretical capacity (4,200 mAh g^{-1}), low discharge potential (~0.3 V vs. Li/Li^+), and natural abundance. [16-18] However, inherent huge volume change during the charge/discharge process (up to 300%), which causes degradation of electrode structure and formation of thick solid electrolyte interface (SEI) layer, hinders the practical application of Si anodes. [19, 20] Various strategies to mitigate volume change of Si by processing Si into yolk-shell nanoparticles, [21, 22] nanowires, [23, 24] and nanoporous structure [25, 26] have been reported. Although the nanostructured Si anodes have been demonstrated to reduce Si volume expansion to some extent, the commercialization of these materials is

challenging because the production is costly and difficult to scale-up. [27]

1.2 Solid Polymer Electrolytes in Lithium Metal Batteries

To solve the aforementioned problems of LMBs, various strategies such as adding electrolyte additives, [28] forming artificial SEI layer, [29] and using gel or solid electrolytes. [30-32] In particular, solid polymer electrolytes (SPEs), which are composed of polymer matrix and lithium salts in the absence of any liquid components, have advantages such as low flammability, flexibility, and dimensional stability. [33] As compared to inorganic ceramic electrolytes, SPEs possess several advantages including ease of processing, flexibility, and strong adhesion to electrodes. [34] Recent researches on SPEs focus on the development of SPEs for practical applications in LMBs requiring sufficient ionic conductivity, sufficient mechanical properties, thermal stability, and wide electrochemical window. [35-37]

Among the SPEs, poly(ethylene oxide) (PEO) based SPEs have been extensively investigated due to their Li^+ solvating ability and ion-conducting nature of ethylene oxide units. [38] However, since PEO-based electrolytes suffer from the low ionic conductivity by crystalline structure of PEO, studies to improve ionic conductivity by suppressing the crystallization of PEO have been reported. [39, 40] In addition, anion-trapping moieties can increase lithium ion transference number (t_{Li^+}) by reducing movement of anions. The

introduction of anion-trapping moieties in the SPEs not only reduces the concentration polarization, thereby lowering internal resistance of battery and improving cell performance, [41] but also inhibits the formation and growth of lithium dendrites. [42, 43]

1.3 Polymeric Binders for Silicon Anodes

It has been demonstrated that functional polymeric binders can effectively mitigate the volume expansion of Si and maintain the structural integrity of the Si anode. [44] Poly(vinylidene fluoride) (PVDF), which is a commercial binder in LIBs, is difficult to maintain structural stability because it cannot sufficiently interact with the Si particle surface. [18] Polymeric materials having a large amount of polar functional groups such as poly(acrylic acid) (PAA), [45] carboxymethyl cellulose (CMC), [46] and polysaccharides [47, 48] have been demonstrated to show strong binding strength with silanol groups on the surface of the Si particles. The hydrogen bonding between silanol groups on Si particles and hydroxyl/carboxylate functional groups in the binder is beneficial to maintaining a conductive network from the huge volume change of Si. [15, 49] In particular, the binders containing large amounts of polar functional groups are usually soluble in water, and the aqueous binders have several advantages as follows. Since they use a cheap solvent, water, the process cost is low, and they are more eco-friendly than

binders using toxic organic solvents such as N-methyl-2-pyrrolidone (NMP). [50, 51] In addition, since water has a much lower boiling point than NMP, energy can be saved in the electrode manufacturing process. [52] One of the most important advantages of aqueous binders is that they are not swelled in liquid electrolytes such as carbonates, so it is easy to tolerate the volume change of Si particles during cell cycling. [45, 53]

1.4 Motivation

Based on the understanding of the current problems in lithium secondary batteries, especially lithium metal batteries and silicon anodes, and the required properties of polymeric materials in the battery system, we designed and synthesized cross-linked polymeric materials including anion-trapping solid polymer electrolytes and ion-conducting polyphosphazene-based binders (Figure 1.1). The structure-property relationships of the prepared cross-linked polymeric materials were investigated systematically and the electrochemical performance of the lithium metal batteries and silicon anode with the prepared polymeric materials was evaluated.

Firstly, cross-linked solid polymer electrolytes (SPEs) with anion-trapping ability due to boron moieties were investigated. sp^2 boron can trap anions through an empty p orbital, and a polymer cross-linker containing boron moieties was synthesized to utilize the anion-trapping ability of boron.

Polysiloxane is a very flexible polymer, and when used as a matrix of polymer electrolytes, it can improve ionic conductivity by increasing the chain mobility of the electrolyte. SPEs were prepared by thiol-ene click reaction of thiol in polysiloxane and double bonds in boron cross-linker and allyl PEG. The thermal and electrochemical properties of the SPEs according to the content of the boron cross-linker and the degree of crosslinking were investigated. The batteries with the prepared SPEs showed excellent cell performance due to the improved ion conductivity with the help of polysiloxane and the anion-trapping effect of boron moieties.

Secondly, ion-conducting cross-linked Si anode binders based on polyphosphazene were prepared and their electrochemical properties were studied. Polyphosphazene is a macromolecule that has a flexible main chain and various organic side groups. To utilize polyphosphazene as the binder for the Si anode, polyphosphazene having two carboxylic acids per repeating was synthesized. In addition, *in-situ* cross-linked binders were prepared in the electrode drying process using PEG bisamine to provide additional ion conductivity and improve mechanical properties. Thermal, mechanical, and electrochemical properties were investigated according to the cross-linking density and PEG content. Si anodes with polyphosphazene-based cross-linked binders exhibited excellent cell performance due to cross-linked structure and lithium ion conductivity.

1.5 References

[1] J.M. Tarascon, M. Armand, Issues and challenges facing rechargeable lithium batteries, Nature 414(6861) (2001) 359-367.

[2] M. Armand, J.M. Tarascon, Building better batteries, Nature 451(7179) (2008) 652-657.

[3] T. Kim, W. Song, D.-Y. Son, L.K. Ono, Y. Qi, Lithium-ion batteries: outlook on present, future, and hybridized technologies, Journal of Materials Chemistry A 7(7) (2019) 2942-2964.

[4] D. Lin, Y. Liu, Y. Cui, Reviving the lithium metal anode for high-energy batteries, Nature Nanotechnology 12(3) (2017) 194-206.

[5] M.M. Thackeray, C. Wolverton, E.D. Isaacs, Electrical energy storage for transportation—approaching the limits of, and going beyond, lithium-ion batteries, Energy & Environmental Science 5(7) (2012) 7854-7863.

[6] M. Li, J. Lu, Z. Chen, K. Amine, 30 Years of Lithium-Ion Batteries, Advanced Materials 30(33) (2018) 1800561.

[7] B. Scrosati, J. Hassoun, Y.-K. Sun, Lithium-ion batteries. A look into the future, Energy & Environmental Science 4(9) (2011) 3287-3295.

[8] J.W. Choi, D. Aurbach, Promise and reality of post-lithium-ion batteries with high energy densities, Nature Reviews Materials 1(4) (2016) 16013.

[9] W. Xu, J. Wang, F. Ding, X. Chen, E. Nasybulin, Y. Zhang, J.-G. Zhang,

Lithium metal anodes for rechargeable batteries, Energy & Environmental Science 7(2) (2014) 513-537.

[10] J. Liu, Z. Bao, Y. Cui, E.J. Dufek, J.B. Goodenough, P. Khalifah, Q. Li, B.Y. Liaw, P. Liu, A. Manthiram, Y.S. Meng, V.R. Subramanian, M.F. Toney, V.V. Viswanathan, M.S. Whittingham, J. Xiao, W. Xu, J. Yang, X.-Q. Yang, J.-G. Zhang, Pathways for practical high-energy long-cycling lithium metal batteries, Nature Energy 4(3) (2019) 180-186.

[11] M.D. Tikekar, S. Choudhury, Z. Tu, L.A. Archer, Design principles for electrolytes and interfaces for stable lithium-metal batteries, Nature Energy 1(9) (2016) 16114.

[12] M. Rosso, C. Brissot, A. Teyssot, M. Dollé, L. Sannier, J.-M. Tarascon, R. Bouchet, S. Lascaud, Dendrite short-circuit and fuse effect on Li/polymer/Li cells, Electrochimica Acta 51(25) (2006) 5334-5340.

[13] S. Wang, K. Rafiz, J. Liu, Y. Jin, J.Y.S. Lin, Effects of lithium dendrites on thermal runaway and gassing of LiFePO4 batteries, Sustainable Energy & Fuels 4(5) (2020) 2342-2351.

[14] J. Zhang, Q. Rao, B. Jin, J. Lu, Q.-g. He, Y. Hou, Z. Li, X. Zhan, F. Chen, Q. Zhang, Cerium oxide embedded bilayer separator enabling fast polysulfide conversion for high-performance lithium-sulfur batteries, Chemical Engineering Journal 388 (2020) 124120.

[15] Z. Shi, Q. Liu, Z. Yang, L.A. Robertson, S.R. Bheemireddy, Y. Zhao, Z. Zhang, L. Zhang, A chemical switch enabled autonomous two-stage

crosslinking polymeric binder for high performance silicon anodes, Journal of Materials Chemistry A 10(3) (2022) 1380-1389.

[16] A. Gupta, R. Badam, N. Matsumi, Heavy-Duty Performance from Silicon Anodes Using Poly(BIAN)/Poly(acrylic acid)-Based Self-Healing Composite Binder in Lithium-Ion Secondary Batteries, ACS Applied Energy Materials 5(7) (2022) 7977-7987.

[17] H. Liu, Q. Wu, X. Guan, M. Liu, F. Wang, R. Li, J. Xu, Ionically Conductive Self-Healing Polymer Binders with Poly(ether-thioureas) Segments for High-Performance Silicon Anodes in Lithium-Ion Batteries, ACS Applied Energy Materials 5(4) (2022) 4934-4944.

[18] S. Ko, M.-J. Baek, T.-U. Wi, J. Kim, C. Park, D. Lim, S.J. Yeom, K. Bayramova, H.Y. Lim, S.K. Kwak, S.W. Lee, S. Jin, D.W. Lee, H.-W. Lee, Understanding the Role of a Water-Soluble Catechol-Functionalized Binder for Silicon Anodes by Diverse In Situ Analyses, ACS Materials Letters 4(5) (2022) 831-839.

[19] P. Luo, P. Lai, Y. Huang, Y. Yuan, J. Wen, C. Xie, J. Li, L. Liu, A Highly Stretchable and Self-Healing Composite Binder Based on the Hydrogen-Bond Network for Silicon Anodes in High-Energy-Density Lithium-Ion Batteries, ChemElectroChem 9(12) (2022) e202200155.

[20] Z. Song, T. Zhang, L. Wang, Y. Zhao, Z. Li, M. Zhang, K. Wang, S. Xue, J. Fang, Y. Ji, F. Pan, L. Yang, Bio-Inspired Binder Design for a Robust Conductive Network in Silicon-Based Anodes, Small Methods 6(5) (2022)

2101591.

[21] X. Li, Y. Xing, J. Xu, Q. Deng, L.-H. Shao, Uniform yolk–shell structured Si–C nanoparticles as a high performance anode material for the Li-ion battery, Chemical Communications 56(3) (2020) 364-367.

[22] N. Liu, J. Liu, D. Jia, Y. Huang, J. Luo, X. Mamat, Y. Yu, Y. Dong, G. Hu, Multi-core yolk-shell like mesoporous double carbon-coated silicon nanoparticles as anode materials for lithium-ion batteries, Energy Storage Materials 18 (2019) 165-173.

[23] D. Kim, T. Ahmed, K. Crossley, J.K. Baldwin, S.H. Ra Shin, Y. Kim, C. Sheehan, N. Li, D.V. Pete, H.H. Han, J. Yoo, A controlled nucleation and growth of Si nanowires by using a TiN diffusion barrier layer for lithium-ion batteries, Nanoscale Advances 4(8) (2022) 1962-1969.

[24] C. Hwang, K. Lee, H.-D. Um, Y. Lee, K. Seo, H.-K. Song, Conductive and Porous Silicon Nanowire Anodes for Lithium Ion Batteries, Journal of The Electrochemical Society 164(7) (2017) A1564-A1568.

[25] S. Chae, Y. Xu, R. Yi, H.-S. Lim, D. Velickovic, X. Li, Q. Li, C. Wang, J.-G. Zhang, A Micrometer-Sized Silicon/Carbon Composite Anode Synthesized by Impregnation of Petroleum Pitch in Nanoporous Silicon, Advanced Materials 33(40) (2021) 2103095.

[26] Y. An, Y. Tian, C. Liu, S. Xiong, J. Feng, Y. Qian, One-Step, Vacuum-Assisted Construction of Micrometer-Sized Nanoporous Silicon Confined by Uniform Two-Dimensional N-Doped Carbon toward Advanced Li Ion and

MXene-Based Li Metal Batteries, ACS Nano 16(3) (2022) 4560-4577.

[27] C. Li, T. Shi, H. Yoshitake, H. Wang, Improved performance in micron-sized silicon anodes by in situ polymerization of acrylic acid-based slurry, Journal of Materials Chemistry A 4(43) (2016) 16982-16991.

[28] G.-B. Han, J.-N. Lee, D.J. Lee, H. Lee, J. Song, H. Lee, M.-H. Ryou, J.-K. Park, Y.M. Lee, Enhanced cycling performance of lithium metal secondary batteries with succinic anhydride as an electrolyte additive, Electrochimica Acta 115 (2014) 525-530.

[29] G.A. Umeda, E. Menke, M. Richard, K.L. Stamm, F. Wudl, B. Dunn, Protection of lithium metal surfaces using tetraethoxysilane, Journal of Materials Chemistry 21(5) (2011) 1593-1599.

[30] J.H. Baik, S. Kim, D.G. Hong, J.C. Lee, Gel Polymer Electrolytes Based on Polymerizable Lithium Salt and Poly(ethylene glycol) for Lithium Battery Applications, ACS Appl Mater Interfaces 11(33) (2019) 29718-29724.

[31] D. Jeong, J. Shim, H. Shin, J.C. Lee, Sustainable Lignin-Derived Cross-Linked Graft Polymers as Electrolyte and Binder Materials for Lithium Metal Batteries, ChemSusChem 13(10) (2020) 2642-2649.

[32] J. Shim, H.J. Kim, B.G. Kim, Y.S. Kim, D.-G. Kim, J.-C. Lee, 2D boron nitride nanoflakes as a multifunctional additive in gel polymer electrolytes for safe, long cycle life and high rate lithium metal batteries, Energy & Environmental Science 10(9) (2017) 1911-1916.

[33] L. Long, S. Wang, M. Xiao, Y. Meng, Polymer electrolytes for lithium

polymer batteries, Journal of Materials Chemistry A 4(26) (2016) 10038-10069.

[34] Y. An, X. Han, Y. Liu, A. Azhar, J. Na, A.K. Nanjundan, S. Wang, J. Yu, Y. Yamauchi, Progress in Solid Polymer Electrolytes for Lithium-Ion Batteries and Beyond, Small 18(3) (2022) 2103617.

[35] J.-H. Baik, D.-G. Kim, J.H. Lee, S. Kim, D.G. Hong, J.-C. Lee, Nonflammable and thermally stable gel polymer electrolytes based on crosslinked perfluoropolyether (PFPE) network for lithium battery applications, Journal of Industrial and Engineering Chemistry 64 (2018) 453-460.

[36] J.-H. Baik, D.-G. Kim, J. Shim, J.H. Lee, Y.-S. Choi, J.-C. Lee, Solid polymer electrolytes containing poly(ethylene glycol) and renewable cardanol moieties for all-solid-state rechargeable lithium batteries, Polymer 99 (2016) 704-712.

[37] J. Shim, J.W. Lee, K.Y. Bae, H.J. Kim, W.Y. Yoon, J.C. Lee, Dendrite Suppression by Synergistic Combination of Solid Polymer Electrolyte Crosslinked with Natural Terpenes and Lithium-Powder Anode for Lithium-Metal Batteries, ChemSusChem 10(10) (2017) 2274-2283.

[38] C. Sun, J. Liu, Y. Gong, D.P. Wilkinson, J. Zhang, Recent advances in all-solid-state rechargeable lithium batteries, Nano Energy 33 (2017) 363-386.

[39] X. Zhan, J. Zhang, M. Liu, J. Lu, Q. Zhang, F. Chen, Advanced Polymer Electrolyte with Enhanced Electrochemical Performance for Lithium-Ion

Batteries: Effect of Nitrile-Functionalized Ionic Liquid, ACS Applied Energy Materials 2(3) (2019) 1685-1694.

[40] Z. Wei, Y. Ren, M. Wang, J. He, W. Huo, H. Tang, Improving the Conductivity of Solid Polymer Electrolyte by Grain Reforming, Nanoscale Research Letters 15(1) (2020) 122.

[41] C.S. Kim, S.M. Oh, Importance of donor number in determining solvating ability of polymers and transport properties in gel-type polymer electrolytes, Electrochimica acta 45(13) (2000) 2101-2109.

[42] Y. Lu, M. Tikekar, R. Mohanty, K. Hendrickson, L. Ma, L.A. Archer, Stable Cycling of Lithium Metal Batteries Using High Transference Number Electrolytes, Advanced Energy Materials 5(9) (2015) 1402073.

[43] S. Li, A.I. Mohamed, V. Pande, H. Wang, J. Cuthbert, X. Pan, H. He, Z. Wang, V. Viswanathan, J.F. Whitacre, K. Matyjaszewski, Single-Ion Homopolymer Electrolytes with High Transference Number Prepared by Click Chemistry and Photoinduced Metal-Free Atom-Transfer Radical Polymerization, ACS Energy Letters 3(1) (2018) 20-27.

[44] H. Wang, B. Wu, X. Wu, Q. Zhuang, T. Liu, Y. Pan, G. Shi, H. Yi, P. Xu, Z. Xiong, S.-L. Chou, B. Wang, Key Factors for Binders to Enhance the Electrochemical Performance of Silicon Anodes through Molecular Design, Small 18(1) (2022) 2101680.

[45] A. Magasinski, B. Zdyrko, I. Kovalenko, B. Hertzberg, R. Burtovyy, C.F. Huebner, T.F. Fuller, I. Luzinov, G. Yushin, Toward Efficient Binders for Li-

Ion Battery Si-Based Anodes: Polyacrylic Acid, ACS Applied Materials & Interfaces 2(11) (2010) 3004-3010.

[46] Z. Zheng, H. Gao, C. Ke, M. Li, Y. Cheng, D.-L. Peng, Q. Zhang, M.-S. Wang, Constructing Robust Cross-Linked Binder Networks for Silicon Anodes with Improved Lithium Storage Performance, ACS Applied Materials & Interfaces 13(45) (2021) 53818-53828.

[47] Y.K. Jeong, T.-w. Kwon, I. Lee, T.-S. Kim, A. Coskun, J.W. Choi, Millipede-inspired structural design principle for high performance polysaccharide binders in silicon anodes, Energy & Environmental Science 8(4) (2015) 1224-1230.

[48] I. Kovalenko, B. Zdyrko, A. Magasinski, B. Hertzberg, Z. Milicev, R. Burtovyy, I. Luzinov, G. Yushin, A Major Constituent of Brown Algae for Use in High-Capacity Li-Ion Batteries, Science 334(6052) (2011) 75-79.

[49] Z. Li, G. Wu, Y. Yang, Z. Wan, X. Zeng, L. Yan, S. Wu, M. Ling, C. Liang, K.N. Hui, Z. Lin, An Ion-Conductive Grafted Polymeric Binder with Practical Loading for Silicon Anode with High Interfacial Stability in Lithium-Ion Batteries, Advanced Energy Materials 12(29) (2022) 2201197.

[50] J.-T. Li, Z.-Y. Wu, Y.-Q. Lu, Y. Zhou, Q.-S. Huang, L. Huang, S.-G. Sun, Water Soluble Binder, an Electrochemical Performance Booster for Electrode Materials with High Energy Density, Advanced Energy Materials 7(24) (2017) 1701185.

[51] N. Lingappan, L. Kong, M. Pecht, The significance of aqueous binders

in lithium-ion batteries, Renewable and Sustainable Energy Reviews 147 (2021) 111227.

[52] A. Cholewinski, P. Si, M. Uceda, M. Pope, B. Zhao, Polymer Binders: Characterization and Development toward Aqueous Electrode Fabrication for Sustainability, Polymers 13(4) (2021) 631.

[53] X. Zhu, F. Zhang, L. Zhang, L. Zhang, Y. Song, T. Jiang, S. Sayed, C. Lu, X. Wang, J. Sun, Z. Liu, A Highly Stretchable Cross-Linked Polyacrylamide Hydrogel as an Effective Binder for Silicon and Sulfur Electrodes toward Durable Lithium-Ion Storage, Advanced Functional Materials 28(11) (2018) 1705015.

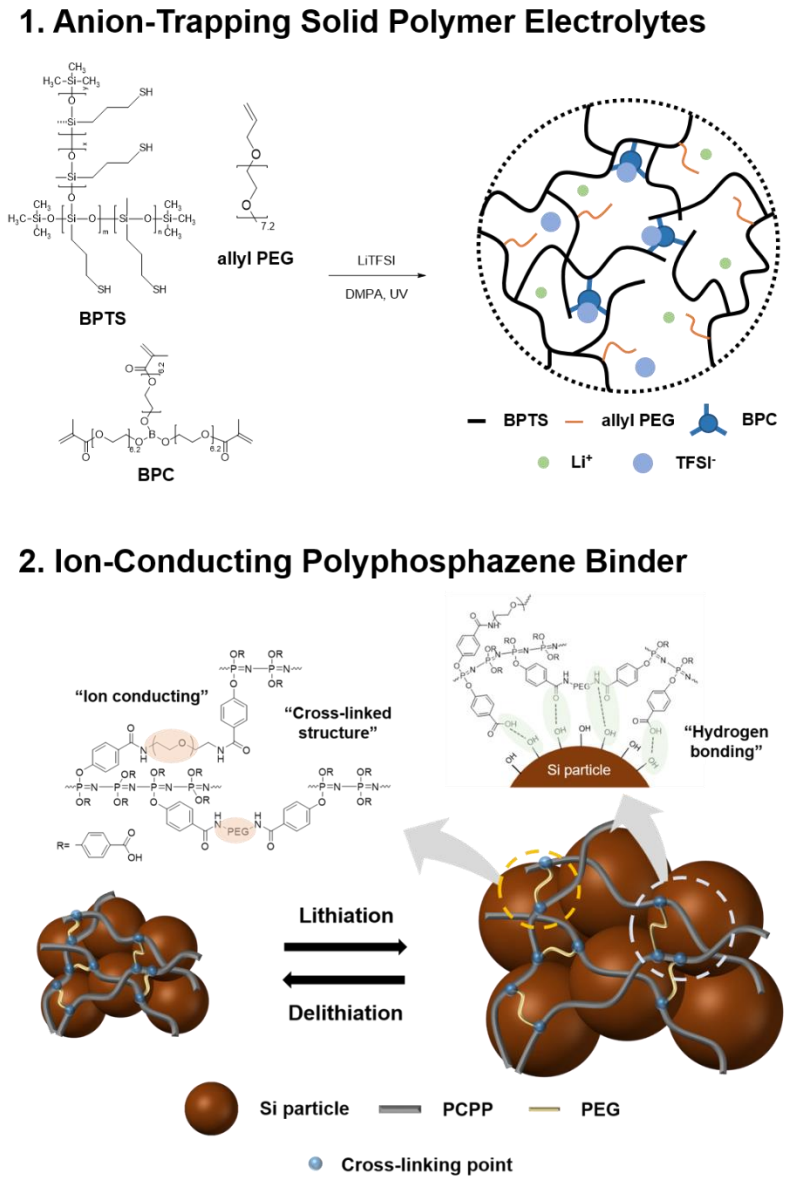

Figure 1.1. Anion-trapping cross-linked solid polymer electrolytes for lithium metal battery and ion-conducting cross-linked polyphosphazene binder for Si anode.

Chapter 2

Solid Polymer Electrolytes Based on Polysiloxane with Anion-Trapping Boron Moieties for All-Solid-State Lithium Metal Batteries

2.1 Introduction

Along with ever-increasing demand for electric vehicles, portable devices, and energy storage system, the development of battery systems with high energy density, safety, and longer life span has received great attention [1-4]. Lithium metal batteries (LMBs) has been investigated extensively for several decades due to the advantages of lithium metal such as extremely high theoretical capacity (3860 mAh g^{-1}), low density (0.58 g cm^{-3}), and lowest negative electrochemical potential (–3.040 V *vs.* hydrogen standard electrode) [2, 5, 6]. However, the practical application of LMBs is hampered by several disadvantages of the lithium metal as an anode material [7] such as unstable solid electrolyte interface (SEI) layer [8, 9] and lithium dendrite formation [7, 10]. The unstable SEI layer leads to the continuous electrolyte consumption and low Coulombic efficiency, resulting in poor long-term stability of LMBs [11]. The lithium dendrite formation, which is regarded as the main cause of the battery failure, results in the lithium metal penetration through separator, internal short-circuit of the battery, and finally thermal runaway [10].

During last several decades, various strategies such as adding electrolyte additives [12-18], forming artificial SEI layer [19-22], and using gel or solid electrolytes [23-30] have been suggested to suppress the formation and growth of lithium dendrites. In particular, solid polymer electrolytes (SPEs), which are composed of polymer matrix and lithium salts in the absence of any

liquid components, have advantages such as low flammability, flexibility, and dimensional stability [31]. SPEs based on poly(ethylene oxide) (PEO) have been extensively studied owing to Li^+ solvating ability and ion-conducting nature of ethylene oxide units [32]. However, since PEO-based electrolytes suffer from the low ionic conductivity by crystalline structure of PEO, studies to improve ionic conductivity by suppressing the crystallization of PEO have been reported [33-36]. Although polymer electrolytes based on poly(ethylene glycol) (PEG), low molecular weight PEO, have been developed because PEG have lower crystallinity, they could not be used as SPEs due to the insufficient dimensional stability of PEG [37]. Therefore, various studies have reported PEG-based SPEs with high ionic conductivity and dimensional stability through tailoring polymer morphology [38-40], cross-linking polymer chains [24, 30], and adding inorganic fillers [28, 29, 41].

Although cross-linking the PEG-based polymer can increase the dimensional stability, it can decrease the mobility of the polymer chain [42]. Since polysiloxane has a low barrier energy against polymer backbone bond rotation ($\approx$0.8 kJ mol^{-1}), it can promote ion transport in the SPEs by the high chain mobility [26, 43, 44]. Thus, the combination of PEG and polysiloxane with cross-linked polymer structure has been suggested to minimize the decrease of the conductivity of PEG-based cross-linked SPEs [45, 46].

In conventional PEG-based SPEs, both lithium cations and counter anions migrate between cathodes and anodes during the battery cycling [47]. In

particular, the lithium ions move more slowly than the anions, because the lithium ions in the PEG matrix coordinate with the oxygen atoms in ethylene oxide units [48]. Lithium ion transference number (t_{Li^+}) defined as the fraction of the current carried by lithium ions is widely used to comprehend this phenomena [49]. It is highly desirable to use an electrolyte having large t_{Li^+} value, because it not only reduces the concentration polarization, thereby lowering internal resistance of battery and improving cell performance [50], but also inhibits the formation and growth of lithium dendrites [51, 52]. Various strategies for increasing the t_{Li^+} value of polymer electrolytes such as introducing Lewis acidic groups [53, 54], adding organic or inorganic fillers [55-60], and attaching anions to the polymer matrix [23, 61] have been suggested. Especially, the incorporation of 'anion-trapping' sp^2 boron moieties in polymer electrolytes has been known to increase the t_{Li^+} value by Lewis acid-base interaction between empty p orbital of boron and anions of lithium salts [41, 62-66].

In this study, the lithium ion conducting PEG-based SPE system with flexible hyperbranched polysiloxane structure and the anion-trapping boron containing cross-linker is prepared for high temperature all-solid-state LMB applications. Overall characteristics of the prepared SPEs with different cross-linking density and anion-trapping boron content including ionic conductivity and electrochemical properties are investigated.

2.2 Experimental

Materials

(3-Mercaptopropyl)trimethoxysilane and (3-mercaptopropyl)methyldimethoxysilane were purchased from TCI Chemicals and used as received. Methoxytrimethylsilane, trimethyl borate, poly(ethylene glycol) methacrylate (PEGMA, average M_n = 360 g mol^{-1}), poly(ethylene glycol) methyl ether (mPEG, average M_n = 350 g mol^{-1}), trimethylolpropane ethoxylate triacrylate (TMPETA, average M_n = 912 g mol^{-1}), allyl bromide, bis(trifluoromethane)sulfonimide lithium salt (LiTFSI), and 2,2-dimethoxy-2-phenylacetophenone (DMPA) were purchased from Aldrich and used as received. Acetonitrile (TCI) and toluene (Junsei) were dried over 4 Å molecular sieve prior to use. Tetrahydrofuran (THF) was distilled over sodium/benzophenone under a nitrogen atmosphere. Allyl PEG was synthesized as described in our previous study as follows [26]. mPEG and allyl bromide were reacted in the presence of sodium hydroxide with dried toluene at 45 °C. The residual solvent was removed by under reduced pressure and purified by extraction and allyl PEG was obtained by 90 % yield. All other reagents and solvents were obtained from reliable commercial sources and used as received.

Synthesis of branched polysiloxane with thiol side and trimethylsilyl end groups (BPTS)

Branched polysiloxane with thiol side group was synthesized by acid-catalyzed hydrolysis and condensation reaction following the previous procedure reported before [26]. 7.4 g of hydrochloric acid (36.5% aqueous solution, 71 mmol) was added into the mixture of solvents (12.8 g of ethanol and 2.9 g of distilled water) and then the mixture of monomers (2.7 g of (3-mercaptopropyl)trimethoxysilane (14 mmol) and 2.5 g of (3-mercaptopropyl)methyldimethoxysilane (14 mmol)) was added into the mixture of solvents. Then the solution was heated at 50 °C for 15 h under nitrogen atmosphere. After the polymerization, methoxytrimethylsilane (1 g, 9.6mmol) was added to the solution at 0 °C and stirred for another 30 min at 50 °C to obtain branched polysiloxane with thiol side and trimethylsilyl end groups (BPTS) (Figure 2.1.(a)). The reaction mixture was poured to distilled water several times for purification. After being dried under vacuum at room temperature for 24h, transparent and viscous oil was obtained by 60% yield. ^{1}H NMR [400 MHz, $CDCl_3$, δ (ppm), TMS ref] of BPTS: 2.55 (q, 2H, –CH_2SH), 1.68 (q, 2H, –CH_2–), 1.36 (t, 1H, –SH), 0.68 (t, 2H, –SiCH_2–), 0.13 (s, 3H, –$SiCH_3$). The number-average molecular weight (M_n) was measured to 3,000 g mol^{-1} by GPC analysis (Figure 2.2).

Synthesis of boron-containing poly(ethylene glycol) cross-linker (BPC)

Boron-containing poly(ethylene glycol) cross-linker (BPC) was synthesized as described in our previous study [62]. Trimethyl borate (0.3 g, 2.9 mmol), poly(ethylene glycol) methacrylate (PEGMA, 3.1 g, 8.7 mmol), and acetonitrile (31 mL) were placed in the 100 mL one-neck round-bottomed flask equipped with a magnetic stirring bar and heated at 50 °C for 3 h under nitrogen atmosphere (Figure 2.2.(b)). Then, the reaction temperature was raised to 70 °C and stirred for another 2 h while purging with nitrogen to eliminate methanol which is a byproduct. After being dried under vacuum at room temperature for 24 h, transparent and viscous oil was obtained by 85% yield. The degree of substitution could be calculated by the following eq (1);

$$\text{Degree of substitution (\%)} = (I_{B-O-CH_2}/2)/(I_{CH_2=C}/2) \times 100 \quad (1)$$

where I_{B-O-CH_2} and $I_{CH_2=C}$ are the intensities of the each peak in ^{1}H NMR spectrum. The degree of substitution was found to be 78%. ^{1}H NMR [400 MHz, $CDCl_3$, δ (ppm), TMS ref] of BPC: 6.13 (s, 1H, vinyl), 5.58 (s, 1H, vinyl), 4.35–4.20 (m, C(O)–O–CH_2), 4.05–3.88 (m, 2H, B–O–CH_2), 3.57–3.77 (m, CH_2–CH_2–O), 1.95 (s, 3H, CH_3).

Preparation of cross-linked solid polymer electrolytes

Cross-linked solid polymer electrolytes with boron cross-linker (CSPE-B#) were prepared by mixing BPTS, BPC, allyl PEG, and LiTFSI in different molar ratios shown in Table 2.1 followed by UV irradiation, where # is the mole percent of double bonds of BPC among the total double bonds in BPC and allyl PEG. For the preparation of CSPE-B60, BPTS (0.04 g, 0.325 mmol of thiol group), BPC (0.075 g, 0.075 mmol), allyl PEG (0.054 g, 0.130 mmol), LiTFSI (0.046 g, 0.150 mmol, [Li]/[EO unit] = 0.07), and DMPA (0.004 g, 0.015 mmol) were dissolved in distilled THF (0.35 mL). Therefore, the molar ratio of BPTS, BPC, and allyl PEG is as shown in Table 2.1. 0.04 g of BPTS contains 0.325 mmol of thiol because the average molecular weight of the repeating units containing thiol in BPTS is 116.03 g mol^{-1}. The details for the calculation of the average molecular weight are shown in the Figure 2.3. The solution was cast onto a glass plate (2.5 x 2.5 cm^2) and the solvent was dried under vacuum at room temperature followed by vacuum drying at 60 °C for 1 day. Subsequently, the glass plate was irradiated by a UV lamp (UVP B-100AP/R, 100 Watt, 365 nm, Analytik Jena, USA) for 2 h. The resulting film was peeled off from the glass plate and dried under vacuum at 60 °C for 2 days prior to further characterization. Other polymer electrolytes such as PE-B0, CSPE-B20, CSPE-B40, CSPE-B50, CSPE-B80, and CSPE-B100 were prepared with the same procedure except the ratio of BPC and allyl PEG.

Boron-free cross-linked SPEs (CSPE-BFs) were also prepared from the same procedures used for preparation of CSPE-Bs except using TMPETA as the cross-linker (Table 2.1). The average thickness of the SPEs were in the range of 250–300 μm.

Cell fabrication and electrochemical analysis

Ionic conductivities of the prepared SPEs were measured by electrochemical impedance spectroscopy (EIS) in a temperature range of 10 to 130 °C using Zahner Zennium XC apparatus in the frequency range of 0.1 Hz to 1 MHz at an applied AC voltage of 10 mV. Two electrode cells were assembled by sandwiching SPE between two symmetric circular stainless electrodes. Each cell was allowed to equilibrate for 30 min at each temperature prior to measurement. The real part of the impedance at the minimum of the imaginary part was regarded as a resistance (R) to calculate the conductivity of the SPEs. The ionic conductivity (σ) was calculated using the following equation, $\sigma = (1/R) \times (d/A)$, where d is the thickness of SPE, and A is the area of electrode. Lithium ion transference number (t_{Li^+}) was measured by Bruce-Vincent method using EIS and direct current (DC) polarization. Li/SPE/Li symmetric cell was fabricated and polarized by a constant DC voltage of 10 mV. The current was recorded until the current reached a steady

state. The initial and steady-state impedances of the cell were also measured by EIS. The t_{Li^+} was calculated using following eq (2);

$$t_{Li^+} = \frac{i_{ss}(V - i_0 R_0)}{i_0(V - i_{ss} R_{ss})} \quad (2)$$

where V is the constant DC voltage applied to the cell; i_0 and i_{ss} are the initial and steady-state currents; and R_0 and R_{ss} are the initial and steady-state interfacial resistances, respectively. The electrochemical stability of the electrolyte was investigated by linear sweep voltammetry (LSV). The cell for LSV measurement was fabricated by sandwiching electrolyte between a stainless steel electrode (working electrode) and a lithium metal electrode (reference electrode) in a 2032 coin cell. The cell was swept in the potential range from 2.95 V to 7 V (*vs.* Li/Li^+) at a scan rate of 1 mV s^{-1} at 60 °C. A galvanostatic charge-discharge test of all-solid-state lithium metal battery was performed with WBCS3000 battery cycler (WonATech) in a voltage range of 2.0–4.0 V (*vs.* Li/Li^+) at 60 °C. V_2O_5 was used as a cathode active material. A slurry composed of V_2O_5 (70 wt%), Super P (20 wt%), and PVDF binder (10 wt%) was dispersed in anhydrous N-methyl-2-pyrrolidone (NMP) and coated uniformly on an aluminum current collector using a doctor blade. The residual solvent was dried under 120 °C for 24 h. The V_2O_5 mass loading was 2.0 mg cm^{-2}. The cathode coated with corresponding SPE, lithium metal foil, and SPE were assembled together in a 2032 coin cell. All components were assembled in an argon-filled glove box (H_2O<0.5 ppm, O_2<0.5 ppm).

Characterization

^{1}H nuclear magnetic resonance (NMR) spectra were obtained using Ascend™ 400 spectrometer (300 MHz) with $CDCl_3$ (Cambridge Isotope Laboratories) as a solvent with tetramethylsilane (TMS) as a reference. Molecular weights (M_n, M_w) and polydispersity index (PDI) were measured by gel permeation chromatography (GPC) apparatus equipped with Waters 515 HPLC pump and three columns including PLgel 5.0 μm guard, MIXED-C, and MIXED-D from Polymer Laboratories followed by a refractive index (RI) detector (Viscotek LR125 laser refractometer). The obtained data were calibrated using polystyrene standards and analyzed using the Omnisec software. HPLC grade THF (J. T. Baker) was used as an eluent at a flow rate of 1.0 mL min^{-1} at 35 °C. Thermal transition behaviors were analyzed by differential scanning calorimetry (DSC) using a TA Instruments DSC 25 under a nitrogen atmosphere. Samples with a typical mass of 5–10 mg were encapsulated in sealed aluminum pans. The samples were first heated to 120 °C and then quenched to –80 °C to initialize crystallization, followed by a second heating scan from –80 °C to 100 °C at a heating rate of 10 °C min^{-1}. Thermal stability was investigated by thermogravimetric analysis (TGA) using TA instruments TGA 55 under a nitrogen atmosphere. The samples were placed at 120 °C for 10 min to remove any residual solvent, and then heated

to 700 °C at a heating rate of 10 °C min^{-1}. Fourier transform infrared (FT-IR) spectroscopy was performed on a Nicolet 6700 in the wavenumber range from 4000 to 600 cm^{-1} with a resolution of 4 cm^{-1}. Field-emission scanning electron microscopy (FE-SEM) and energy-dispersive X-ray spectroscopy (EDS) were performed on a Carl Zeiss SUPRA 55VP with an accelerating voltage of 10 kV. Storage modulus was measured by advanced rheometric expansion system (ARES) using Rheometric Scientific ARES with 1 rad s^{-1} of frequency and 5 % strain from 30 °C to 180 °C at 3 °C min^{-1} ramp. X-ray photoelectron spectroscopy (XPS) measurements were performed on an AXIS-SUPRA XPS (Kratos Analytical, UK) using Mg Ka (1254.0 eV) as the radiation source. The lithium electrode samples were sealed in an Ar-filled chamber during the entire transfer process.

2.3 Results and Discussion

Preparation of cross-linked solid polymer electrolytes with boron cross-linker (CSPE-Bs)

Branched polysiloxane with thiol side and trimethylsilyl end groups (BPTS) was synthesized by acid-catalyzed hydrolysis and condensation reaction of thiol containing methyldimethoxysilane and trimethoxysilane, followed by end-capping reaction as shown in Figure 2.1.(a). The combination of methyldimethoxysilane and trimethoxysilane results in the polysiloxane with the hyperbranched structure. Methoxytrimethylsilane was added into the reaction mixture after the reaction to end-cap the hydroxyl groups at the chain ends to prevent the possible side reactions with lithium metal in the battery system [67]. The polysiloxane with hyperbranched structure is effective in improving the ionic conductivity of cross-linked SPE, because the polysiloxane backbone is very flexible due to its low barrier energy for the polymer backbone rotation [43] and the hyperbranched structure increases free volume of the polymer chain that can further increase the ionic conductivity of the polymer electrolytes [68]. In the ^{1}H NMR spectrum of BPTS (Figure 2.4), the signal from 1.36 ppm is assigned to the protons in the thiol group and the signal from 0.13 ppm is assigned to methyl group bonded to silicon, while those at 2.55, 1.68, and 0.68 ppm are originated from propyl

side groups.

Boron-containing poly(ethylene glycol) cross-linker (BPC) was synthesized from trimethylborate and poly(ethylene glycol) methacrylate (PEGMA) as shown in Figure 2.1.(b). The ^{1}H NMR spectrum of BPC correctly represents the chemical structure of BPC (Figure 2.5) [62]. The proton peaks adjacent to hydroxyl group in PEGMA shift to the down field after the formation of BPC due to the electron-deficient nature of boron atom. Thus, the signal from 3.88–4.05 ppm could be assigned to the protons of ethylene oxide unit adjacent to boron atom (B–O–CH_2–). CSPE-Bs were prepared by UV irradiation of the mixtures of BPTS, BPC, allyl PEG, and LiTFSI (Figure 2.6). DMPA was added to initiate thiol-ene click reaction of thiol of BPTS and double bonds in BPC and allyl PEG and LiTFSI with a [Li^+]/[EO unit] ratio of 0.07 was also included. Cross-linking density of CSPE-B# could be controlled by adjusting the molar ratio of BPC and allyl PEG (Table 2.1). The thiol-ene reaction was monitored by FT-IR spectroscopy to confirm thiol-ene reaction as shown in Figure 2.7.(a) and Figure 2.8. The complete consumption of thiol and double bonds could be confirmed by the disappearance of thiol peak at 2560 cm^{-1} and C=C stretching peak at around 1640 cm^{-1} after 2 h of UV irradiation. CSPE-B50, CSPE-B60, CSPE-B80, and CSPE-B100 were obtained as flexible free-standing films with an average thickness of 250–300 μm (Figure 2.7.(b)). CSPE-B20 and CSPE-B40 were not dimensionally stable because fully cross-linked structure was not obtained because only small

amount of cross-linker was used and PE-B0 was obtained in a wax state because no cross-linker was used. Nonporous and smooth surface of the prepared SPEs was observed in SEM images. For example, CSPE-B60 shows dense and smooth surface indicating that the components are homogeneously mixed without any phase-separation (Figure 2.9.(a)). It was also confirmed that each element is uniformly distributed through EDS analysis (Figure 2.9.(b)–(d)). CSPE-BFs without the boron moiety was also prepared using the same procedure used for CSPE-Bs to explain the effect of BPC on the properties of SPE system (Figure 2.10).

Characterization of the SPEs

Thermal transition behavior of CSPE-Bs and PE-B0 was investigated by DSC (Figure 2.11.(a)). The T_g values of PE-B0 to CSPE-B100 increase from –61.9 °C to –38.4 °C. The T_g of CSPE-Bs are much lower than room temperature although they are cross-linked because of the high flexibility of polysiloxane backbone. We further studied the relationship between the lithium salt concentration and the T_g value in CSPE-B60 (Figure 2.11.(b)), because CSPE-B60 is the representative sample having relatively high ionic conductivity with large lithium transference number showing the best cell performance when it was used as the SPE as discussed in the later part of this paper. The T_g values increase with the increase of salt concentration indicating

that the lithium ions strongly coordinate with EO groups in CSPE-B60 decreasing the chain mobility. For CSPE-BFs, T_g values also increase with the increase of the content of cross-linker, TMPETA (Table 2.1).

The ionic conductivity of CSPE-B60 with different LiTFSI doping concentration was measured (Figure 2.11.(c)). The ionic conductivity of CSPE-B60 was obtained at a $[Li^+]$/[EO unit] ratio of 0.07 and the values were 2.1×10^{-5} S cm^{-1} and 1.3×10^{-4} S cm^{-1} at 30 °C and 60 °C, respectively. The ionic conductivity is proportional to the product of the number of charge carriers and the mobility of the charge carriers [24]. At the low salt concentration region ($[Li^+]$/[EO unit] ≤ 0.07), the ionic conductivity increases as the number of charge carriers increases, while the ionic conductivity decreases due to the decrease of charge carrier mobility after the maximum point ($[Li^+]$/[EO unit] = 0.07) [24]. Figure 2.11.(d) shows the ionic conductivities of CSPE-B50, CSPE-B60, CSPE-B80, and CSPE-B100 at various temperatures having the same lithium salt concentration of $[Li^+]$/[EO unit] = 0.07. The ionic conductivity values of PE-B0, CSPE-B20, and CSPE-B40 could not be measured in this study because we could not make the free-standing films that can work as the SPE between the electrodes. Since we did not use any separator to make our all-solid-state batteries, PE-B0 having the wax state and dimensionally unstable CSPE-B20 and CSPE-B40 could not be used to make the cell to compare the ionic conductivity and cell performance. While CSPE-B50, CSPE-B60, CSPE-B80, and CSPE-B100 could be used to

make the cell and their ionic conductivity values decreased as the cross-linking density increased (Table 2.1). It is well known that the increase of the cross-linking density in the SPE decreases the ionic conductivity [69, 70]. For the same reason, the ionic conductivity of CSPE-BFs decreases with the increase of the content of cross-linker, TMPETA, without any boron moiety.

The thermal and electrochemical stability of polymer electrolytes were investigated (Table 2.1). The decomposition temperature for 1 wt% loss was measured by TGA analysis. The TGA curves of CSPE-Bs with PE-B0 and CSPE-BFs are shown in Figure 2.12.(a) and (b), respectively. The thermal stability of the prepared electrolytes increases as the content of the cross-linker increases. The decomposition temperatures for 1 wt% loss of all the samples are higher than 190 °C and any weight loss was not observed until 150 °C, suggesting that our SPEs are thermally stable at elevated temperature such as 60 °C due to the cross-linked structure. The decomposition voltage behavior of the samples was studied by linear sweep voltammetry (LSV) at 60 °C with a scan rate of 1 mV s^{-1} using the cell fabricated by the CSPEs. The LSV curves of CSPE-Bs and CSPE-BFs are shown in Figure 2.13.(a) and (b), respectively. The abrupt increase of anodic current corresponding to electrochemical decomposition is observed at 4.85–5.24 V (vs. Li/Li^+). Although there is some deviation, the increase of the cross-linker increases the decomposition voltage because the cross-linked structure can hinder the decomposition of segments [71]. Still, it is clear that CSPEs are

electrochemically stable in the operating voltage of V_2O_5 cathode as well as high-voltage cathode materials.

The lithium ion transference number (t_{Li^+}) of polymer electrolytes was measured by Bruce-Vincent method using DC polarization and AC impedance results of Li/electrolytes/Li symmetric cell (Figure 2.14). Table 2.1 and Figure 2.15 shows the t_{Li^+} values of PE-B0, CSPE-Bs, and CSPE-BFs with various cross-linking density. The t_{Li^+} values of boron-containing CSPE-Bs are larger than those of CSPE-BFs because Lewis acidic boron moieties from BPC can trap TFSI anions. The increase in the BPC content in CSPE-Bs increases the t_{Li^+} values due to increased anion-trapping ability by boron atom in the electrolyte. Slight increase of t_{Li^+} value in CSPE-BFs could be observed with the increase of the cross-linker content, although the trend is not very clear. It was reported that the cross-linking can increase the t_{Li^+} value because the dense cross-linked structure can decrease the mobility of relatively large anions [72]. Therefore it is also possible that the increase of the t_{Li^+} value of CSPE-Bs with the increase of the cross-linker content is affected by the cross-linking density for some degree. Because the higher salt concentration of the electrolyte restricts the movement of large anions, the t_{Li^+} value of PE-B0, which does not contain a cross-linker but has a higher salt concentration, is higher than those of CSPE-BFs. The ionic conductivity and the t_{Li^+} value can be affected by the chain lengths of PEG in the SPEs. For example, as the chain length of the PEG constituting the SPE increases,

the crosslinking density decreases, and as a result, the ionic conductivity increases. For the SPE containing anion-trapping moieties, as the length of the PEG increases, the anion-trapping effect decreases and the t_{Li^+} value decreases. To investigate the effect of PEG chain length on the ionic conductivity and the t_{Li^+} value, the CSPEs with shorter and longer PEG chain length were prepared and their ion conductivity and the t_{Li^+} values were measured (Figure 2.16 and Figure 2.17).

Cell Performance

Galvanostatic charge-discharge tests of all-solid-state V_2O_5/SPE/Li batteries were performed at 60 °C to evaluate the cycle stability and performance for high temperature application (Figure 2.18.(a)). To observe the effect of anion-trapping property on the cell performance, CSPE-B50 and CSPE-B60 having the highest ionic conductivity among CSPE-Bs, and CSPE-BF40 having the ionic conductivity close to that of CSPE-B50 and CSPE-B60, were used as the SPE for the cell test (Figure 2.20). Due to sufficient dimensional stability of the SPEs, the separator was not used for the cell fabrication. To create ion conductive pathway in the cathode and decrease the interfacial resistance between cathode and SPE, the SPE precursor solution was cast on each cathodes and exposed to UV. Since the ionic conductivity of the SPEs at room temperature is not high enough for the cell

test, the test was conducted with a low current density of 0.1 C at 60 °C, like other SPE system [24, 26, 28-30, 41, 68, 73]. It might be possible that the addition of inorganic fillers or organic plasticizer can increase the ionic conductivity of the SPEs as reported before [74-77] and such study is currently conducted in our group. Cells with CSPE-B50 and CSPE-B60 show higher discharge capacity values than the cell with CSPE-BF40 during 50 cycles. Although CSPE-BF40 shows comparable ionic conductivity to CSPE-B50 and CSPE-B60, the cell with CSPE-BF40 exhibits poorer cell performance due to the smaller t_{Li^+} value by the concentration polarization [78]. The cell with CSPE-B60 shows higher discharge capacity values than the cell with CSPE-B50 during 50 cycles. Furthermore, the cell with CSPE-B60 shows remarkable capacity retention (80%) and Coulombic efficiency (>99%) even though the ionic conductivity value of CSPE-B60 is smaller than that of CSPE-B50. This result could be ascribed to: (1) the larger lithium ion transference number of CSPE-B60 by the reduced concentration polarization, (2) the larger storage modulus value of CSPE-B60 (≈ 0.1 MPa) that can effectively suppress lithium dendrite growth (Figure 2.21) [79]. Furthermore, the cell with CSPE-B60 shows higher discharge capacity values than that with PP separator and liquid electrolyte (1M $LiPF_6$ EC/DMC, 1:1 v/v) (Figure 2.22) because the liquid electrolyte system cannot suppress lithium dendrite growth. The charge−discharge profiles at different rates of the cell with CSPE-B60 showed reversible discharge capacity of 289 mAh g^-

[1] at 0.1C, 197 mAh g^{-1} at 0.2C, and 108 mAh g^{-1} at 0.5C (Figure 2.23). Plateaus due to the electrochemical lithiation were observed, and the discharge plateau moves to a lower potential at high current density due to the limited lithium ion diffusion. Surface morphologies of the lithium metal anode after 50 cycles are shown in Figure 2.18.(b). A rough and mossy surface of lithium metal with a lot of dendrites is observed in the cell with CSPE-BF40, whereas the lithium metal anodes of the cell with CSPE-B50 and CSPE-B60 show much smoother surface without any noticeable dendrites, demonstrating that the CSPE-B50 and CSPE-B60 suppressed the dendrite growth more effectively than CSPE-BF40. It could be attributed to the reduced concentration polarization in the cells with CSPE-B50 and CSPE-B60 which have larger t_{Li^+} values than CSPE-BF40 [51, 52, 80-82]. Furthermore, lithium metal with CSPE-B60 shows much smoother surface compared to that with CSPE-B50 because CSPE-B60 has larger lithium transference number and mechanical strength, resulting in better cycling performance than CSPE-B50. X-ray photoelectron spectroscopy (XPS) analysis on the lithium metal surfaces of the V_2O_5/CSPE/Li cells with CSPE-B60 and CSPE-BF40 after cycling for 50 cycles at 60 °C with a rate of 0.1 C was performed. Figure 2.18.(c) and (d) show the XPS spectra of N 1s and F 1s, and Figure 2.24 shows those of C 1s, O 1s, and S 2p. For the N 1s spectra, the cells with CSPE-B60 and CSPE-BF40 show two peaks corresponding to TFSI (399 eV) and Li_3N (397 eV). Li_3N is the product of the decomposition

of TFSI anion [83]. The relative intensity of Li_3N peak in cell with CSPE-BF40 is much stronger than that in the cells with CSPE-B60, indicating that LiTFSI is more decomposed in the cell with CSPE-BF40. Since LiF is also produced by the decomposition of LiTFSI [84], the F 1s spectra of the anodes can also show the decomposition behavior. The peak intensity of LiF peak in the cell with CSPE-BF40 is stronger than that in the cell with CSPE-B60 in the spectra. In the cell with CSPE-B60 containing anion-trapping boron moieties, the anionic TFSI can be trapped resulting in the decrease of concentration polarization of TFSI anions. The reduced local TFSI anion concentration can lower TFSI decomposition on the lithium metal surface. These XPS results are consistent with the result that the lithium transference number of CSPE-B60 is larger than that of CSPE-BF40. Therefore, the anion-trapping effect of the boron moieties in CSPE-B60 can decrease the concentration polarization and lithium dendrite growth.

2.4 Conclusion

In this study, SPEs containing flexible hyperbranced polysiloxane, anion-trapping boron cross-linker, and ion-conductive PEG moieties were prepared for all-solid-state lithium metal battery applications. For the preparation of dimensionally stable cross-linked SPEs, thiol groups in branched polysiloxane (BPTS), double bonds in anion-trapping boron cross-linker (BPC), and double bonds in allyl PEG were reacted *via* thiol-ene click reaction under UV irradiation. The ionic conductivity of 2.2×10^{-4} S cm^{-1} was obtained from CSPE-B50 at 60 °C and slightly lower ionic conductivity of 1.3×10^{-4} S cm^{-1} was obtained from CSPE-B60 at same temperature, where CSPE-B50 and CSPE-B60 have 50 and 60 mole percent of double bonds of BPC, respectively, among the total double bonds in BPC and allyl PEG. CSPE-B50 and CSPE-B60 showed lithium ion transference numbers (t_{Li^+}) of 0.32 and 0.35, respectively, of which are higher than that of CSPE-BF40 (0.15), because they have the anion-trapping boron moieties. Furthermore, CSPE-B60 exhibited excellent thermal stability up to 200 °C and electrochemical stability up to 5.00 V. Since CSPE-B60 have relatively large t_{Li^+} value and physical stability, the cell with CSPE-B60 showed excellent cycle stability during 50 cycles at elevated temperature. We believe that our results provide insight into the incorporation of anion-trapping moieties to the cross-linked SPEs in advanced all-solid-state lithium metal battery applications.

2.5 References

[1] T. Kim, W. Song, D.-Y. Son, L.K. Ono, Y. Qi, Lithium-ion batteries: outlook on present, future, and hybridized technologies, Journal of Materials Chemistry A 7(7) (2019) 2942-2964.

[2] M. Armand, J.M. Tarascon, Building better batteries, Nature 451(7179) (2008) 652-657.

[3] J.M. Tarascon, M. Armand, Issues and challenges facing rechargeable lithium batteries, Nature 414(6861) (2001) 359-367.

[4] J. Qian, B. Jin, Y. Li, X. Zhan, Y. Hou, Q. Zhang, Research progress on gel polymer electrolytes for lithium-sulfur batteries, Journal of Energy Chemistry 56 (2021) 420-437.

[5] W. Xu, J. Wang, F. Ding, X. Chen, E. Nasybulin, Y. Zhang, J.-G. Zhang, Lithium metal anodes for rechargeable batteries, Energy & Environmental Science 7(2) (2014) 513-537.

[6] J. Liu, Z. Bao, Y. Cui, E.J. Dufek, J.B. Goodenough, P. Khalifah, Q. Li, B.Y. Liaw, P. Liu, A. Manthiram, Y.S. Meng, V.R. Subramanian, M.F. Toney, V.V. Viswanathan, M.S. Whittingham, J. Xiao, W. Xu, J. Yang, X.-Q. Yang, J.-G. Zhang, Pathways for practical high-energy long-cycling lithium metal batteries, Nature Energy 4(3) (2019) 180-186.

[7] M.D. Tikekar, S. Choudhury, Z. Tu, L.A. Archer, Design principles for electrolytes and interfaces for stable lithium-metal batteries, Nature Energy

1(9) (2016) 16114.

[8] D. Aurbach, E. Zinigrad, Y. Cohen, H. Teller, A short review of failure mechanisms of lithium metal and lithiated graphite anodes in liquid electrolyte solutions, Solid State Ionics 148(3) (2002) 405-416.

[9] M. Rosso, C. Brissot, A. Teyssot, M. Dollé, L. Sannier, J.-M. Tarascon, R. Bouchet, S. Lascaud, Dendrite short-circuit and fuse effect on Li/polymer/Li cells, Electrochimica Acta 51(25) (2006) 5334-5340.

[10] S. Wang, K. Rafiz, J. Liu, Y. Jin, J.Y.S. Lin, Effects of lithium dendrites on thermal runaway and gassing of LiFePO4 batteries, Sustainable Energy & Fuels 4(5) (2020) 2342-2351.

[11] J. Zhang, Q. Rao, B. Jin, J. Lu, Q.-g. He, Y. Hou, Z. Li, X. Zhan, F. Chen, Q. Zhang, Cerium oxide embedded bilayer separator enabling fast polysulfide conversion for high-performance lithium-sulfur batteries, Chemical Engineering Journal 388 (2020) 124120.

[12] H. Kuwata, H. Sonoki, M. Matsui, Y. Matsuda, N. Imanishi, Surface Layer and Morphology of Lithium Metal Electrodes, Electrochemistry 84(11) (2016) 854-860.

[13] J. Heine, P. Hilbig, X. Qi, P. Niehoff, M. Winter, P. Bieker, Fluoroethylene Carbonate as Electrolyte Additive in Tetraethylene Glycol Dimethyl Ether Based Electrolytes for Application in Lithium Ion and Lithium Metal Batteries, Journal of The Electrochemical Society 162(6) (2015) A1094-A1101.

[14] J. Guo, Z. Wen, M. Wu, J. Jin, Y. Liu, Vinylene carbonate–LiNO3: A hybrid additive in carbonic ester electrolytes for SEI modification on Li metal anode, Electrochemistry Communications 51 (2015) 59-63.

[15] R. Miao, J. Yang, X. Feng, H. Jia, J. Wang, Y. Nuli, Novel dual-salts electrolyte solution for dendrite-free lithium-metal based rechargeable batteries with high cycle reversibility, Journal of Power Sources 271 (2014) 291-297.

[16] G.-B. Han, J.-N. Lee, D.J. Lee, H. Lee, J. Song, H. Lee, M.-H. Ryou, J.-K. Park, Y.M. Lee, Enhanced cycling performance of lithium metal secondary batteries with succinic anhydride as an electrolyte additive, Electrochimica Acta 115 (2014) 525-530.

[17] H. Xiang, P. Shi, P. Bhattacharya, X. Chen, D. Mei, M.E. Bowden, J. Zheng, J.-G. Zhang, W. Xu, Enhanced charging capability of lithium metal batteries based on lithium bis(trifluoromethanesulfonyl)imide-lithium bis(oxalato)borate dual-salt electrolytes, Journal of Power Sources 318 (2016) 170-177.

[18] F. Wu, J. Qian, R. Chen, J. Lu, L. Li, H. Wu, J. Chen, T. Zhao, Y. Ye, K. Amine, An Effective Approach To Protect Lithium Anode and Improve Cycle Performance for Li–S Batteries, ACS Applied Materials & Interfaces 6(17) (2014) 15542-15549.

[19] G.A. Umeda, E. Menke, M. Richard, K.L. Stamm, F. Wudl, B. Dunn, Protection of lithium metal surfaces using tetraethoxysilane, Journal of

Materials Chemistry 21(5) (2011) 1593-1599.

[20] F. Marchioni, K. Star, E. Menke, T. Buffeteau, L. Servant, B. Dunn, F. Wudl, Protection of Lithium Metal Surfaces Using Chlorosilanes, Langmuir 23(23) (2007) 11597-11602.

[21] N.-S. Choi, Y.M. Lee, J.H. Park, J.-K. Park, Interfacial enhancement between lithium electrode and polymer electrolytes, Journal of Power Sources 119-121 (2003) 610-616.

[22] N.-S. Choi, Y.M. Lee, W. Seol, J.A. Lee, J.-K. Park, Protective coating of lithium metal electrode for interfacial enhancement with gel polymer electrolyte, Solid State Ionics 172(1) (2004) 19-24.

[23] J.H. Baik, S. Kim, D.G. Hong, J.C. Lee, Gel Polymer Electrolytes Based on Polymerizable Lithium Salt and Poly(ethylene glycol) for Lithium Battery Applications, ACS Appl Mater Interfaces 11(33) (2019) 29718-29724.

[24] J.-H. Baik, D.-G. Kim, J. Shim, J.H. Lee, Y.-S. Choi, J.-C. Lee, Solid polymer electrolytes containing poly(ethylene glycol) and renewable cardanol moieties for all-solid-state rechargeable lithium batteries, Polymer 99 (2016) 704-712.

[25] J.-H. Baik, D.-G. Kim, J.H. Lee, S. Kim, D.G. Hong, J.-C. Lee, Nonflammable and thermally stable gel polymer electrolytes based on crosslinked perfluoropolyether (PFPE) network for lithium battery applications, Journal of Industrial and Engineering Chemistry 64 (2018) 453-460.

[26] J. Shim, J.W. Lee, K.Y. Bae, H.J. Kim, W.Y. Yoon, J.C. Lee, Dendrite Suppression by Synergistic Combination of Solid Polymer Electrolyte Crosslinked with Natural Terpenes and Lithium-Powder Anode for Lithium-Metal Batteries, ChemSusChem 10(10) (2017) 2274-2283.

[27] J. Shim, H.J. Kim, B.G. Kim, Y.S. Kim, D.-G. Kim, J.-C. Lee, 2D boron nitride nanoflakes as a multifunctional additive in gel polymer electrolytes for safe, long cycle life and high rate lithium metal batteries, Energy & Environmental Science 10(9) (2017) 1911-1916.

[28] J. Shim, D.-G. Kim, H.J. Kim, J.H. Lee, J.-H. Baik, J.-C. Lee, Novel composite polymer electrolytes containing poly(ethylene glycol)-grafted graphene oxide for all-solid-state lithium-ion battery applications, J. Mater. Chem. A 2(34) (2014) 13873-13883.

[29] J. Shim, K.Y. Bae, H.J. Kim, J.H. Lee, D.G. Kim, W.Y. Yoon, J.C. Lee, Solid Polymer Electrolytes Based on Functionalized Tannic Acids from Natural Resources for All-Solid-State Lithium-Ion Batteries, ChemSusChem 8(24) (2015) 4133-8.

[30] D. Jeong, J. Shim, H. Shin, J.C. Lee, Sustainable Lignin-Derived Cross-Linked Graft Polymers as Electrolyte and Binder Materials for Lithium Metal Batteries, ChemSusChem 13(10) (2020) 2642-2649.

[31] L. Long, S. Wang, M. Xiao, Y. Meng, Polymer electrolytes for lithium polymer batteries, Journal of Materials Chemistry A 4(26) (2016) 10038-10069.

[32] C. Sun, J. Liu, Y. Gong, D.P. Wilkinson, J. Zhang, Recent advances in all-solid-state rechargeable lithium batteries, Nano Energy 33 (2017) 363-386.

[33] M. Wetjen, M.A. Navarra, S. Panero, S. Passerini, B. Scrosati, J. Hassoun, Composite Poly(ethylene oxide) Electrolytes Plasticized by N-Alkyl-N-butylpyrrolidinium Bis(trifluoromethanesulfonyl)imide for Lithium Batteries, ChemSusChem 6(6) (2013) 1037-1043.

[34] M.J. Reddy, P.P. Chu, J.S. Kumar, U.V.S. Rao, Inhibited crystallization and its effect on conductivity in a nano-sized Fe oxide composite PEO solid electrolyte, Journal of Power Sources 161(1) (2006) 535-540.

[35] Z. Wei, Y. Ren, M. Wang, J. He, W. Huo, H. Tang, Improving the Conductivity of Solid Polymer Electrolyte by Grain Reforming, Nanoscale Research Letters 15(1) (2020) 122.

[36] X. Zhan, J. Zhang, M. Liu, J. Lu, Q. Zhang, F. Chen, Advanced Polymer Electrolyte with Enhanced Electrochemical Performance for Lithium-Ion Batteries: Effect of Nitrile-Functionalized Ionic Liquid, ACS Applied Energy Materials 2(3) (2019) 1685-1694.

[37] N.A.A. Rossi, Z. Zhang, Y. Schneider, K. Morcom, L.J. Lyons, Q. Wang, K. Amine, R. West, Synthesis and Characterization of Tetra- and Trisiloxane-Containing Oligo(ethylene glycol)s Highly Conducting Electrolytes for Lithium Batteries, Chemistry of Materials 18(5) (2006) 1289-1295.

[38] W.-S. Young, T.H. Epps, Ionic Conductivities of Block Copolymer Electrolytes with Various Conducting Pathways: Sample Preparation and

Processing Considerations, Macromolecules 45(11) (2012) 4689-4697.

[39] D.-G. Kim, J. Shim, J.H. Lee, S.-J. Kwon, J.-H. Baik, J.-C. Lee, Preparation of solid-state composite electrolytes based on organic/inorganic hybrid star-shaped polymer and PEG-functionalized POSS for all-solid-state lithium battery applications, Polymer 54(21) (2013) 5812-5820.

[40] D.-G. Kim, H.-S. Sohn, S.-K. Kim, A. Lee, J.-C. Lee, Star-shaped polymers having side chain poss groups for solid polymer electrolytes; synthesis, thermal behavior, dimensional stability, and ionic conductivity, Journal of Polymer Science Part A: Polymer Chemistry 50(17) (2012) 3618-3627.

[41] J. Shim, D.G. Kim, H.J. Kim, J.H. Lee, J.C. Lee, Polymer composite electrolytes having core-shell silica fillers with anion-trapping boron moiety in the shell layer for all-solid-state lithium-ion batteries, ACS Appl Mater Interfaces 7(14) (2015) 7690-701.

[42] F. Fischer, T. Hahn, H. Bässler, I. Bauer, P. Strohriegl, A. Köhler, Measuring Reduced C60 Diffusion in Crosslinked Polymer Films by Optical Spectroscopy, Advanced Functional Materials 24(39) (2014) 6172-6177.

[43] H.-S. Ryu, D.-G. Kim, J.-C. Lee, Polysiloxanes containing polyhedral oligomeric silsesquioxane groups in the side chains; synthesis and properties, Polymer 51(11) (2010) 2296-2304.

[44] M. Liu, B. Jin, Q. Zhang, X. Zhan, F. Chen, High-performance solid polymer electrolytes for lithium ion batteries based on sulfobetaine zwitterion

and poly (ethylene oxide) modified polysiloxane, Journal of Alloys and Compounds 742 (2018) 619-628.

[45] Y. Kang, J. Lee, D.H. Suh, C. Lee, A new polysiloxane based cross-linker for solid polymer electrolyte, Journal of Power Sources 146(1) (2005) 391-396.

[46] J. Shim, L. Kim, H.J. Kim, D. Jeong, J.H. Lee, J.-C. Lee, All-solid-state lithium metal battery with solid polymer electrolytes based on polysiloxane crosslinked by modified natural gallic acid, Polymer 122 (2017) 222-231.

[47] J. Evans, C.A. Vincent, P.G. Bruce, Electrochemical measurement of transference numbers in polymer electrolytes, Polymer 28(13) (1987) 2324-2328.

[48] H. Zhang, C. Li, M. Piszcz, E. Coya, T. Rojo, L.M. Rodriguez-Martinez, M. Armand, Z. Zhou, Single lithium-ion conducting solid polymer electrolytes: advances and perspectives, Chemical Society Reviews 46(3) (2017) 797-815.

[49] Y. Zhao, L. Wang, Y. Zhou, Z. Liang, N. Tavajohi, B. Li, T. Li, Solid Polymer Electrolytes with High Conductivity and Transference Number of Li Ions for Li-Based Rechargeable Batteries, Advanced Science (2021) 2003675.

[50] C.S. Kim, S.M. Oh, Importance of donor number in determining solvating ability of polymers and transport properties in gel-type polymer electrolytes, Electrochimica acta 45(13) (2000) 2101-2109.

[51] Y. Lu, M. Tikekar, R. Mohanty, K. Hendrickson, L. Ma, L.A. Archer, Stable Cycling of Lithium Metal Batteries Using High Transference Number Electrolytes, Advanced Energy Materials 5(9) (2015) 1402073.

[52] S. Li, A.I. Mohamed, V. Pande, H. Wang, J. Cuthbert, X. Pan, H. He, Z. Wang, V. Viswanathan, J.F. Whitacre, K. Matyjaszewski, Single-Ion Homopolymer Electrolytes with High Transference Number Prepared by Click Chemistry and Photoinduced Metal-Free Atom-Transfer Radical Polymerization, ACS Energy Letters 3(1) (2018) 20-27.

[53] X. Wang, L. Peng, H. Hua, Y. Liu, P. Zhang, J. Zhao, Magnesium Borate Fiber Coating Separators with High Lithium-Ion Transference Number for Lithium-Ion Batteries, ChemElectroChem 7(5) (2020) 1187-1192.

[54] W. Liu, D. Lin, J. Sun, G. Zhou, Y. Cui, Improved Lithium Ionic Conductivity in Composite Polymer Electrolytes with Oxide-Ion Conducting Nanowires, ACS Nano 10(12) (2016) 11407-11413.

[55] C. Ma, K. Dai, H. Hou, X. Ji, L. Chen, D.G. Ivey, W. Wei, High Ion-Conducting Solid-State Composite Electrolytes with Carbon Quantum Dot Nanofillers, Advanced Science 5(5) (2018) 1700996.

[56] M. Sasikumar, M. Raja, R.H. Krishna, A. Jagadeesan, P. Sivakumar, S. Rajendran, Influence of Hydrothermally Synthesized Cubic-Structured BaTiO3 Ceramic Fillers on Ionic Conductivity, Mechanical Integrity, and Thermal Behavior of P(VDF–HFP)/PVAc-Based Composite Solid Polymer Electrolytes for Lithium-Ion Batteries, The Journal of Physical Chemistry C

122(45) (2018) 25741-25752.

[57] J.-F. Wu, X. Guo, MOF-derived nanoporous multifunctional fillers enhancing the performances of polymer electrolytes for solid-state lithium batteries, Journal of Materials Chemistry A 7(6) (2019) 2653-2659.

[58] D. Dong, H. Zhang, B. Zhou, Y. Sun, H. Zhang, M. Cao, J. Li, H. Zhou, H. Qian, Z. Lin, H. Chen, Porous covalent organic frameworks for high transference number polymer-based electrolytes, Chemical Communications 55(10) (2019) 1458-1461.

[59] T. Jiang, P. He, G. Wang, Y. Shen, C.-W. Nan, L.-Z. Fan, Solvent-Free Synthesis of Thin, Flexible, Nonflammable Garnet-Based Composite Solid Electrolyte for All-Solid-State Lithium Batteries, Advanced Energy Materials 10(12) (2020) 1903376.

[60] X. Peng, K. Huang, S. Song, F. Wu, Y. Xiang, X. Zhang, Garnet-Polymer Composite Electrolytes with High Li+ Conductivity and Transference Number via Well-Fused Grain Boundaries in Microporous Frameworks, ChemElectroChem 7(11) (2020) 2389-2394.

[61] L. Porcarelli, A.S. Shaplov, M. Salsamendi, J.R. Nair, Y.S. Vygodskii, D. Mecerreyes, C. Gerbaldi, Single-Ion Block Copoly(ionic liquid)s as Electrolytes for All-Solid State Lithium Batteries, ACS Applied Materials & Interfaces 8(16) (2016) 10350-10359.

[62] J. Shim, J.S. Lee, J.H. Lee, H.J. Kim, J.C. Lee, Gel Polymer Electrolytes Containing Anion-Trapping Boron Moieties for Lithium-Ion Battery

Applications, ACS Appl Mater Interfaces 8(41) (2016) 27740-27752.

[63] G. Chen, C. Niu, X. Liao, Y. Chen, W. Shang, J. Du, Y. Chen, Boron-containing single-ion conducting polymer electrolyte for dendrite-free lithium metal batteries, Solid State Ionics 349 (2020) 115309.

[64] D. Li, X. Ji, X. Gong, F. Tsai, Q. Zhang, L. Yao, T. Jiang, R.K.Y. Li, H. Shi, S. Luan, D. Shi, The synergistic effect of poly(ethylene glycol)-borate ester on the electrochemical performance of all solid state Si doped-poly(ethylene glycol) hybrid polymer electrolyte for lithium ion battery, Journal of Power Sources 423 (2019) 349-357.

[65] K. Dai, C. Ma, Y. Feng, L. Zhou, G. Kuang, Y. Zhang, Y. Lai, X. Cui, W. Wei, A borate-rich, cross-linked gel polymer electrolyte with near-single ion conduction for lithium metal batteries, Journal of Materials Chemistry A 7(31) (2019) 18547-18557.

[66] J. Zhang, C. Ma, H. Hou, X. Li, L. Chen, D.G. Ivey, W. Wei, A star-shaped solid composite electrolyte containing multifunctional moieties with enhanced electrochemical properties for all solid-state lithium batteries, Journal of Membrane Science 552 (2018) 107-114.

[67] L. Fan, S. Wei, S. Li, Q. Li, Y. Lu, Recent Progress of the Solid-State Electrolytes for High-Energy Metal-Based Batteries, Advanced Energy Materials 8(11) (2018) 1702657.

[68] J. Shim, D.-G. Kim, J.H. Lee, J.H. Baik, J.-C. Lee, Synthesis and properties of organic/inorganic hybrid branched-graft copolymers and their

application to solid-state electrolytes for high-temperature lithium-ion batteries, Polym. Chem. 5(10) (2014) 3432-3442.

[69] L. Xu, W. Wei, D. You, H. Xiong, J. Yang, Ion conduction in the comb-branched polyether electrolytes with controlled network structures, Soft Matter 16(8) (2020) 1979-1988.

[70] M.L. Lehmann, G. Yang, J. Nanda, T. Saito, Well-designed Crosslinked Polymer Electrolyte Enables High Ionic Conductivity and Enhanced Salt Solvation, Journal of The Electrochemical Society 167(7) (2020) 070539.

[71] J. Jiang, H. Pan, W. Lin, W. Tu, H. Zhang, UV-induced semi-interpenetrating polymer electrolyte membrane for elevated-temperature all-solid-state lithium-ion batteries, Materials Chemistry and Physics 236 (2019) 121781.

[72] M. Falco, C. Simari, C. Ferrara, J.R. Nair, G. Meligrana, F. Bella, I. Nicotera, P. Mustarelli, M. Winter, C. Gerbaldi, Understanding the Effect of UV-Induced Cross-Linking on the Physicochemical Properties of Highly Performing PEO/LiTFSI-Based Polymer Electrolytes, Langmuir 35(25) (2019) 8210-8219.

[73] S.-J. Kwon, D.-G. Kim, J. Shim, J.H. Lee, J.-H. Baik, J.-C. Lee, Preparation of organic/inorganic hybrid semi-interpenetrating network polymer electrolytes based on poly(ethylene oxide-co-ethylene carbonate) for all-solid-state lithium batteries at elevated temperatures, Polymer 55(12) (2014) 2799-2808.

[74] S. Zhang, Z. Li, Y. Guo, L. Cai, P. Manikandan, K. Zhao, Y. Li, V.G. Pol, Room-temperature, high-voltage solid-state lithium battery with composite solid polymer electrolyte with in-situ thermal safety study, Chemical Engineering Journal 400 (2020) 125996.

[75] S. Xia, B. Yang, H. Zhang, J. Yang, W. Liu, S. Zheng, Ultrathin Layered Double Hydroxide Nanosheets Enabling Composite Polymer Electrolyte for All-Solid-State Lithium Batteries at Room Temperature, Advanced Functional Materials 31(28) (2021) 2101168.

[76] J. Wang, J. Yang, L. Shen, Q. Guo, H. He, X. Yao, Synergistic Effects of Plasticizer and 3D Framework toward High-Performance Solid Polymer Electrolyte for Room-Temperature Solid-State Lithium Batteries, ACS Applied Energy Materials 4(4) (2021) 4129-4137.

[77] J. Castillo, A. Santiago, X. Judez, I. Garbayo, J.A. Coca Clemente, M.C. Morant-Miñana, A. Villaverde, J.A. González-Marcos, H. Zhang, M. Armand, C. Li, Safe, Flexible, and High-Performing Gel-Polymer Electrolyte for Rechargeable Lithium Metal Batteries, Chemistry of Materials 33(22) (2021) 8812-8821.

[78] K. Dai, Y. Zheng, W. Wei, Organoboron-Containing Polymer Electrolytes for High-Performance Lithium Batteries, Advanced Functional Materials 31(13) (2021) 2008632.

[79] R. Khurana, J.L. Schaefer, L.A. Archer, G.W. Coates, Suppression of Lithium Dendrite Growth Using Cross-Linked Polyethylene/Poly(ethylene

oxide) Electrolytes: A New Approach for Practical Lithium-Metal Polymer Batteries, Journal of the American Chemical Society 136(20) (2014) 7395-7402.

[80] Y. He, J. Wang, Y. Zhang, S. Huo, D. Zeng, Y. Lu, Z. Liu, D. Wang, H. Cheng, Effectively suppressing lithium dendrite growth via an es-LiSPCE single-ion conducting nano fiber membrane, Journal of Materials Chemistry A 8(5) (2020) 2518-2528.

[81] S. Tang, X.-G. Zhang, X.-Y. Cui, H.-Y. Xu, D.-Y. Wu, J.-W. Yan, M.-S. Zheng, Q.-F. Dong, B.-W. Mao, Mitigating concentration polarization for highly reversible plating/stripping electrochemistry: Li versus Na, Journal of Materials Chemistry A 7(40) (2019) 23216-23224.

[82] W. Chen, Y. Hu, W. Lv, T. Lei, X. Wang, Z. Li, M. Zhang, J. Huang, X. Du, Y. Yan, W. He, C. Liu, M. Liao, W. Zhang, J. Xiong, C. Yan, Lithiophilic montmorillonite serves as lithium ion reservoir to facilitate uniform lithium deposition, Nature Communications 10(1) (2019) 4973.

[83] Y. Zheng, X. Li, W.R. Fullerton, Q. Qian, M. Shang, J. Niu, C.Y. Li, Interpenetrating Network-Based Hybrid Solid and Gel Electrolytes for High Voltage Lithium Metal Batteries, ACS Applied Energy Materials 4(6) (2021) 5639-5648.

[84] F.J. Simon, M. Hanauer, F.H. Richter, J. Janek, Interphase Formation of PEO20:LiTFSI–Li6PS5Cl Composite Electrolytes with Lithium Metal, ACS Applied Materials & Interfaces 12(10) (2020) 11713-11723.

Table 2.1. Sample composition and properties of CSPE-Bs[a] and CSPE-BFs[a].

Sample	Molar ratio				Properties				
	Thiol in BPTS[b]	Cross-linker	Allyl PEG	LiTFSI ([Li]/[EO] = 0.07)	T_g (°C)	$T_{d,1\%}$[c] (°C)	σ[d] (S cm^{-1})	E_d[e] (V)	t_{Li^+}[d]
PE-B0[f]	3.0	0	3.0	1.51	-61.9	130	-	-	-
CSPE-B20	3.0	0.2[g]	2.4	1.47	-57.1	191	-	-	-
CSPE-B40	3.0	0.4[g]	1.8	1.43	-53.4	190	-	-	-
CSPE-B50	3.0	0.5[g]	1.5	1.41	-50.7	225	2.2×10^{-4}	5.00	0.32
CSPE-B60	3.0	0.6[g]	1.2	1.39	-49.4	225	1.3×10^{-4}	5.00	0.35
CSPE-B80	3.0	0.8[g]	0.6	1.34	-44.4	227	5.2×10^{-5}	5.00	0.37
CSPE-B100	3.0	1.0[g]	0	1.30	-38.4	230	6.0×10^{-6}	5.13	0.38
CSPE-BF20	3.0	0.2[h]	2.4	1.41	-50.2	203	2.7×10^{-4}	4.85	0.13
CSPE-BF40	3.0	0.4[h]	1.8	1.30	-42.6	199	1.7×10^{-4}	4.96	0.15
CSPE-BF60	3.0	0.6[h]	1.2	1.19	-33.9	225	6.2×10^{-5}	4.96	0.16
CSPE-BF80	3.0	0.8[h]	0.6	1.09	-24.3	242	2.1×10^{-5}	4.93	0.16
CSPE-BF100	3.0	1.0[h]	0	0.98	-23.1	289	1.2×10^{-5}	5.23	0.16

[a] 10 wt% of DMPA added compared to BPTS.

[b] the molar amount of thiol in BPTS was calculated using the average molecular weight of the repeating units containing thiol.

[c] Decomposition temperature for 1 wt% loss.

[d] At 60 °C.

[e] Decomposition voltage at 60 °C.

[f] PE-B0 is polymer electrolyte without cross-linker.

[g] BPC is the cross-linker.

[h] TMPETA is the cross-linker.

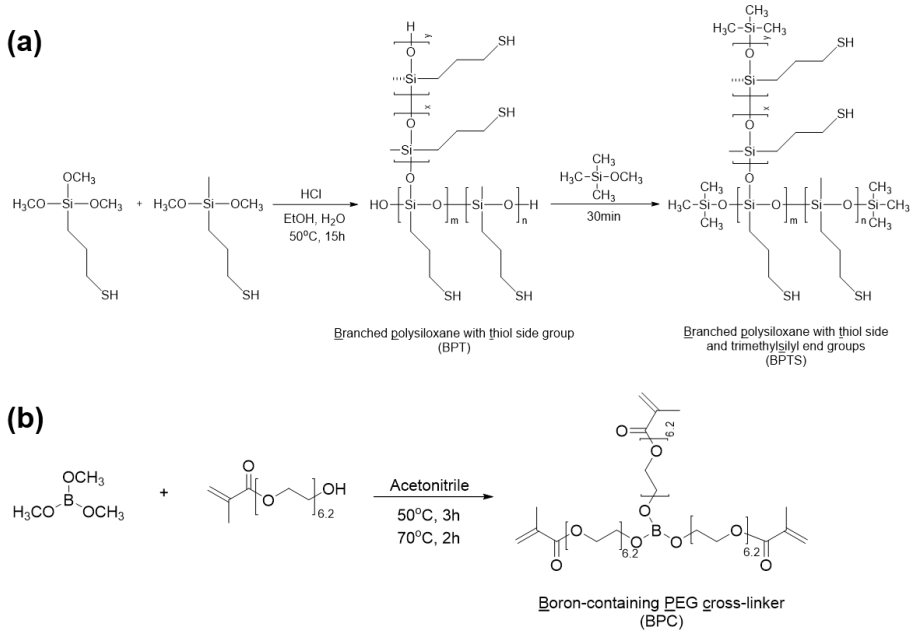

Figure 2.1. The synthetic scheme of (a) BPTS and (b) BPC.

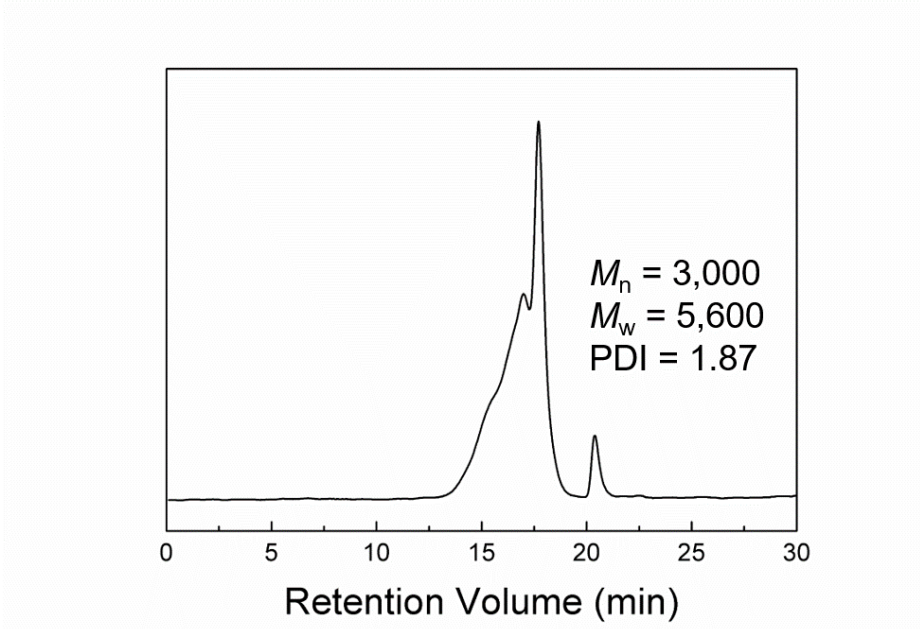

Figure 2.2. GPC profile of BPTS.

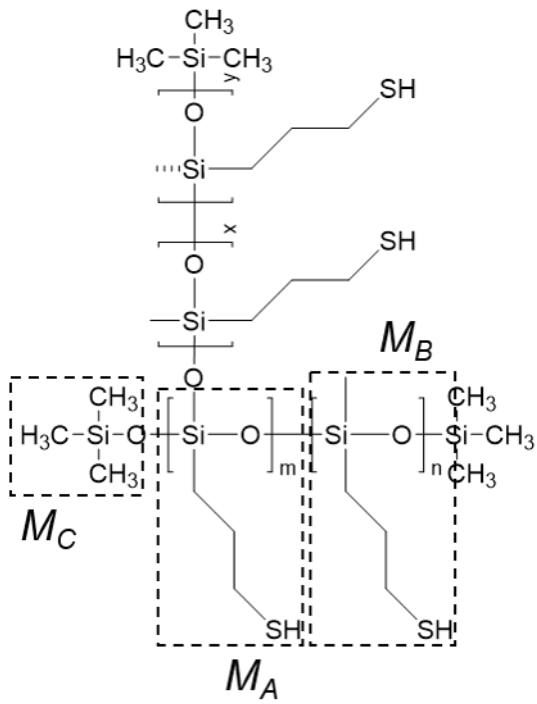

Figure 2.3. Repeating units and end group of BPTS.

▶ Calculation of average molecular weight of the repeating units containing thiol in BPTS (M_{avg})

The average molecular weight of the repeating units containing thiol in BPTS (M_{avg}) can be calculated using the following equation;

$$M_{avg} = w_A M_A + w_B M_B$$

where M_A is the molecular weight of repeating unit A [–Si($CH_2CH_2CH_2SH$)–O–] (119.2 g mol^{-1}), M_B is the molecular weight of repeating unit B [–Si($CH_2CH_2CH_2SH$)CH_3–O–] (134.3 g mol^{-1}), M_C is the

molecular weight of end group C [–Si((CH$_3$O)$_3$)] (73.2 g mol^{-1}) (Figure 2.3). w_A and w_B are the weight fractions of repeating unit A and B, respectively. The weight fraction of each repeating unit can be obtained through the following equation;

$$w_A = \frac{y_A M_A}{y_A M_A + y_B M_B + y_C M_C}, w_B = \frac{y_B M_B}{y_A M_A + y_B M_B + y_C M_C}$$

where, y_A, y_B, and y_C are molar ratios of repeating unit A, B, and end group C, respectively. Since equimolar amount of trimethoxysilane and dimethoxymethylsilane was used for the polymerization, unit A and unit B have the same molar amount, and y_C can be obtained by the following equation

$$y_C = \frac{I_a - I_{CH_3,B}}{n_{H,C}}$$

where I_a is an integral value of peak *a* from CH$_3$ in the ^{1}H NMR spectrum of BPTS, $I_{CH_3,B}$ is an integral value of CH$_3$ in unit B, and $n_{H,C}$ is the number of hydrogen atoms in end group C. Therefore, M_{avg} can be obtained by the following equation.

$$M_{avg} = \frac{M_A}{M_A + M_B + \left(\frac{I_a - I_{CH_3,B}}{n_{H,C}}\right) \times M_C} \times M_A + \frac{M_B}{M_A + M_B + \left(\frac{I_a - I_{CH_3,B}}{n_{H,C}}\right) \times M_C} \times M_B$$

Therefore, M_{avg} value in this study can be obtained using the integral values

obtained from the ^{1}H NMR spectrum of BPTS (Figure 2.4). For example, if y_A and y_B are 1, respectively, and the integral value of the b peak in the NMR spectrum is 4, then the $I_{CH_3,B}$ value is 3. Since $n_{H,C}$ is 9 and I_a value is 6 in the ^{1}H NMR spectrum, the M_{avg} is 116.03 g mol^{-1}.

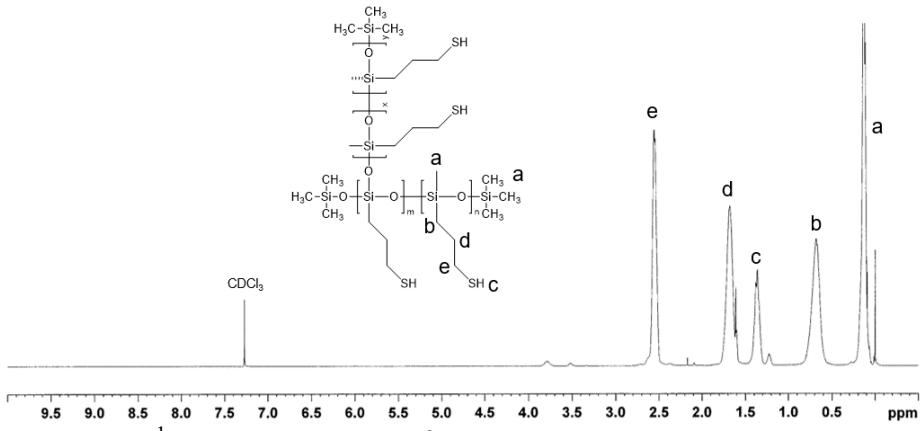

Figure 2.4. ^{1}H NMR spectrum of BPTS.

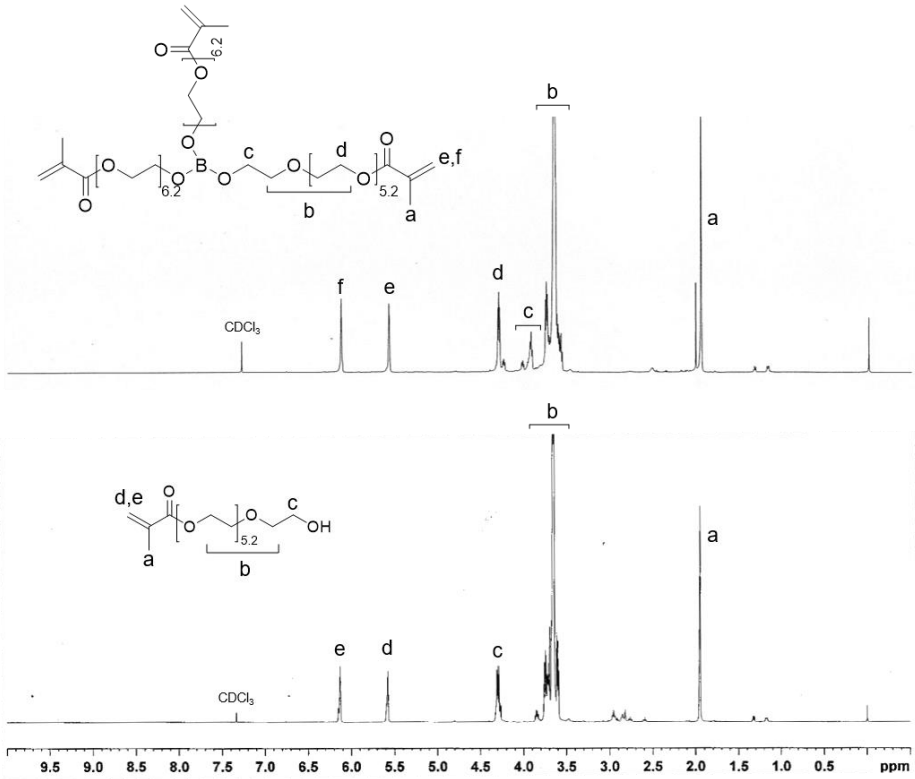

Figure 2.5. ^{1}H NMR spectra of BPC and PEGMA.

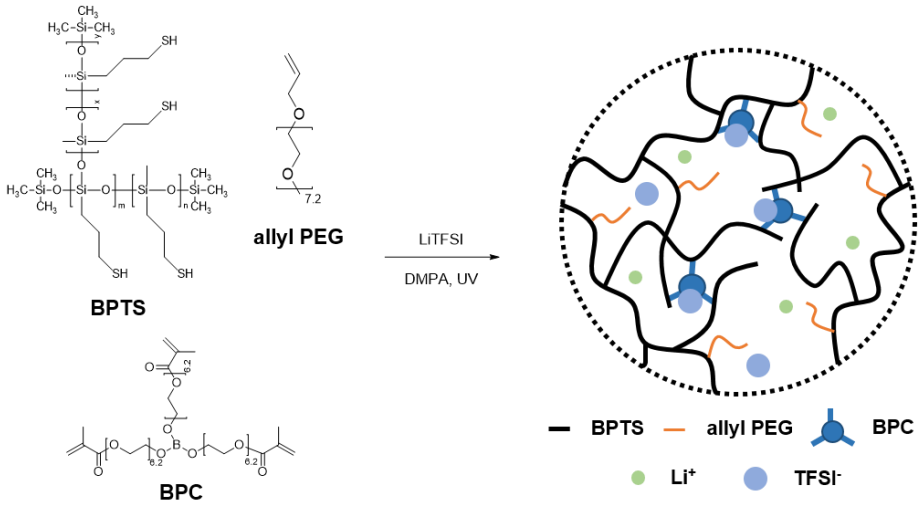

Figure 2.6. Preparation of solid polymer electrolytes based on hyperbranched polysiloxane (BPTS) and anion-trapping boron cross-linker (BPC).

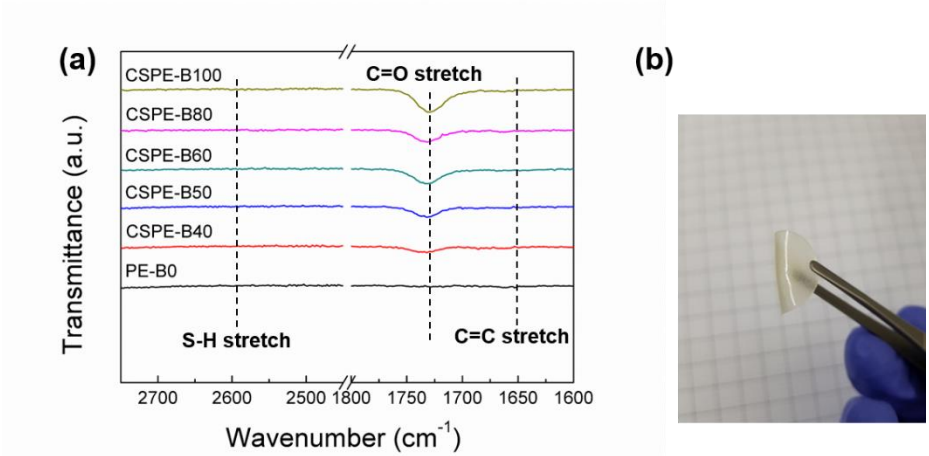

Figure 2.7. FT-IR spectra of CSPE-Bs and PE-B0 in the range of 2750–1600 cm^{-1}, (b) photograph of free-standing CSPE-B60.

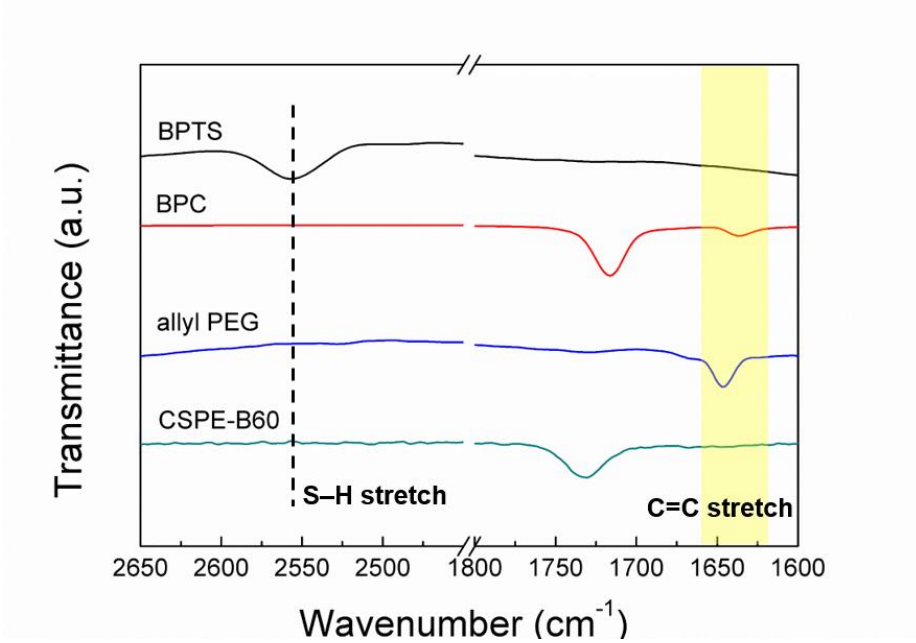

Figure 2.8. FT-IR spectra of BPTS, BPC, allyl PEG, and CSPE-B60 in the range of 2650–1600 cm^{-1}.

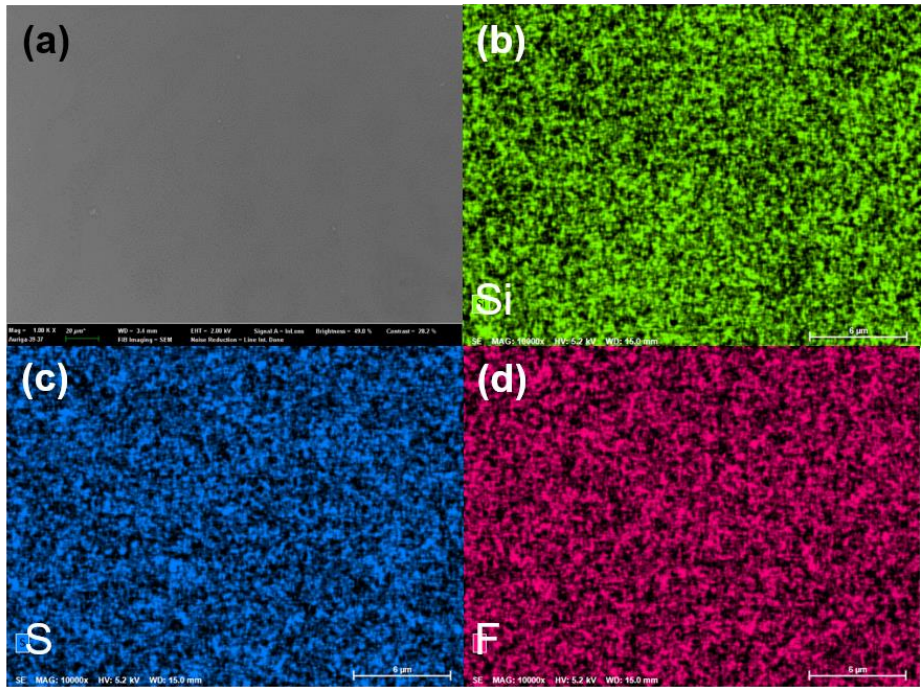

Figure 2.9. SEM and EDS images of CSPE-B60.

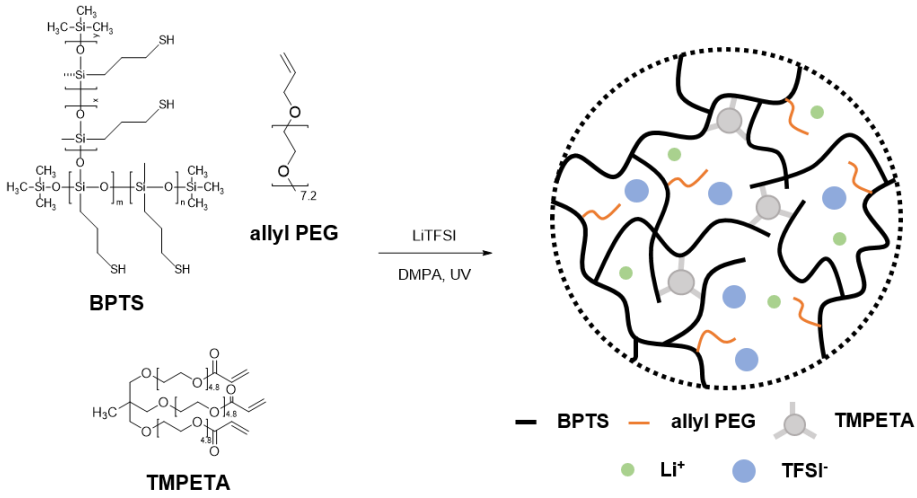

Figure 2.10. Preparation of CSPE-BFs.

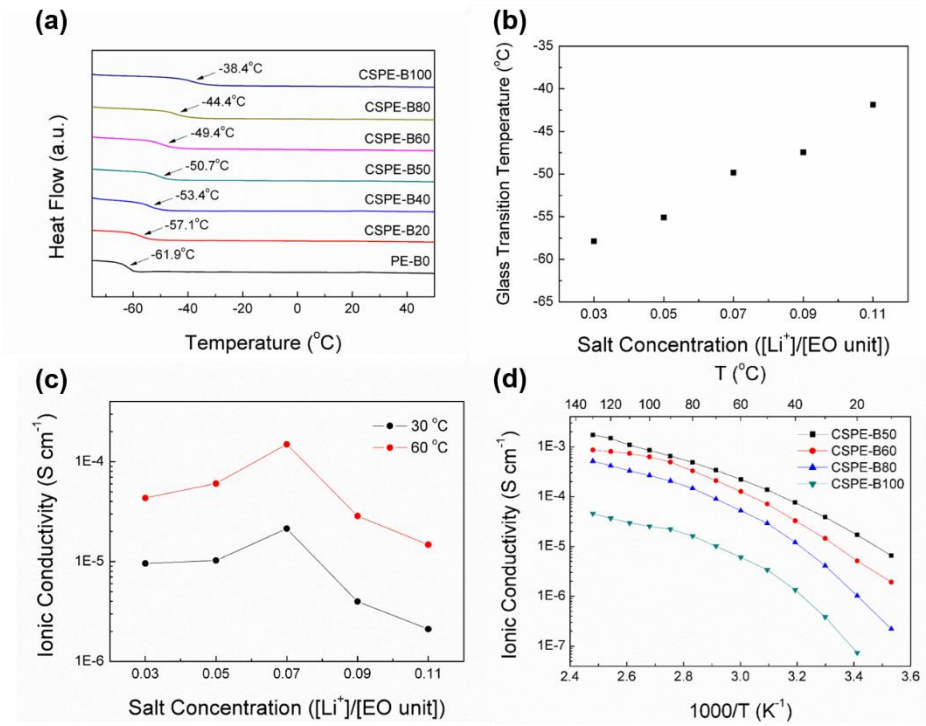

Figure 2.11. (a) DSC thermograms of CSPE-Bs and PE-B0 ([Li^+]/[EO unit] = 0.07). (b) Glass transition temperatures of CSPE-B60 with various lithium salt concentrations. (c) Ionic conductivities of CSPE-B60 with various lithium salt concentrations at 30 °C and 60 °C. (d) Ionic conductivities of CSPE-Bs at various temperatures ([Li^+]/[EO unit] = 0.07).

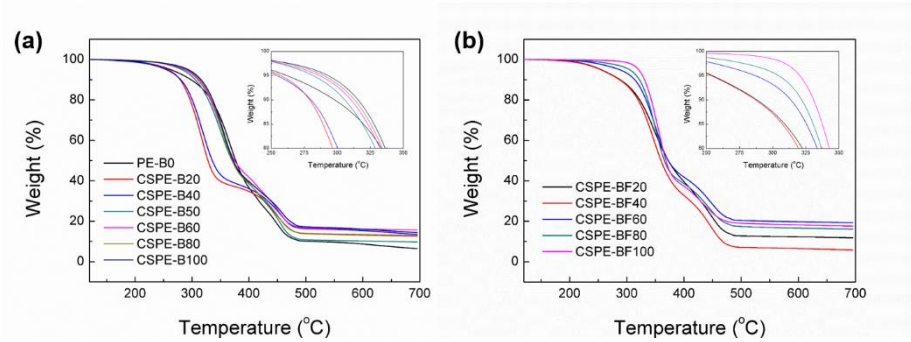

Figure 2.12. TGA curves of (a) CSPE-Bs with PE-B0 and (b) CSPE-BFs.

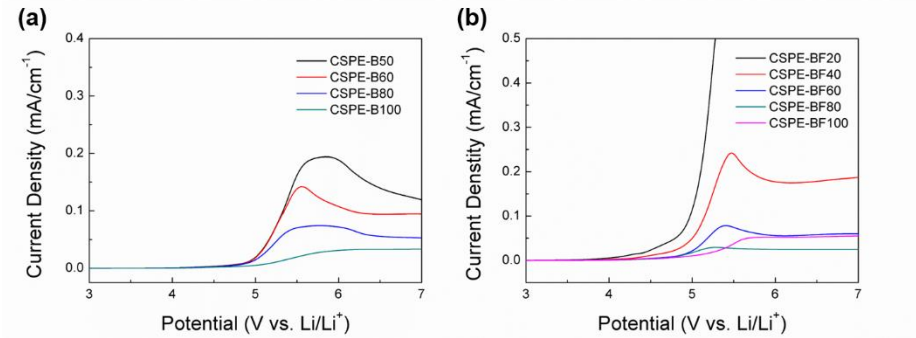

Figure 2.13. Linear sweep voltammogram of (a) CSPE-Bs and (b) CSPE-BFs at 60 °C with a scan rate of 1 mV s^{-1}.

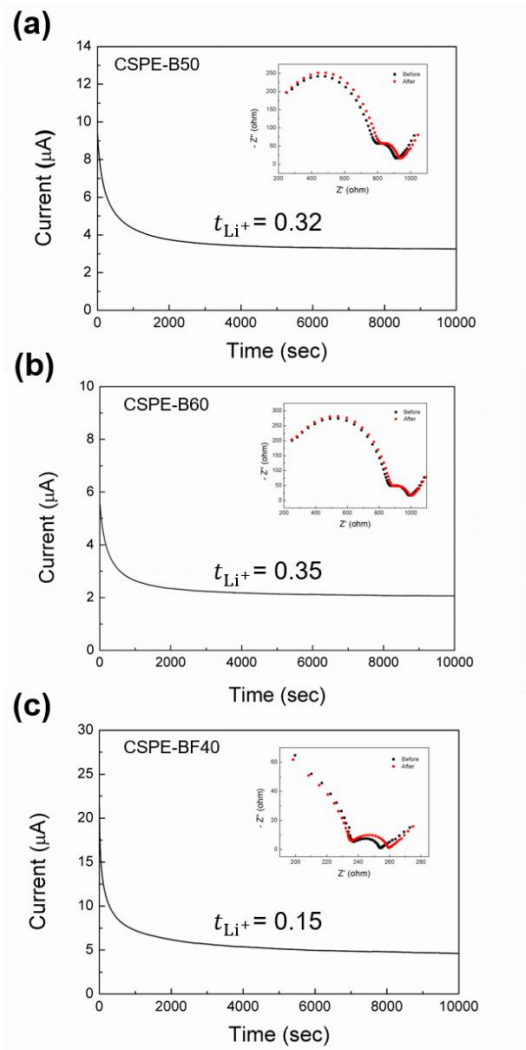

Figure 2.14. Chronoamperometric curves of (a) Li/CSPE-B50/Li cell, (b) Li/CSPE-B60/Li cell, and (c) Li/CSPE-BF40/Li cell (inset: corresponding electrochemical impedance spectra before and after polarization)

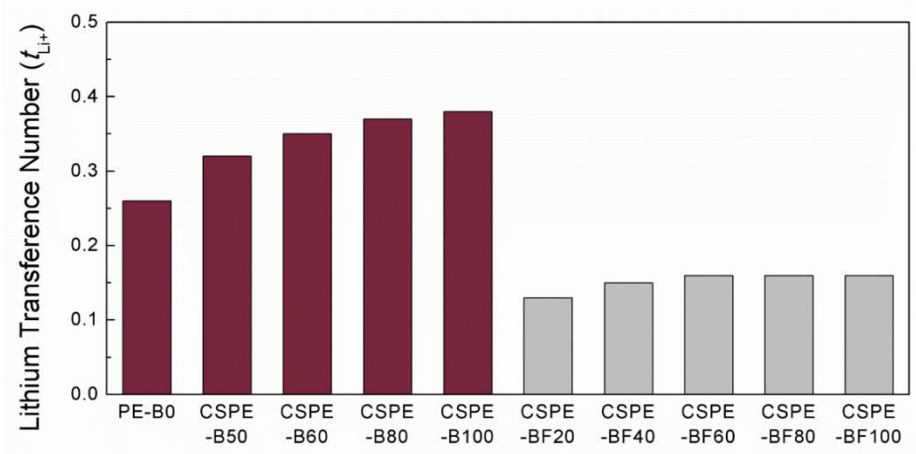

Figure 2.15. t_{Li^+} of polymer electrolytes at 60 °C.

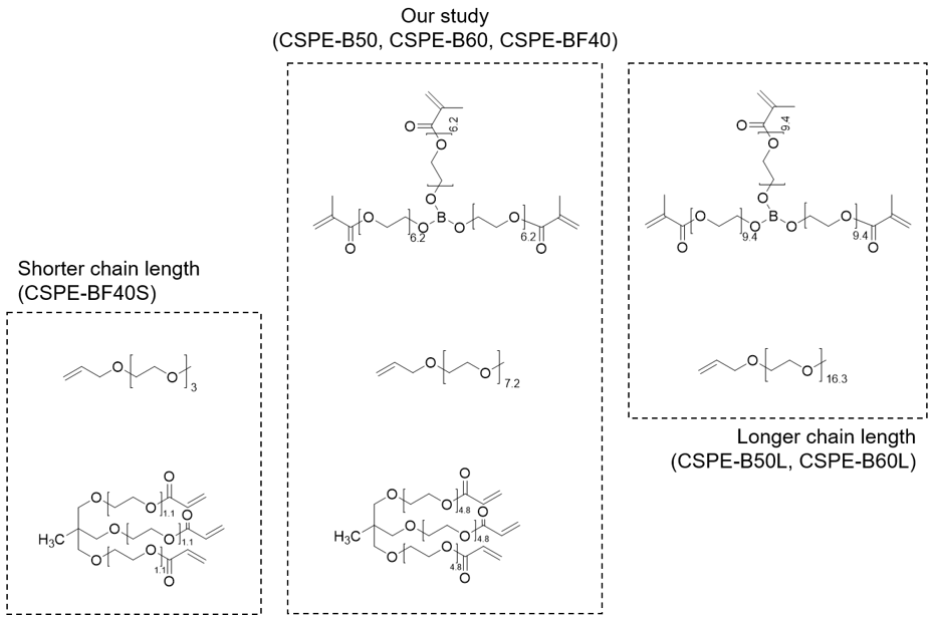

Figure 2.16. Components of CSPEs with different PEG chain length.

▶ Investigation of the effect of PEG chain length on the ionic conductivity and the t_{Li^+} values in the SPEs

SPEs with the boron-containing cross-linker having longer oligo(ethylene oxide) (CSPE-B50L and CSPE-B60L) were synthesized using the same molar ratios that used for CSPE-B50 and CSPE-B60, respectively. SPEs with shorter oligo(ethylene oxide) without any boron moiety (CSPE-BF40S) were also synthesized from the same manner used for the synthesis of CSPE-BF40. The ionic conductivity values of CSPE-B50L and CSPE-B60L were found to be larger than those of CSPE-B50 and CSPE-B60, respectively, and the ionic conductivity values of CSPE-BF40S were smaller than those of CSPE-BF40

(Figure 2.17.(a)). The t_{Li^+} values of CSPE-B50L and CSPE-B60L were smaller than those of CSPE-B50 and CSPE-B60 (Figure 2.17.(b)). The t_{Li^+} value of CSPE-BF40S was larger than that of CSPE-BF40 because the densely cross-linked structure can decrease the mobility of relatively large anions, as we mentioned in manuscript. Therefore, the PEG lengths of BPC and allyl PEG were determined based on the previous results.

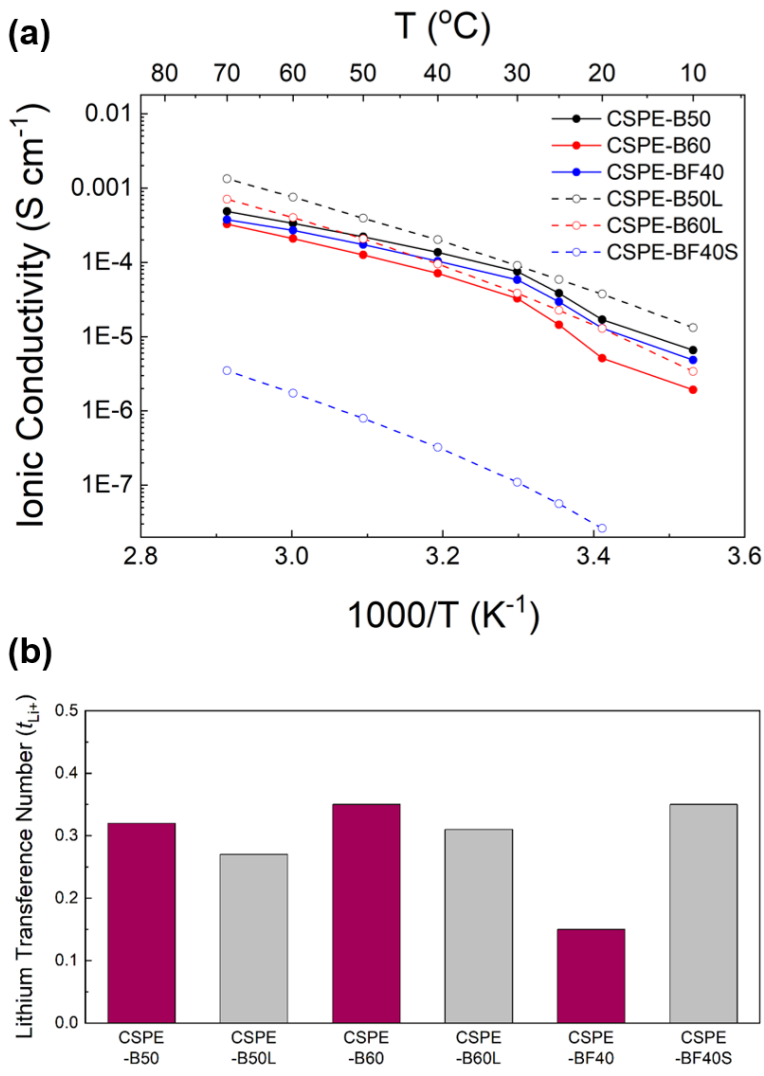

Figure 2.17. (a) Ionic conductivities of CSPEs with different PEG chain length at various temperatures. (b) t_{Li^+} values of CSPEs with different PEG chain length at 60 °C.

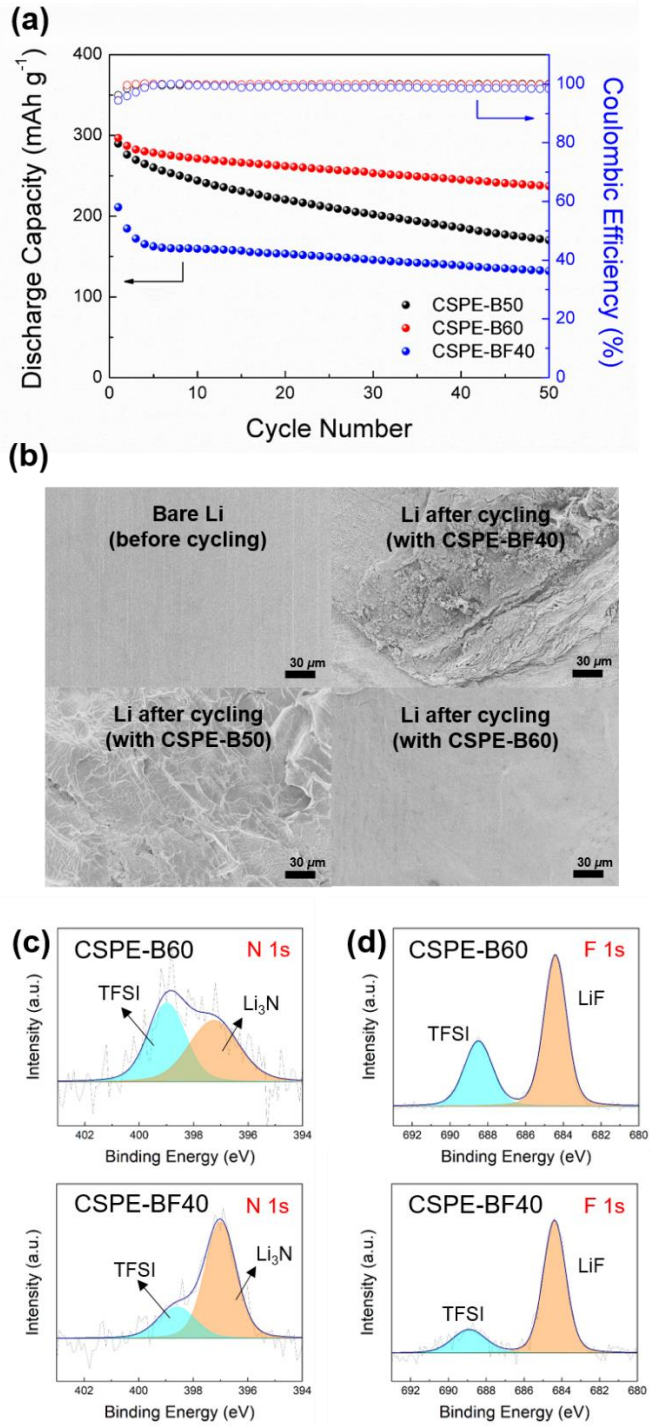

Figure 2.18. (a) Specific discharge capacity and Coulombic efficiency of the V_2O_5/CSPE/Li cells cycled at 60 °C with a rate of 0.1 C. (b) Surface SEM

images of bare lithium metal before cycling and those of the cells with CSPE-BF40, CSPE-B50, and CSPE-B60, respectively, after 50 cycles. XPS spectra of (c) N 1s and (d) F 1s from the lithium metal anode of the V_2O_5/CSPE/Li cells with CSPE-B60 and CSPE-BF40 after cycling for 50 cycles at 60 °C with a rate of 0.1 C.

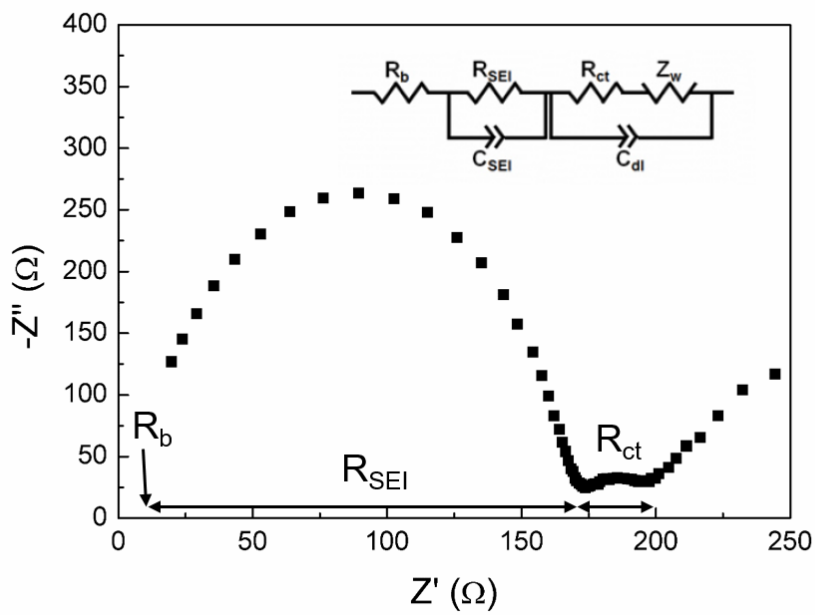

Figure 2.19. Nyquist plot of V_2O_5/CSPE-B60/Li cell at 60 °C.

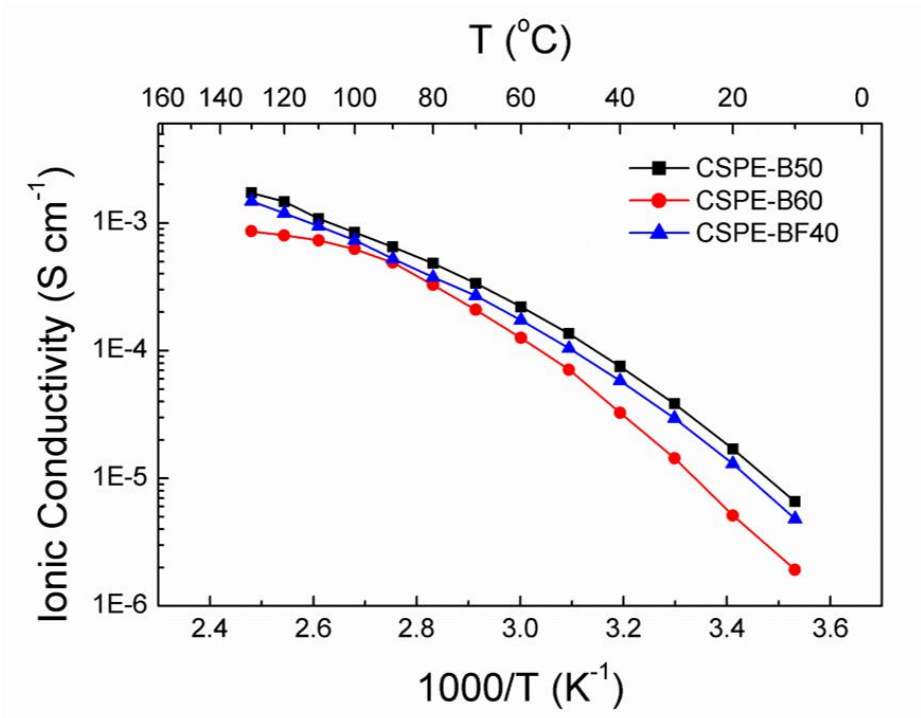

Figure 2.20. Ionic conductivities of CSPE-BF40, CSPE-B50, and CSPE-B60 at various temperatures ($[Li^+]$/[EO unit] = 0.07).

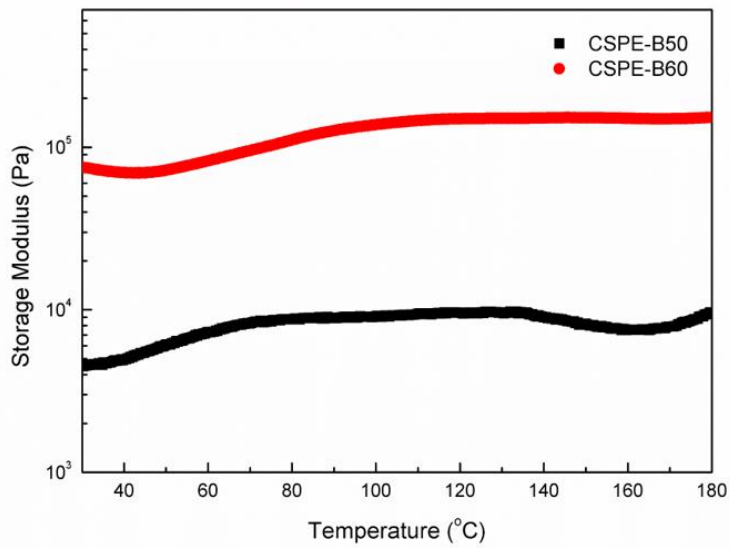

Figure 2.21. Storage modulus profiles of CSPE-B50 and CSPE-B60.

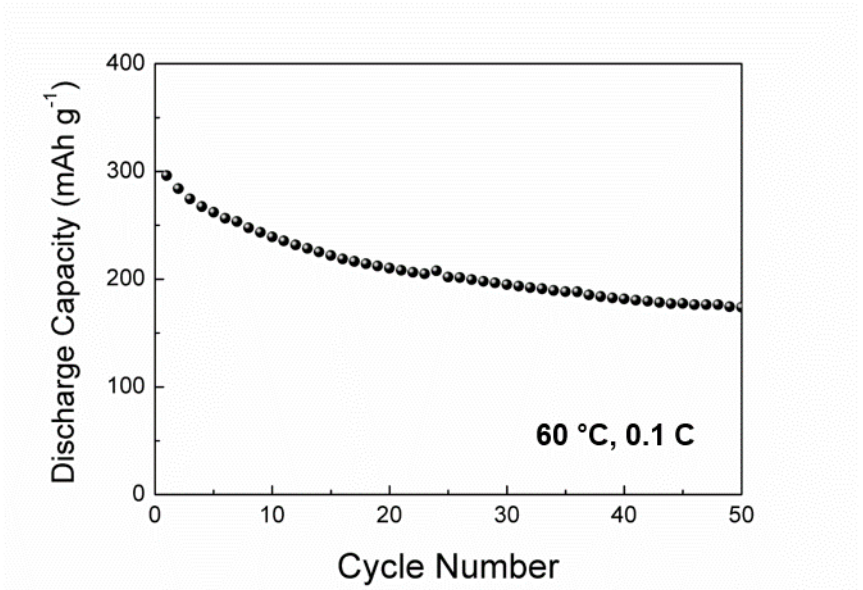

Figure 2.22. Specific discharge capacity of the V_2O_5/PP separator-LE/Li cells cycled at 60 °C with a rate of 0.1 C. (LE: 1M $LiPF_6$ EC/DMC, 1:1 v/v)

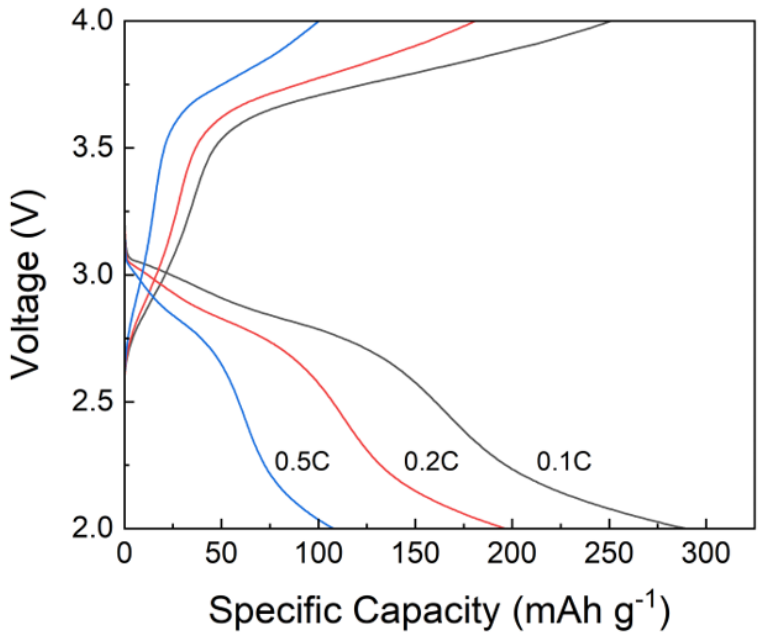

Figure 2.23. Charge-discharge profiles of V_2O_5/CSPE-B60/Li cell cycled at 60 °C with various rates.

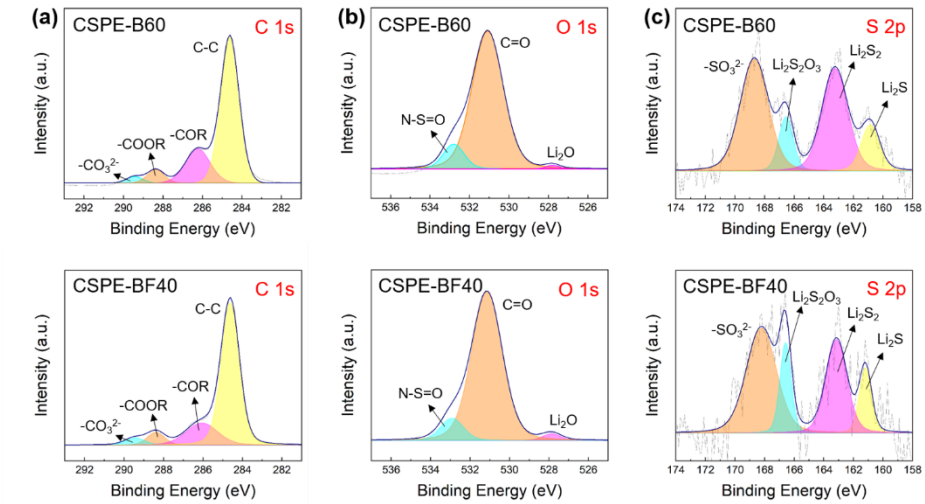

Figure 2.24. XPS spectra of (a) C 1s, (b) O 1s, and (c) S 2p from the lithium metal anode of the V_2O_5/CSPE/Li cells with CSPE-B60 and CSPE-BF40 after cycling for 50 cycles at 60 °C with a rate of 0.1 C.

Chapter 3

Ion-Conducting Cross-linked Polyphosphazene Binders for High-Performance Silicon Anodes in Lithium-Ion Batteries

3.1 Introduction

With increasing development of electric vehicles, portable devices, and energy storage systems, considerable attention is being paid to improving the energy density of lithium-ion batteries (LIBs). [1-3] Graphite-based materials are the most commonly used materials for anodes in commercial LIBs; however, improvement of their energy density is limited owing to their relatively low theoretical capacities (e.g., capacity = 372 mAh g^{-1} based on LiC_6). [4] Silicon has been regarded as a promising anode material owing to its high theoretical capacity (4,200 mAh g^{-1}), low discharge potential (~0.3 V vs. Li/Li^+), and natural abundance. [5-7] However, Si undergoes a significant volume change of up to 300 % during charging/discharging, which causes degradation of the electrode structure and formation of a thick solid–electrolyte interface (SEI) layer, which is critical disadvantage for the practical application of Si anodes. [8, 9] One of the main strategies to mitigate the volume change of Si is adopting nanostructured Si as the anode material, such as yolk–shell nanoparticles, [10, 11] nanowires, [12, 13] and nanoporous structures. [14, 15] However, although nanostructured Si anodes have been known to reduce Si volume expansion to some extent, the commercialization of these materials is challenging because of high production cost and the difficulty of scaling-up the fabrication process. [16]

Another promising approach to overcoming the volume expansion problem

of Si and maintaining the structural integrity of the Si anode is the use of polymeric binders that have functional groups such as hydroxyl and/or carboxylic acid groups, which can interact with silanol groups (Si–OH) on the Si particles via hydrogen bonding. [4, 17, 18] Poly(vinylidene fluoride) (PVDF) is the most commonly used material for LIB binders; however, when it is used in binders for Si anodes, the interface between the polymer and the Si surface is easily disrupted during the charging/discharging, which, accompanied by the volume change of Si, results in the severe degradation of battery performance. [19, 20] However, when poly(acrylic acid) (PAA), [21] carboxymethyl cellulose (CMC), [22] and polysaccharides, [23-25] which contain hydrogen bonding functional groups, are used as the binder, their interaction with the surface of the Si particles is improved, which helps maintain the structural integrity of the electrode. Polymeric binders with cross-linked structures have also been known to improve the performance of batteries with Si anodes because of the enhanced mechanical strength and adhesion strength imparted by the structure, which can help preserve the structural integrity of the Si anode. [22, 26, 27] Binders with ion-conducting moieties, including ethylene oxide, can also improve the performance of the Si anode by promoting the transport of lithium ions between the Si particle surface and the binder. [18, 28, 29]

Polyphosphazenes are inorganic polymers that comprise a backbone of alternating phosphorus and nitrogen atoms, and two organic side groups

attached to each phosphorus atom. [30] The inorganic phosphorus–nitrogen backbone imparts polyphosphazenes with excellent thermal stability, while the backbone structure simultaneously has very high chain flexibility owing to the low barrier energy to torsion (0.1–0.5 kcal/repeating unit). [31, 32] In addition, as two organic side groups can be introduced per phosphazene repeat unit via chlorine substitution, polyphosphazenes with diverse physical and chemical characteristics have been prepared and used in various applications, including in the fields of engineering and biomedicine. [33-35] Polyphosphazenes with different structures have also been used as polymeric materials in lithium secondary batteries, including as polymer electrolytes, [36, 37] electrode materials, [38, 39] and interlayers for Li−S batteries. [40]

In this study, polyphosphazene-based binders with hydrogen-bonded carboxylic acids and ion-conducting PEG groups were prepared for the first time for use as binder materials in Si anode-based lithium-ion batteries. We believed that the cross-linked structure of the binders and the hydrogen bonds between polyphosphazene and the Si surface could maintain the structural integrity of the electrode and reduce structural damage during battery cycles. The overall characteristics of the prepared binders with different cross-linking densities, including the thermal, mechanical, and electrochemical properties, were investigated. We found that the presence of carboxylic acid groups in the binder was beneficial for maintaining the structural integrity of the electrode, and that PEG moieties promoted lithium-ion conduction in the

electrode, resulting in better Si anodic performance (Figure 3.1).

3.2 Experimental

Materials

Hexachlorocyclotriphosphazene (HCCP) was purchased from Shandong Look Chemical (China) and used after vacuum sublimation at 60 °C. Poly(dichlorophosphazene) (PDCP) was synthesized via thermal ring-opening polymerization of HCCP with a catalyst (sulfamic acid) and a promoter ($CaSO_4 \cdot 2H_2O$) according to a previously reported method; [41] the prepared PDCP was used after dissolving in dry 1,4-dioxane. 1,2,4-trichlorobenzene (Merck), ammonium hydroxide solution (NH_4OH; 28.0 wt%, Merck), poly(acrylic acid) (PAA; average $M_v = 450{,}000$ g mol^{-1}; Merck), Super P (Alfa Aesar), silicon powder (average particle size = ~100 nm), and poly(ethylene glycol) bisamine (PEG-NH_3, M_n = 1,000; Alfa Aesar) were used as received. Sulfamic acid (Merck) and $CaSO_4 \cdot 2H_2O$ (Merck) were stored under vacuum before use. Ethyl 4-hydroxybenzoate (Merck) was dissolved in 1,4-dioxane and dried over a 3 Å molecular sieve prior to use. Sodium hydride (Merck) and potassium tert-butoxide (Alfa Aesar) were stored in an argon-filled glove box (H_2O < 0.5 ppm, O_2 < 0.5 ppm). Tetrahydrofuran (THF) was distilled over sodium/benzophenone under a nitrogen atmosphere. 1,4-Dioxane (Daejung) was dried over a 3 Å molecular

sieve prior to use. All other reagents and solvents were obtained from reliable commercial sources and used as received.

Synthesis of poly[bis(4-(ethoxycarbonyl)phenoxy)phosphazene] (PEPP)

Poly[bis(4-(ethoxycarbonyl)phenoxy)phosphazene] (PEPP) was synthesized via the substitution of chlorine atoms in PDCP with ethyl 4-hydroxybenzoate sodium salt. [42] Ethyl 4-hydroxybenzoate sodium salt was prepared by mixing sodium hydride (4.1 g, 0.1 mol) and ethyl 4-hydroxybenzoate (20.6 g, 0.12 mol) in dry dioxane (50.0 mL) at 0 °C. To this solution, PDCP (3.0 g) in dioxane (200.0 mL) was added dropwise for 30 min and stirred under reflux conditions for 48 h. The resulting reaction mixture was precipitated into the distilled water and further purified by reprecipitating from the THF into hexane and methanol. Upon drying under vacuum at 25 °C for 24 h, a white-colored polymer was obtained in 76% yield. ^{1}H NMR [400 MHz, $CDCl_3$, δ (ppm), TMS ref] of PEPP: 7.43 (d, 2H, aromatic), 6.59 (d, 2H, aromatic), 4.22 (q, 2H, –CH_2–), 1.28 (t, 3H, –CH_3). ^{31}P NMR [600 MHz, $CDCl_3$, δ (ppm)] of PEPP: –20.4 (s, –P=N–). The number-average molecular weight (M_n) and weight-average molecular weight (M_w) values (5.21×10^5 and 1.73×10^6 g mol^{-1}, respectively) were determined by GPC analysis (Figure 3.2).

Synthesis of poly[bis(4-carboxyphenoxy)phosphazene] (PCPP)

Poly[bis(4-carboxyphenoxy)phosphazene] (PCPP) was synthesized by the ester hydrolysis of the ethoxycarbonyl group in PEPP. [42] In detail, 1.0 g of PEPP (2.7 mmol) in THF (20.0 mL) was added slowly to a flask containing 8.1 g of potassium *tert*-butoxide (72.0 mmol) in distilled THF (100.0 mL) at 0 °C under a nitrogen atmosphere for 5 min, following which the mixture was stirred for 40 h at 30 °C. After the reaction, the solvent was evaporated using a rotary evaporator. Then, 100 mL of deionized water was added to the reaction mixture in an ice bath. The solution was dialyzed against deionized water using a regenerated cellulose tube (MWCO = 3,500). After dialysis for 48 h, the polymer was isolated by acidification of the solution with hydrochloric acid. After being centrifuged and dried under vacuum at 25 °C for 24 h, a beige-colored polymer was obtained in 94 % yield. ^{1}H NMR [400 MHz, DMSO-d_6, δ (ppm)] of PCPP: 7.42 (s, 2H, aromatic), 6.64 (s, 2H, aromatic). ^{31}P NMR [600 MHz, DMSO-d_6, δ (ppm)] of PCPP: -20.8 (s, –P=N–). The molecular weight of PCPP could not be obtained because of the interaction between the carboxylic acid groups and the GPC column. [43] However, because the phosphazene backbone did not decompose in the reaction under basic conditions, the molecular weight of the backbone will be similar to that of PEPP. [44]

Preparation of aqueous binder solutions using PCPP and PEG-NH_3

PCPP is insoluble in water despite the presence of carboxylic acids because of the hydrophobicity of the benzene group. [45] Therefore, a 10.0 wt% aqueous solution of PCPP-NH_3 (Figure 3.3) was first prepared by mixing 0.16 g of PCPP (0.5 mmol) with 64 mg of NH_4OH solution (containing 1.1 mmol of NH_3) in 1.56 g of deionized water. A 10.0 wt% of PEG-NH_3 aqueous solution was also prepared by mixing 20 mg of PEG-NH_3 (0.02 mmol) with 0.18 g of deionized water. The two aqueous solutions were mixed at different weight ratios of PEG-NH_3 to PCPP-NH_3 between 2.5 wt% and 10.0 wt% (Table 3.1, Figure. 3.3) to produce PCG-Xs, where X indicates the wt% of PEG-NH_3 to PCPP-NH_3. For example, when 0.4 g of the PCPP-NH_3 solution and 0.03 g of the PEG-NH_3 solution are mixed, it is referred to as PCG-7.5. Lastly, the control binder PAA was dissolved in deionized water at 10.0 wt%.

Cell fabrication and electrochemical analysis

Ionic conductivities of the PCG-X binders were measured by electrochemical impedance spectroscopy (EIS) using the Zahner Elektrik IM6 apparatus in a frequency range of 0.1 mHz–1.0 MHz with an applied alternating current (AC)

voltage of 10.0 mV. Symmetric cells for the measurement were prepared by sandwiching the PCG-Xs between two stainless-steel electrodes with a liquid electrolyte to form 2032 coin cells. For electrochemical characterization, the Si particles to be used as the anode active material were dispersed in deionized water with Super P and a binder at a weight ratio of 6:2:2, respectively. The dispersed slurry was coated uniformly on a copper current collector using a doctor blade and dried at 80 °C for 24 h. To form a covalently cross-linked structure in the binder (PCG-X), the prepared electrodes were further dried at 130 °C under vacuum for 8 h. The loading amount of Si was 0.8–1.0 mg cm^{-2} in all samples. The prepared anode, separator (Celgard 2400), and Li foil were assembled in a 2032 coin cell using a liquid electrolyte containing 1.0 M lithium hexafluorophosphate ($LiPF_6$) in EC:DEC (1:1 v/v) with 10 vol% FEC. All the components were assembled in an argon-filled glove box (H_2O < 0.5 ppm, O_2 < 0.5 ppm). Cyclic voltammetry (CV) tests were performed using a WBSC3000 battery cycler (WonATech) with a cutoff voltage of 0.01–1.5 V (vs. Li/Li^+) at 25 °C with different scan rates. The lithium-ion diffusion ability of each anode was measured using the Randles-Sevcik equation [29, 46]

$$I_p = 2.69 \times 10^5 n^{1.5} A D_{Li^+}^{0.5} v^{0.5} C_{Li^+}$$

where I_p is the peak current, n is the number of electrons in the reaction, A is the area of the electrode, D_{Li^+} is the lithium ion diffusion coefficient, v is the scan rate, and C_{Li^+} is the lithium-ion concentration in the electrolyte.

Galvanostatic charge–discharge testing of the coin-type half-cells was performed using the WBCS3000 battery cycler in a voltage range of 0.01–1.5 V (*vs.* Li/Li^+) at 25 °C.

Characterization

^1H and ^{31}P nuclear magnetic resonance (NMR) spectra were obtained using JNM – ECX400 (400 MHz, JEOL) and AVANCE 600 (600 MHz, Bruker), respectively, with $CDCl_3$ and DMSO-d_6 (Cambridge Isotope Laboratories) as solvents. Molecular weights (M_n, M_w) and polydispersity index (PDI) were measured by gel permeation chromatography (GPC) apparatus equipped with quaternary pump and three columns including KF-806L, KD-806M, and GF-7M followed by a refractive index (RI) detector. The obtained data were calibrated using polystyrene standards. HPLC grade THF (Fischer) was used as an eluent at a flow rate of 1.0 mL min^{-1} at 35 °C. Thermal transition behaviors were analyzed by differential scanning calorimetry (DSC) using a DSC 25 (TA Instruments) under a nitrogen atmosphere. Samples with a typical mass of 5–10 mg were encapsulated in sealed aluminum pans. The samples were first heated to 200 °C and then cooled to –50 °C to initialize crystallization, followed by a second heating scan from –50 °C to 200 °C at a heating rate of 10 °C min^{-1}. Thermal stability was investigated by thermogravimetric analysis (TGA) using TGA 55 (TA instruments) under a

nitrogen atmosphere. The samples were placed at 120 °C for 10 min to remove any residual solvent, and then heated to 700 °C at a heating rate of 10 °C min^{-1}. Fourier transform infrared (FT-IR) spectroscopy was performed on an ALPHA II (Bruker) in the wavenumber range from 4000 to 400 cm^{-1} with a resolution of 2 cm^{-1}. X-ray photoelectron spectroscopy (XPS) measurements were performed on an AXIS-SUPRA XPS (Kratos Analytical) using Mg Ka (1254.0 eV) as the radiation source. Nano-indentation test was conducted for slide glass cast binder samples using a TI-950 (Bruker). The surface morphology of electrode samples was observed by field-emission scanning electron microscopy (FE-SEM, AURIGA, Carl Zeiss) with an accelerating voltage of 10 kV. The thickness of each electrode was measured from the cross-sectional SEM image of the samples milled by a focused ion beam (FIB, AURIGA, Carl Zeiss). For the 180° peel test, 12 × 20 mm electrode samples were attached to 3M tapes. Both ends of the samples were loaded on a universal testing machine (LS1, AMETEK), and the 3M tape was pulled at a constant displacement rate of 10 mm min^{-1} while peeling force was monitored.

3.3 Results and Discussion

Synthesis of poly[bis(4-(ethoxycarbonyl)phenoxy)phosphazene] (PEPP) and poly[bis(4-carboxyphenoxy)phosphazene] (PCPP)

Poly[bis(4-(ethoxycarbonyl)phenoxy)phosphazene] (PEPP) was prepared via the substitution reaction of PDCP with the sodium salt of ethyl 4-hydroxybenzoate (Figure 3.4.(a)). The success of the substitution reactions was confirmed using ^{1}H and ^{31}P NMR spectroscopy (Figure 3.5); the appearance of the singlet peak corresponding to the phosphorous atom of PEPP in the ^{31}P NMR spectrum confirms complete substitution (Figure 3.5.(b)).

Poly[bis(4-carboxyphenoxy)phosphazene] (PCPP) was prepared via the hydrolysis of the ethoxycarbonyl group of PEPP under basic conditions (Figure 3.4.(b)), the success of which was confirmed by NMR and FT-IR spectroscopy (Figure 3.6 and 3.7). In the FT-IR spectra, a broad peak originating from the carboxylic acid group appeared at 2500 cm^{-1} and the carbonyl peak shifted from 1713 cm^{-1} to 1689 cm^{-1} after the hydrolysis reaction. [42] The two carboxylic acid groups per repeating unit of PCPP can form strong hydrogen bonds with the silanol groups on the Si particles, allowing the Si anode to avoid detachment of the binder materials while undergoing large volume change during the charge/discharge cycles.

The thermal transition behavior of PEPP and PCPP was investigated using DSC (Figure 3.8.(a) and (b)). PEPP, which has a semi-crystalline structure induced by its symmetrical side chain, exhibited T_g and T_m values of 12.1 °C and 150.1 °C, respectively. [42] After the hydrolysis reaction, the T_g value of PCPP increased to 56.6 °C, which can be attributed to the strong hydrogen bonding between the carboxylic acid groups. The thermal stability of PEPP and PCPP was investigated using TGA (Figure 3.9). PEPP, which comprises an inorganic backbone (–P=N–), was thermally stable up to a temperature of 250 °C and did not undergo decomposition; however, loss of mass occurred at temperatures above 250 °C because of the decomposition of the organic side groups. In the case of PCPP, loss of mass began in a lower temperature range (150–200 °C) because of the anhydride groups that formed by dehydration between two carboxylic acid groups. [47, 48]

Preparation of the aqueous binder solution and the properties of the binder materials containing PCPP and PEG-NH_3 (PCG-X)

Because PCPP is not soluble in aqueous media by itself, it was neutralized using NH_4OH (28.0 wt% NH_3 aqueous solution); after neutralization, PCPP-NH_3 dissolved well in water owing to the formation of an ammonium carboxylate group. The aqueous binder solution was prepared by mixing the PCPP-NH_3 and PEG-NH_3 solutions at different weight ratios (Table 3.1 and

Figure 3.3). When the aqueous binder solution containing PCPP-NH_3 and PEG-NH_3 was heated at 80 °C under vacuum, the ammonium carboxylate groups in PCPP-NH_3 changed to carboxylic acid groups, releasing NH_3 gas; this caused the formation of an ionically cross-linked structure (*i*-PCG). [49] When *i*-PCG was further heated to 130 °C under vacuum, water molecules were liberated, causing the ionically cross-linked structure to change into a covalently cross-linked structure (PCG-X) by the formation of an amide group. The same heating process at 80 °C and at 130 °C under vacuum was used to prepare the Si anode.

The formation of ionically and covalently cross-linked structures in *i*-PCG-7.5 and PCG-7.5, respectively, from the addition of 7.5% (w/w) PEG-NH_3 to PCPP-NH_3 was confirmed by FT-IR spectroscopy. In Figure 3.10, the *i*-PCG-7.5 spectrums exhibits a peak at 1536 cm^{-1} corresponding to the carboxylate group, while that of PCG-7.5 exhibits a peak at 1645 cm^{-1} corresponding to the amide group. [4] In addition, the peak at 1713 cm^{-1} that originated from the aromatic ester of PEPP disappeared after the hydrolysis reaction, while a new peak corresponding to aromatic carboxylic acid appeared at 1689 cm^{-1} for PCPP, *i*-PCG-7.5, and PCG-7.5. [42]

The thermal transition behavior and mechanical properties of PCG-Xs were evaluated by DSC and nano-indentation to investigate the properties of the binder materials and elucidate their effects on cell performance (Figure 3.11 and 3.12.(a)). For DSC and nano-indentation analysis, PCG-X films were

prepared by film casting the aqueous binder solutions without adding electrode materials, such as Si particles and Super P, following which heat treatment was conducted first at 80 °C and then at 130 °C under vacuum.

Because the cross-linking density of PCG-Xs increases with increasing PEG-NH_3 content, the glass transition temperature (T_g) and elastic modulus of PCG-Xs also increased as the PEG-NH_3 content increased up to 7.5 wt% (Table 1). [50, 51] However, when the PEG-NH_3 content increased to 10.0 wt%, the T_g and elastic modulus decreased owing to the increased content of the flexible ethylene oxide units. [52] The strong mechanical strength of the polymer binder can be beneficial in improving the cell performance of the Si anode because it can help maintain the polymer structure when the Si particles undergo volume change. [53, 54] Although PCG-7.5 had the highest T_g value of 65.8 °C, there would not be much effect on the cell performance as the difference was less than 4 °C. Furthermore, because PCG-Xs have a cross-linked structure, a small difference in the T_g value does not significantly affect the overall physical properties.

The adhesion properties of the silicon anodes prepared with the PCG-Xs were evaluated using 180° peel test and SAICAS (Figure 3.12.(b) and (c)). The adhesion force of the PCG-Xs also increased with increasing PEG-NH_3 content up to 7.5 wt%, following which it decreased as the PEG-NH_3 content increased to 10.0 wt%; this behavior was observed for T_g and elastic modulus as well. In general, an increase in cross-linking density improves the adhesion

force of the polymers on the substrates by increasing the mechanical strength. [55, 56] Accordingly, when the PEG-NH_3 content increased up to 7.5 wt%, the adhesion forces of the PCG-Xs increased. However, a further increase to 10.0 wt% decreased the adhesion force because although the cross-linking density increased, the concentration of carboxylic acid groups—which have strong binding ability with Si particles—decreased; in addition, the excessively flexible ethylene oxide unit, which does not have strong hydrogen bonding ability and thus decrease the binding strength. Therefore, we confirmed once again that a PEG-NH_3 content of 7.5 wt% is optimal for the Si anode binder to exhibit both the highest adhesion force as well as the highest mechanical strength. Because the highest adhesion force indicates the highest interaction between the binder and Si particles, the cell performance can be improved as the Si-containing electrode structure can be effectively maintained. [57, 58]

Cell Performance

The long-term cycling stability of Si/LE-Celgard/Li cells with different binders (PCG-Xs or PAA) was evaluated at a 0.2 C rate (840 mAh g^{-1}) after two activation cycles at 0.05 C (210 mAh g^{-1}) (Figure 3.13.(a)). The cell with the PCG-7.5 binder exhibited the highest discharge capacity over 300 cycles, followed by the cells with PCG-10, PCG-5, and PCG-2.5 in that order. Owing

to the volume change of Si particles, the better the physical properties of the binder, such as elastic modulus and peel strength, the better the structure of the Si anode is maintained during the charge/discharge process. Among the PCG-Xs, PCG-7.5 had the best physical properties and, as a result, showed the best cell performance. The cell performance results of the other PCG-Xs also coincided with the physical properties of the binders.

In addition, the cell with PCG-7.5 showed better cell performance and rate capability than the cell with PAA, which is a conventional Si anode binder (Figure 3.13.(b)), although the elastic modulus (10.56 GPa) and peeling force (1.21 N) values of PAA were larger than those of PCG-7.5. We believe that the better performance of the cell with PCG-7.5 can be ascribed to (1) the larger chain flexibility of the polyphosphazene backbone, (2) the cross-linked structure of PCG, and (3) enhanced ionic conductivity by the PEG moiety. The polyphosphazene backbone and PEG chain, which are the main polymer structures of PCG-7.5, are very flexible. [31, 32] The T_g values of the polyphosphazene- and PEG-based polymers are therefore much smaller than that of PAA. Accordingly, the T_g value of PCG-7.5 (65.8 °C) was smaller than that of PAA (103 °C), [59] despite PCG-7.5 having a cross-linked structure. The flexibility of PCG-7.5 can also improve the electrochemical kinetics by increasing the free volume [60] and maintain the anode structure by adjusting quickly to the volume change of Si particles. [61] In addition, the cross-linked structure of PCG-7.5 allows the binder structure to be maintained more

effectively than that of PAA (which has a linear structure) when the Si particles are undergoing volume change during charge/discharge cycles. [22] Lastly, the improved ion transport inside the electrode caused by the PEG moieties is the third reason for the excellent electrochemical performance of PCG-7.5. The ionic conductivities of PCG-Xs and PAA are summarized in Table 3.1 and Figure 3.14.(a). It was found that the ionic conductivity of the PCG-Xs increased as the PEG content increased. In addition, all the PCG-Xs had considerably larger ionic conductivity values than PAA; greater ionic conductivity leads to lower internal resistance of the Si anode, which improves cell performance. EIS was performed to investigate the effect of ionic conductivity on the internal resistance of Si half-cells; the resulting Nyquist plots of the half-cells before and after cycling are shown in Figure 3.15. The charge transfer resistance (R_{ct}) values of the Si anode with PCG-7.5 were smaller than those of the Si anode with PAA both before and after cycling, suggesting that PCG-7.5 can improve the ion conduction in the Si anode more than PAA can. CV tests were also conducted to determine the D_{Li^+} of the Si anodes. The CV curves of the half-cells with PAA and PCG-7.5 at different scan rates over the range of 0.1–0.4 mV s^{-1} between voltages of 0.01 and 1.5 V (*vs.* Li/Li^+) were plotted (Figure. 3.16), and D_{Li^+} values were calculated using the Randles–Sevcik equation [6]

$$I_p = 2.69 \times 10^5 n^{1.5} A D_{Li^+}^{0.5} v^{0.5} C_{Li^+}$$

where n is the number of electrons in the redox process (4.4), A is the

anode area (0.95 cm^2), C_{Li^+} is the concentration of lithium ions (0.001 mol cm^{-3}), v is the scan rate, and D_{Li^+} is the diffusion coefficient. Plots of the peak current (I_p) with the square root of the scan rate ($v^{0.5}$) are shown in Figure 3.13.(c). D_{Li^+} values of the Si anodes with PAA and PCG-7.5 were 1.8×10^{-10} cm^2 s^{-1} and 4.3×10^{-10} cm^2 s^{-1}, respectively, which also demonstrates that the PEG moieties in PCG-7.5 improve lithium-ion conduction inside the Si anode.

The surface morphologies of the Si anodes with PAA and PCG-7.5 binders before and after cycling were examined using SEM (Figure 3.17.(a)–(d)). While numerous cracks were generated after 50 cycles on the surface of the Si anode with PAA, the surface of the Si anode with PCG-7.5 was relatively less cracked after cycling, demonstrating that PCG-7.5 can tolerate the huge volume change of Si during charge/discharge cycles; this is attributed to the higher chain flexibility and the cross-linked structure of PCG-7.5. To observe the change in thickness of the Si anodes before and after cycling, FIB-milled cross-sectional SEM images were obtained (Figure 3.17.(e)–(h)). The change in thickness of the Si anode with PAA was 64.4%, whereas that of the anode with PCG-7.5 was 30.8%. This result indicates that PCG-7.5 can withstand the huge volume change of Si better than PAA; this allows for the electrode integrity to be maintained, leading to the formation of a compact and thin SEI layer. [62]

3.4 Conclusion

In this study, cross-linked polymeric binders containing polyphosphazene with carboxylic acid groups (PCPP) and ion-conducting PEG were prepared for application in high-performance lithium-ion battery systems with Si anodes. For the preparation of aqueous binder solutions, the water-insoluble PCPP was neutralized with NH_3-producing water-soluble PCPP-NH_3, and subsequently mixed with poly(ethylene glycol) bisamine (PEG-NH_3); the wt% of PEG-NH_3 to PCPP-NH_3 was varied from 2.5 wt% to 10 wt%. Polyphosphazene binders with cross-linked structures (PCG-Xs, where X indicates the wt% of PEG-NH_3 to PCPP-NH_3) were prepared by covalent bond formation between carboxylic acid and amine groups via thermal treatment during the electrode drying process. PCG-7.5, which contained 7.5 wt% PEG-NH_3, exhibited the highest glass transition temperature, elastic modulus, and peeling force among the PCG-Xs; this is because it had the optimum amount of flexible ion-conducting ethylene oxide and carboxylic acid groups, which resulted in the optimum degree of cross-linking density that imparted the highest thermal transition temperature, mechanical strength, and interactions with Si. Comparing the battery performance of the cell fabricated with PCG-7.5 against that of the cell fabricated with PAA, the cell with PCG-7.5 exhibited better performance owing to the advantageous features of PCG-7.5, including chain flexibility, cross-linked structure, and ionic conductivity. Our results have proved that binders based on flexible

polyphosphazenes and ion-conducting PEG moieties with cross-linked structures can impart Si anodes with high performance when used in LIBs. Further studies optimizing their chemical structures, including cross-linking density, ion-conducting moiety, and hydrogen bonding groups, can improve battery cell performance.

3.5 References

[1] J.W. Choi, D. Aurbach, Promise and reality of post-lithium-ion batteries with high energy densities, Nature Reviews Materials 1(4) (2016) 16013.

[2] J. Chang, Q. Huang, Y. Gao, Z. Zheng, Pathways of Developing High-Energy-Density Flexible Lithium Batteries, Advanced Materials 33(46) (2021) 2004419.

[3] X. Yang, K.R. Adair, X. Gao, X. Sun, Recent advances and perspectives on thin electrolytes for high-energy-density solid-state lithium batteries, Energy & Environmental Science 14(2) (2021) 643-671.

[4] Z. Shi, Q. Liu, Z. Yang, L.A. Robertson, S.R. Bheemireddy, Y. Zhao, Z. Zhang, L. Zhang, A chemical switch enabled autonomous two-stage crosslinking polymeric binder for high performance silicon anodes, Journal of Materials Chemistry A 10(3) (2022) 1380-1389.

[5] A. Gupta, R. Badam, N. Matsumi, Heavy-Duty Performance from Silicon Anodes Using Poly(BIAN)/Poly(acrylic acid)-Based Self-Healing Composite Binder in Lithium-Ion Secondary Batteries, ACS Applied Energy Materials 5(7) (2022) 7977-7987.

[6] H. Liu, Q. Wu, X. Guan, M. Liu, F. Wang, R. Li, J. Xu, Ionically Conductive Self-Healing Polymer Binders with Poly(ether-thioureas) Segments for High-Performance Silicon Anodes in Lithium-Ion Batteries, ACS Applied Energy Materials 5(4) (2022) 4934-4944.

[7] S. Ko, M.-J. Baek, T.-U. Wi, J. Kim, C. Park, D. Lim, S.J. Yeom, K. Bayramova, H.Y. Lim, S.K. Kwak, S.W. Lee, S. Jin, D.W. Lee, H.-W. Lee, Understanding the Role of a Water-Soluble Catechol-Functionalized Binder for Silicon Anodes by Diverse In Situ Analyses, ACS Materials Letters 4(5) (2022) 831-839.

[8] P. Luo, P. Lai, Y. Huang, Y. Yuan, J. Wen, C. Xie, J. Li, L. Liu, A Highly Stretchable and Self-Healing Composite Binder Based on the Hydrogen-Bond Network for Silicon Anodes in High-Energy-Density Lithium-Ion Batteries, ChemElectroChem 9(12) (2022) e202200155.

[9] Z. Song, T. Zhang, L. Wang, Y. Zhao, Z. Li, M. Zhang, K. Wang, S. Xue, J. Fang, Y. Ji, F. Pan, L. Yang, Bio-Inspired Binder Design for a Robust Conductive Network in Silicon-Based Anodes, Small Methods 6(5) (2022) 2101591.

[10] X. Li, Y. Xing, J. Xu, Q. Deng, L.-H. Shao, Uniform yolk–shell structured Si–C nanoparticles as a high performance anode material for the Li-ion battery, Chemical Communications 56(3) (2020) 364-367.

[11] N. Liu, J. Liu, D. Jia, Y. Huang, J. Luo, X. Mamat, Y. Yu, Y. Dong, G. Hu, Multi-core yolk-shell like mesoporous double carbon-coated silicon nanoparticles as anode materials for lithium-ion batteries, Energy Storage Materials 18 (2019) 165-173.

[12] D. Kim, T. Ahmed, K. Crossley, J.K. Baldwin, S.H. Ra Shin, Y. Kim, C. Sheehan, N. Li, D.V. Pete, H.H. Han, J. Yoo, A controlled nucleation and

growth of Si nanowires by using a TiN diffusion barrier layer for lithium-ion batteries, Nanoscale Advances 4(8) (2022) 1962-1969.

[13] C. Hwang, K. Lee, H.-D. Um, Y. Lee, K. Seo, H.-K. Song, Conductive and Porous Silicon Nanowire Anodes for Lithium Ion Batteries, Journal of The Electrochemical Society 164(7) (2017) A1564-A1568.

[14] S. Chae, Y. Xu, R. Yi, H.-S. Lim, D. Velickovic, X. Li, Q. Li, C. Wang, J.-G. Zhang, A Micrometer-Sized Silicon/Carbon Composite Anode Synthesized by Impregnation of Petroleum Pitch in Nanoporous Silicon, Advanced Materials 33(40) (2021) 2103095.

[15] Y. An, Y. Tian, C. Liu, S. Xiong, J. Feng, Y. Qian, One-Step, Vacuum-Assisted Construction of Micrometer-Sized Nanoporous Silicon Confined by Uniform Two-Dimensional N-Doped Carbon toward Advanced Li Ion and MXene-Based Li Metal Batteries, ACS Nano 16(3) (2022) 4560-4577.

[16] C. Li, T. Shi, H. Yoshitake, H. Wang, Improved performance in micron-sized silicon anodes by in situ polymerization of acrylic acid-based slurry, Journal of Materials Chemistry A 4(43) (2016) 16982-16991.

[17] H. Wang, B. Wu, X. Wu, Q. Zhuang, T. Liu, Y. Pan, G. Shi, H. Yi, P. Xu, Z. Xiong, S.-L. Chou, B. Wang, Key Factors for Binders to Enhance the Electrochemical Performance of Silicon Anodes through Molecular Design, Small 18(1) (2022) 2101680.

[18] Z. Li, G. Wu, Y. Yang, Z. Wan, X. Zeng, L. Yan, S. Wu, M. Ling, C. Liang, K.N. Hui, Z. Lin, An Ion-Conductive Grafted Polymeric Binder with

Practical Loading for Silicon Anode with High Interfacial Stability in Lithium-Ion Batteries, Advanced Energy Materials 12(29) (2022) 2201197.

[19] H.Y. Ling, C. Wang, Z. Su, S. Chen, H. Chen, S. Qian, D.-S. Li, C. Yan, M. Kiefel, C. Lai, S. Zhang, Amylopectin from Glutinous Rice as a Sustainable Binder for High-Performance Silicon Anodes, ENERGY & ENVIRONMENTAL MATERIALS 4(2) (2021) 263-268.

[20] W. Huang, W. Wang, Y. Wang, Q. Qu, C. Jin, H. Zheng, Overcoming the fundamental challenge of PVDF binder use with silicon anodes with a super-molecular nano-layer, Journal of Materials Chemistry A 9(3) (2021) 1541-1551.

[21] A. Magasinski, B. Zdyrko, I. Kovalenko, B. Hertzberg, R. Burtovyy, C.F. Huebner, T.F. Fuller, I. Luzinov, G. Yushin, Toward Efficient Binders for Li-Ion Battery Si-Based Anodes: Polyacrylic Acid, ACS Applied Materials & Interfaces 2(11) (2010) 3004-3010.

[22] Z. Zheng, H. Gao, C. Ke, M. Li, Y. Cheng, D.-L. Peng, Q. Zhang, M.-S. Wang, Constructing Robust Cross-Linked Binder Networks for Silicon Anodes with Improved Lithium Storage Performance, ACS Applied Materials & Interfaces 13(45) (2021) 53818-53828.

[23] Y.K. Jeong, T.-w. Kwon, I. Lee, T.-S. Kim, A. Coskun, J.W. Choi, Millipede-inspired structural design principle for high performance polysaccharide binders in silicon anodes, Energy & Environmental Science 8(4) (2015) 1224-1230.

[24] I. Kovalenko, B. Zdyrko, A. Magasinski, B. Hertzberg, Z. Milicev, R. Burtovyy, I. Luzinov, G. Yushin, A Major Constituent of Brown Algae for Use in High-Capacity Li-Ion Batteries, Science 334(6052) (2011) 75-79.

[25] S. Guo, H. Li, Y. Li, Y. Han, K. Chen, G. Xu, Y. Zhu, X. Hu, SiO2-Enhanced Structural Stability and Strong Adhesion with a New Binder of Konjac Glucomannan Enables Stable Cycling of Silicon Anodes for Lithium-Ion Batteries, Advanced Energy Materials 8(24) (2018) 1800434.

[26] Z.H. Xie, M.Z. Rong, M.Q. Zhang, Dynamically Cross-Linked Polymeric Binder-Made Durable Silicon Anode of a Wide Operating Temperature Li-Ion Battery, ACS Applied Materials & Interfaces 13(24) (2021) 28737-28748.

[27] R. Guo, S. Zhang, H. Ying, W. Yang, J. Wang, W. Han, Preparation of an Amorphous Cross-Linked Binder for Silicon Anodes, ChemSusChem 12(21) (2019) 4838-4845.

[28] J. Liu, Q. Zhang, T. Zhang, J.-T. Li, L. Huang, S.-G. Sun, A Robust Ion-Conductive Biopolymer as a Binder for Si Anodes of Lithium-Ion Batteries, Advanced Functional Materials 25(23) (2015) 3599-3605.

[29] W. Zeng, L. Wang, X. Peng, T. Liu, Y. Jiang, F. Qin, L. Hu, P.K. Chu, K. Huo, Y. Zhou, Enhanced Ion Conductivity in Conducting Polymer Binder for High-Performance Silicon Anodes in Advanced Lithium-Ion Batteries, Advanced Energy Materials 8(11) (2018) 1702314.

[30] S. Rothemund, I. Teasdale, Preparation of polyphosphazenes: a tutorial

review, Chemical Society Reviews 45(19) (2016) 5200-5215.

[31] K.S. Ogueri, K.S. Ogueri, H.R. Allcock, C.T. Laurencin, Polyphosphazene polymers: The next generation of biomaterials for regenerative engineering and therapeutic drug delivery, Journal of Vacuum Science & Technology B 38(3) (2020) 030801.

[32] Z. Tian, A. Hess, C.R. Fellin, H. Nulwala, H.R. Allcock, Phosphazene High Polymers and Models with Cyclic Aliphatic Side Groups: New Structure–Property Relationships, Macromolecules 48(13) (2015) 4301-4311.

[33] H.R. Allcock, R.L. Kugel, Synthesis of High Polymeric Alkoxy- and Aryloxyphosphonitriles, Journal of the American Chemical Society 87(18) (1965) 4216-4217.

[34] H.R. Allcock, D.C. Ngo, Synthesis of poly[bis(phosphazo)phosphazenes] bearing aryloxy and alkoxy side groups, Macromolecules 25(11) (1992) 2802-2810.

[35] A. Singh, N.R. Krogman, S. Sethuraman, L.S. Nair, J.L. Sturgeon, P.W. Brown, C.T. Laurencin, H.R. Allcock, Effect of Side Group Chemistry on the Properties of Biodegradable l-Alanine Cosubstituted Polyphosphazenes, Biomacromolecules 7(3) (2006) 914-918.

[36] S. Jankowsky, M.M. Hiller, H.D. Wiemhöfer, Preparation and electrochemical performance of polyphosphazene based salt-in-polymer electrolyte membranes for lithium ion batteries, Journal of Power Sources 253 (2014) 256-262.

[37] S. Jankowsky, M.M. Hiller, R. Stolina, H.D. Wiemhöfer, Performance of polyphosphazene based gel polymer electrolytes in combination with lithium metal anodes, Journal of Power Sources 273 (2015) 574-579.

[38] S. Yeşilot, S. Küçükköylü, T. Mutlu, R. Demir-Cakan, Halogen-Free Polyphosphazene-Based Flame Retardant Cathode Materials for Li–S Batteries, Energy Technology 9(12) (2021) 2100563.

[39] S. Yeşilot, F. Hacıvelioğlu, S. Küçükköylü, K.B. Çelik, G. Sayan, R. Demir-Cakan, Design, Synthesis, and Characterization of Polyphosphazene Bearing Stable Nitroxide Radicals as Cathode-Active Materials in Li-Ion Batteries, Macromolecular Chemistry and Physics 218(17) (2017) 1700051.

[40] P. Chen, Z. Wu, T. Guo, Y. Zhou, M. Liu, X. Xia, J. Sun, L. Lu, X. Ouyang, X. Wang, Y. Fu, J. Zhu, Strong Chemical Interaction between Lithium Polysulfides and Flame-Retardant Polyphosphazene for Lithium–Sulfur Batteries with Enhanced Safety and Electrochemical Performance, Advanced Materials 33(9) (2021) 2007549.

[41] A.N. Mujumdar, S.G. Young, R.L. Merker, J.H. Magill, A study of solution polymerization of polyphosphazenes, Macromolecules 23(1) (1990) 14-21.

[42] H.R. Allcock, S. Kwon, An ionically crosslinkable polyphosphazene: poly[bis(carboxylatophenoxy)phosphazene] and its hydrogels and membranes, Macromolecules 22(1) (1989) 75-79.

[43] D. Chen, M. Song, M. Zhu, T. Zhu, P. Kang, X. Yang, G. Sui, Highly

Elastic and Polar Block Polymer Binder Enabling Accommodation of Volume Change and Confinement of Polysulfide for High-Performance Lithium–Sulfur Batteries, ACS Applied Energy Materials 5(4) (2022) 5287-5295.

[44] A.K. Andrianov, A. Marin, J. Chen, J. Sargent, N. Corbett, Novel Route to Sulfonated Polyphosphazenes: Single-Step Synthesis Using "Noncovalent Protection" of Sulfonic Acid Functionality, Macromolecules 37(11) (2004) 4075-4080.

[45] B. Hu, S. Jiang, I.A. Shkrob, S. Zhang, J. Zhang, Z. Zhang, L. Zhang, Poly(4-vinylbenzoic acid): A Re-Engineered Binder for Improved Performance from Water-Free Slurry Processing for Silicon Graphite Composite Electrodes, ACS Applied Energy Materials 2(9) (2019) 6348-6354.

[46] X. Tao, J. Wang, C. Liu, H. Wang, H. Yao, G. Zheng, Z.W. Seh, Q. Cai, W. Li, G. Zhou, C. Zu, Y. Cui, Balancing surface adsorption and diffusion of lithium-polysulfides on nonconductive oxides for lithium–sulfur battery design, Nature Communications 7(1) (2016) 11203.

[47] P.L. Nayak, K. Yang, P.K. Dhal, S. Alva, J. Kumar, S.K. Tripathy, Polyelectrolyte-Containing Fullerene I: Synthesis and Characterization of the Copolymers of 4-Vinylbenzoic Acid with C60, Chemistry of Materials 10(8) (1998) 2058-2066.

[48] A.S. Abreu, M. Oliveira, P.V. Rodrigues, I. Moura, G. Botelho, A.V. Machado, Synthesis and characterization of polystyrene-block-poly(vinylbenzoic acid): a promising compound for manipulating

photoresponsive properties at the nanoscale, Journal of Materials Science 50(7) (2015) 2788-2796.

[49] Z. Shi, S. Jiang, L.A. Robertson, Y. Zhao, E. Sarnello, T. Li, W. Chen, Z. Zhang, L. Zhang, Restorable Neutralization of Poly(acrylic acid) Binders toward Balanced Processing Properties and Cycling Performance for Silicon Anodes in Lithium-Ion Batteries, ACS Applied Materials & Interfaces 12(52) (2020) 57932-57940.

[50] M.C. Montoya-Ospina, H. Verhoogt, M. Ordner, X. Tan, T.A. Osswald, Effect of cross-linking on the mechanical properties, degree of crystallinity and thermal stability of polyethylene vitrimers, Polymer Engineering & Science n/a(n/a) (2022).

[51] A. Mujtaba, M. Keller, S. Ilisch, H.J. Radusch, T. Thurn-Albrecht, K. Saalwächter, M. Beiner, Mechanical Properties and Cross-Link Density of Styrene–Butadiene Model Composites Containing Fillers with Bimodal Particle Size Distribution, Macromolecules 45(16) (2012) 6504-6515.

[52] L.E. Nielsen, Cross-Linking–Effect on Physical Properties of Polymers, Journal of Macromolecular Science, Part C 3(1) (1969) 69-103.

[53] Y.-M. Zhao, F.-S. Yue, S.-C. Li, Y. Zhang, Z.-R. Tian, Q. Xu, S. Xin, Y.-G. Guo, Advances of polymer binders for silicon-based anodes in high energy density lithium-ion batteries, InfoMat 3(5) (2021) 460-501.

[54] H. Chen, Z. Wu, Z. Su, S. Chen, C. Yan, M. Al-Mamun, Y. Tang, S. Zhang, A mechanically robust self-healing binder for silicon anode in lithium

ion batteries, Nano Energy 81 (2021) 105654.

[55] J. He, C. Das, F. Yang, J. Maibach, Crosslinked poly(acrylic acid) enhances adhesion and electrochemical performance of Si anodes in Li-ion batteries, Electrochimica Acta 411 (2022) 140038.

[56] J. Lopez, Z. Chen, C. Wang, S.C. Andrews, Y. Cui, Z. Bao, The Effects of Cross-Linking in a Supramolecular Binder on Cycle Life in Silicon Microparticle Anodes, ACS Applied Materials & Interfaces 8(3) (2016) 2318-2324.

[57] L. Wei, C. Chen, Z. Hou, H. Wei, Poly (acrylic acid sodium) grafted carboxymethyl cellulose as a high performance polymer binder for silicon anode in lithium ion batteries, Scientific Reports 6(1) (2016) 19583.

[58] R. Tang, L. Ma, Y. Zhang, X. Zheng, Y. Shi, X. Zeng, X. Wang, L. Wei, A Flexible and Conductive Binder with Strong Adhesion for High Performance Silicon-Based Lithium-Ion Battery Anode, ChemElectroChem 7(9) (2020) 1992-2000.

[59] A. Eisenberg, T. Yokoyama, E. Sambalido, Dehydration kinetics and glass transition of poly(acrylic acid), Journal of Polymer Science Part A-1: Polymer Chemistry 7(7) (1969) 1717-1728.

[60] G. Zhu, Y. Gu, Y. Wang, G. Liu, V.S. Battaglia, Q. Qu, H. Zheng, Suppressing the dry bed-lake fracture of silicon anode via dispersant modification in electrode processing, Electrochimica Acta 319 (2019) 682-689.

[61] C. Chen, F. Chen, L. Liu, J. Zhao, F. Wang, Cross-linked hyperbranched polyethylenimine as an efficient multidimensional binder for silicon anodes in lithium-ion batteries, Electrochimica Acta 326 (2019) 134964.

[62] L. Han, T. Liu, O. Sheng, Y. Liu, Y. Wang, J. Nai, L. Zhang, X. Tao, Undervalued Roles of Binder in Modulating Solid Electrolyte Interphase Formation of Silicon-Based Anode Materials, ACS Applied Materials & Interfaces 13(38) (2021) 45139-45148.

Table 3.1. Preparation of aqueous binder solutions and properties of the binder materials (PCG-Xs)

PCG-Xs	Weight ratio [a]			Properties			
	PCPP	NH_3[b]	PEG-NH_3	T_g (°C)	σ[c] (S cm^{-1})	Elastic modulus[d] (GPa)	Peeling Force[e] (N)
PCG-2.5	89.9	10.1	2.5	62.1	9.9×10^{-4}	5.46	0.22
PCG-5	89.9	10.1	5.0	63.4	1.0×10^{-3}	6.04	0.42
PCG-7.5	89.9	10.1	7.5	65.8	1.1×10^{-3}	6.45	0.80
PCG-10	89.9	10.1	10.0	63.3	1.1×10^{-3}	6.41	0.60

[a]For the preparation of aqueous binder solution.

[b]Equimolar amounts of NH_3 to carboxylic acid in PCPP were used, where NH_4OH is a 28 wt% aqueous solution of NH_3.

[c]Measured at 25 °C after soaking with liquid electrolyte.

[d]Measured after solution casting followed by heat treatment at 130 °C under vacuum.

[e]Measured using Si anode dried under vacuum at 130 °C.

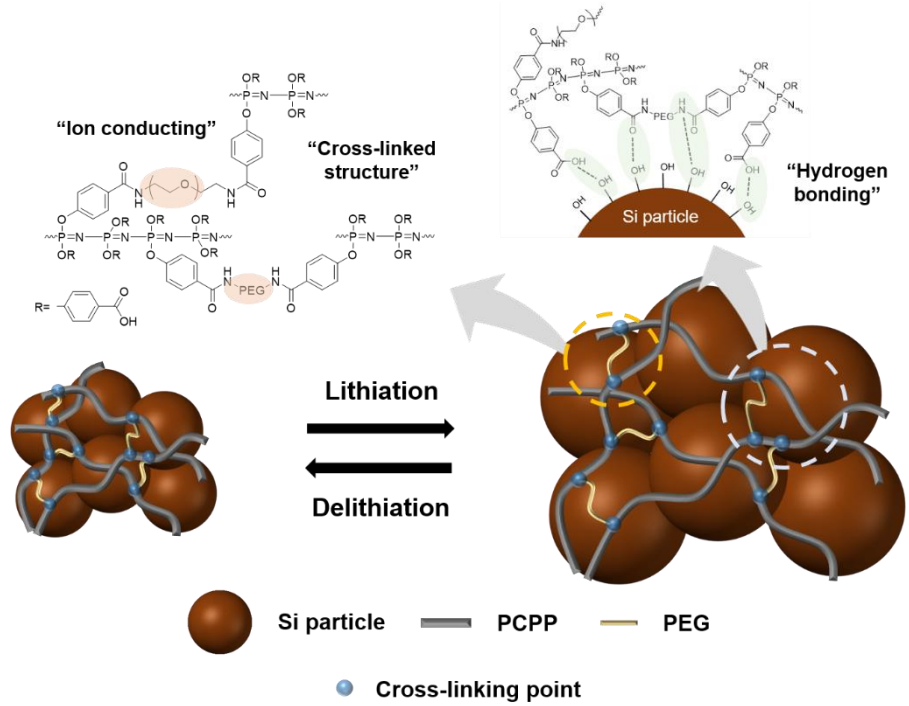

Figure 3.1. The illustration for lithiation/delithiation of Si anode with ion-conducting cross-linked poly[bis(4-carboxyphenoxy)phosphazene] binder.

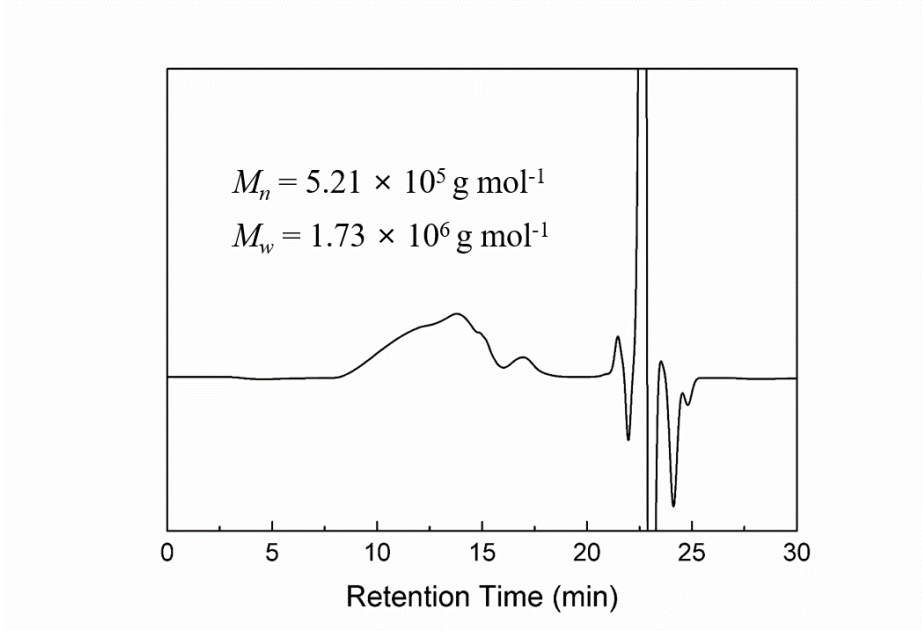

Figure 3.2. GPC profile of PEPP.

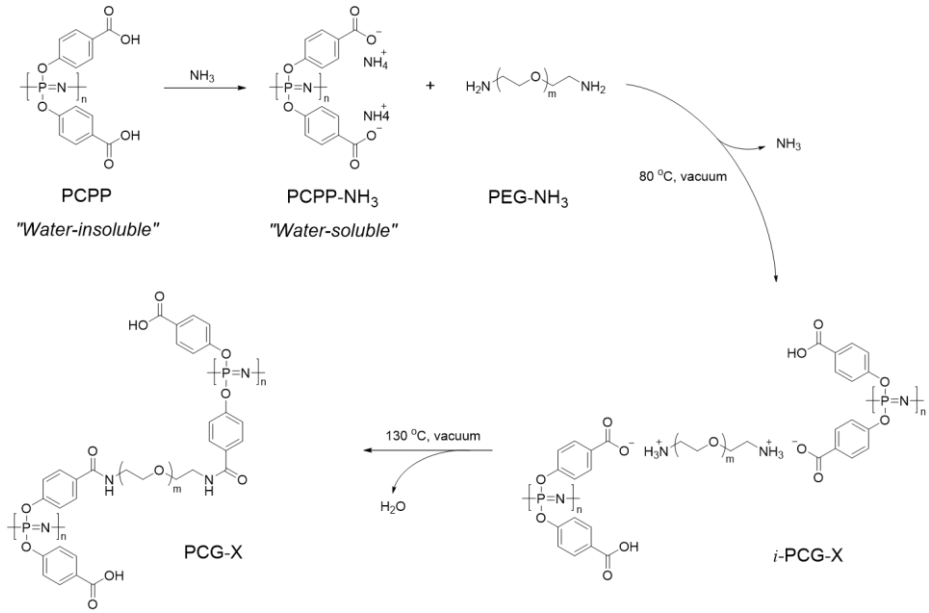

Figure 3.3. Schematic illustration for the preparation of binder solution and the formation of binders with cross-linked structures (PCG-Xs).

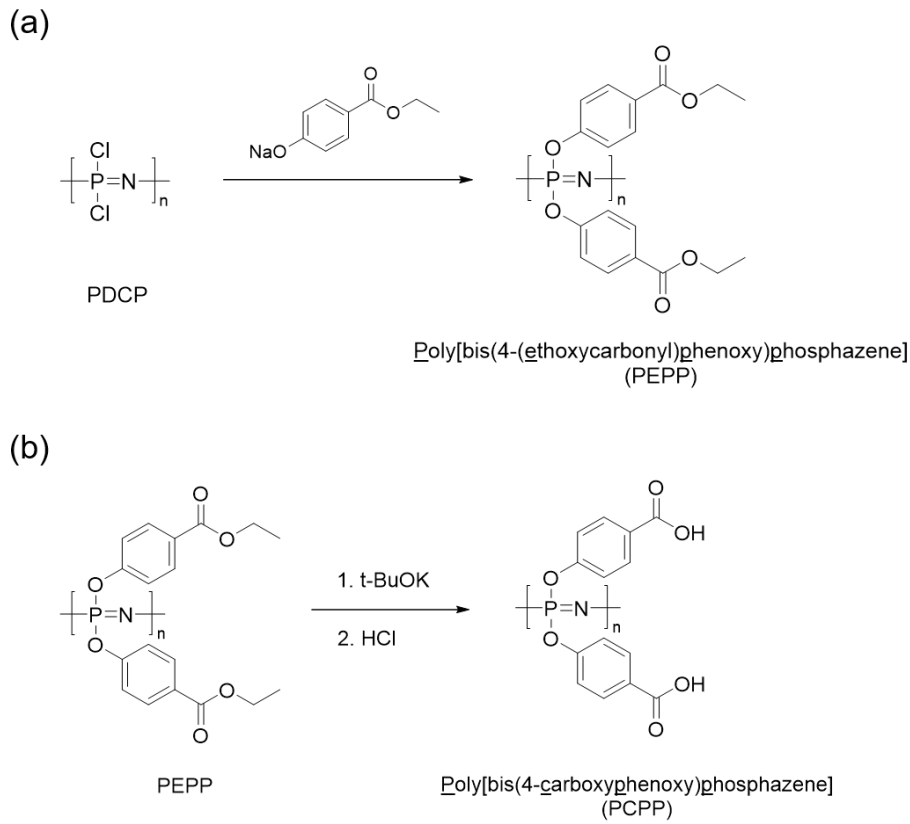

Figure 3.4. Synthetic scheme of (a) PEPP and (b) PCPP.

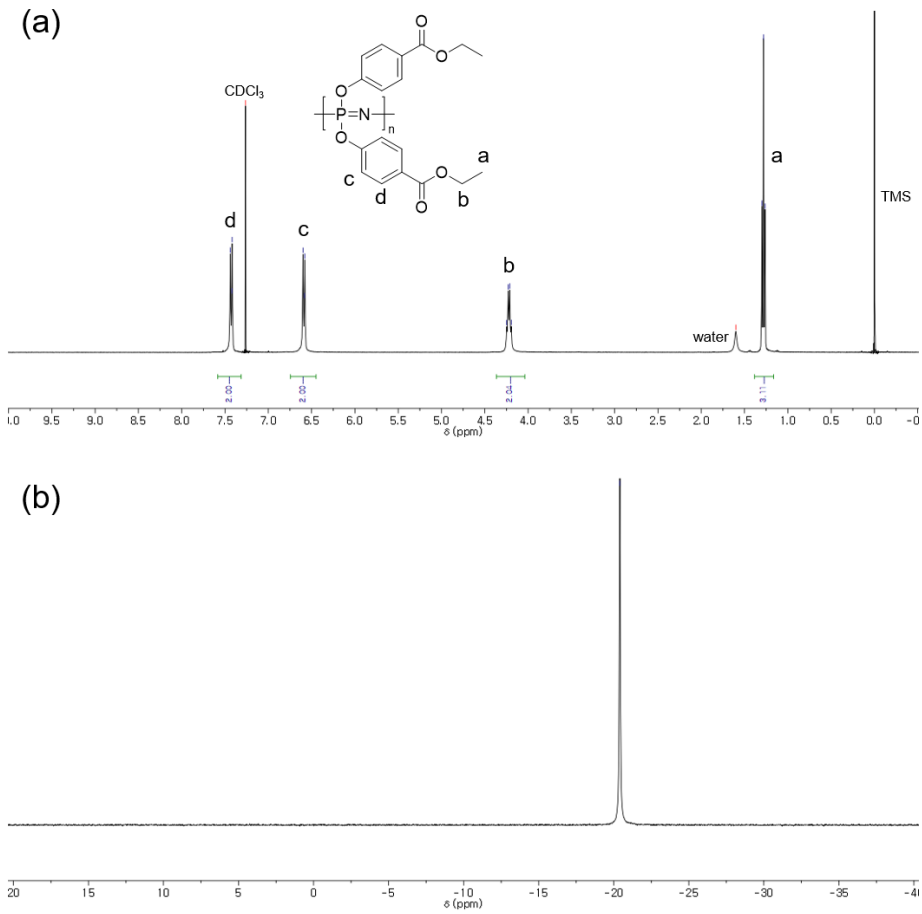

Figure 3.5. (a) ^{1}H NMR spectrum and (b) ^{31}P NMR spectrum of PEPP.

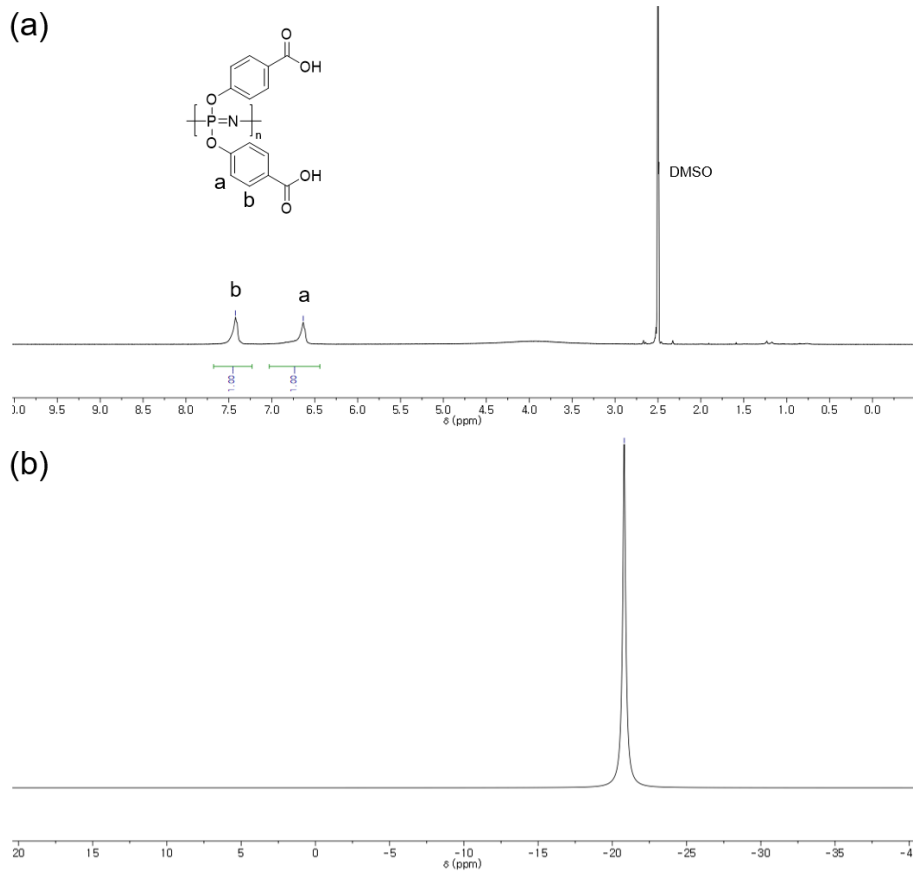

Figure 3.6. (a) ^{1}H NMR spectrum and (b) ^{31}P NMR spectrum of PCPP.

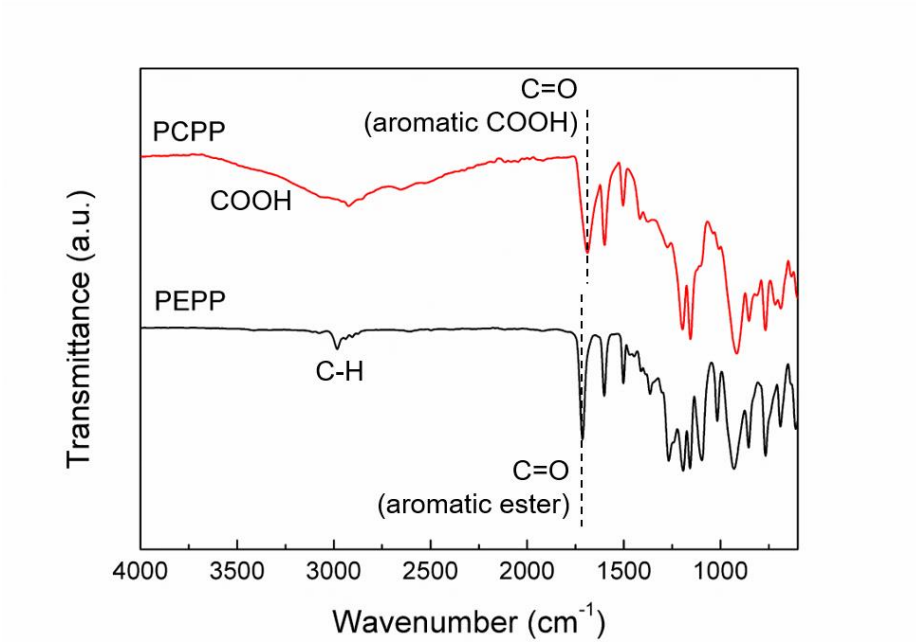

Figure 3.7. FT-IR spectra of PEPP and PCPP in the range of 4000–600 cm^{-1}.

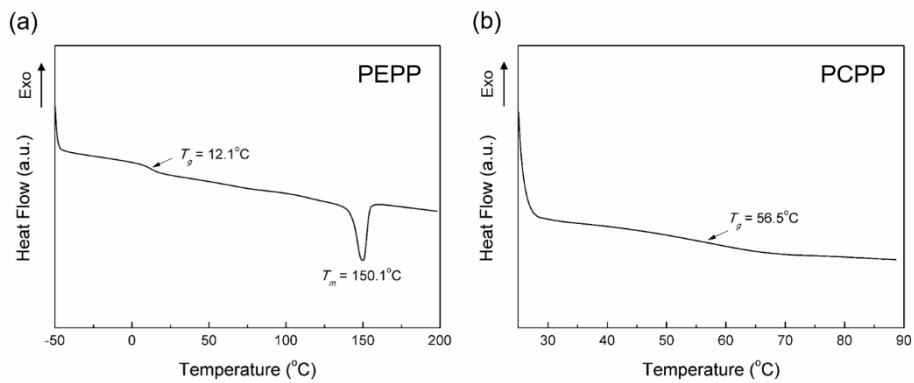

Figure 3.8. DSC thermograms of (a) PEPP and (b) PCPP.

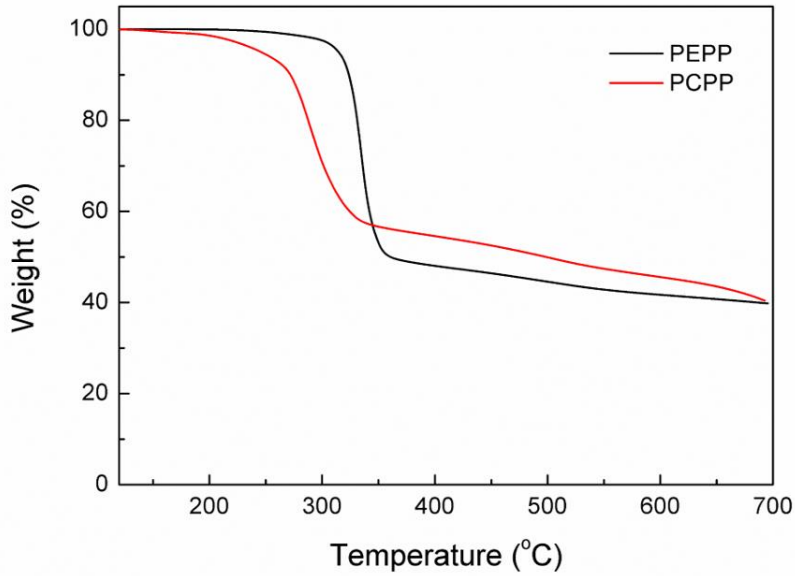

Figure 3.9. TGA curves of PEPP and PCPP.

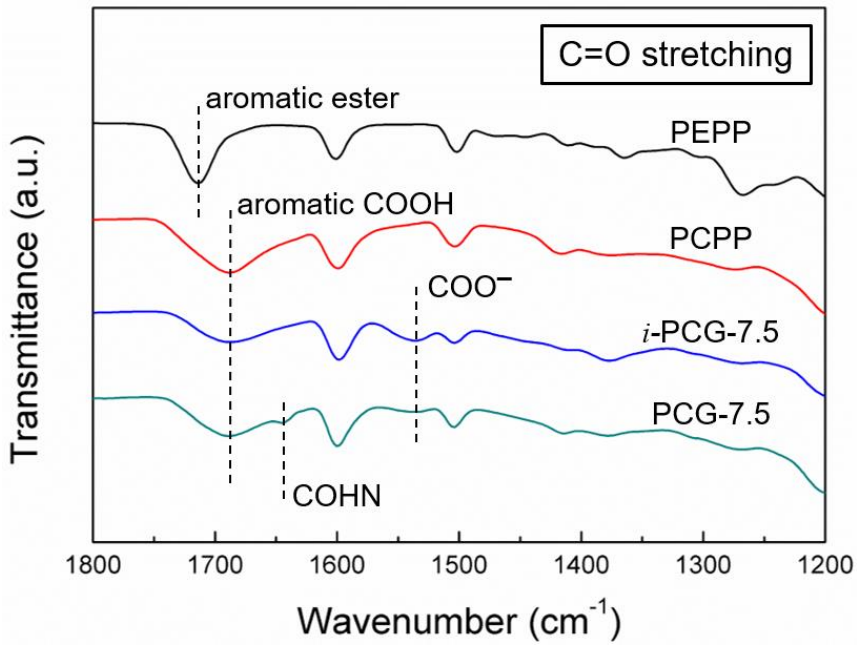

Figure 3.10. FT-IR spectra of PEPP, PCPP, *i*-PCG-7.5, and PCG-7.5 in the range of 1800–1200 cm^{-1}.

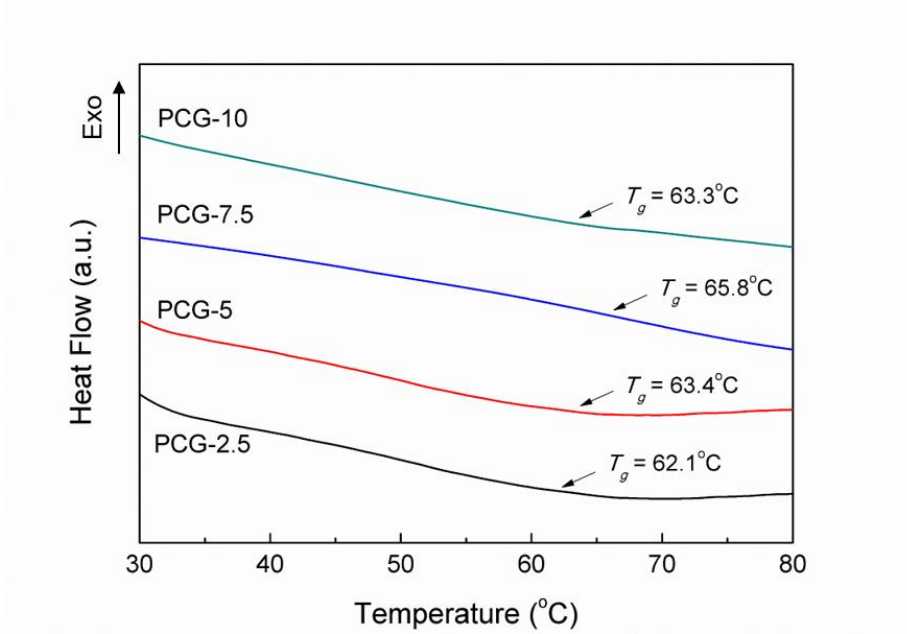

Figure 3.11. DSC thermograms of PCG-Xs.

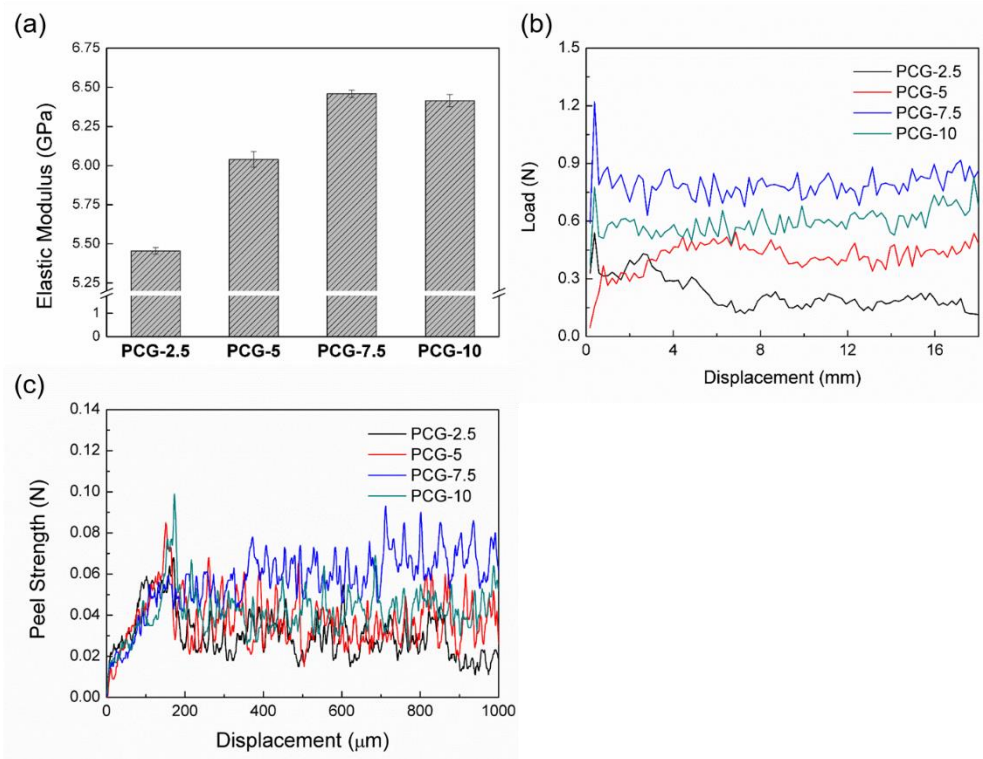

Figure 3.12. (a) Elastic moduli of PCG-Xs. (b) Load–displacement curves and (c) SAICAS data of Si anodes with PCG-Xs.

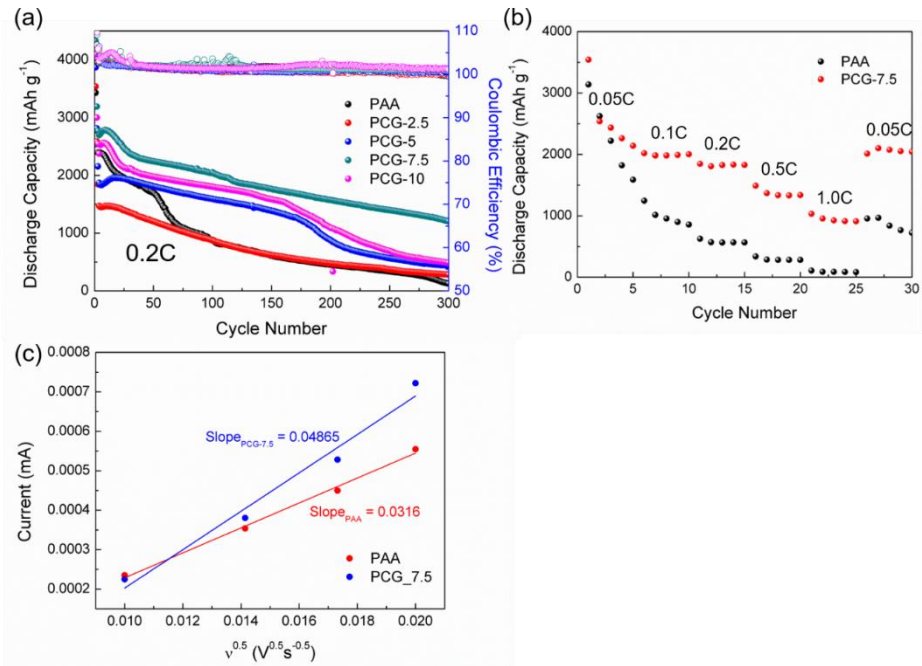

Figure 3.13. (a) Specific discharge capacity of the Si half-cells with PCG-Xs and PAA binders cycled at a rate of 0.2 C after two activation cycles at 0.05 C. (b) Rate capability test of cells with PCG-7.5 and PAA binders. (c) Linear fits for the cathodic peak currents versus the square root of the scan rates for anodes with PCG-7.5 and PAA binders.

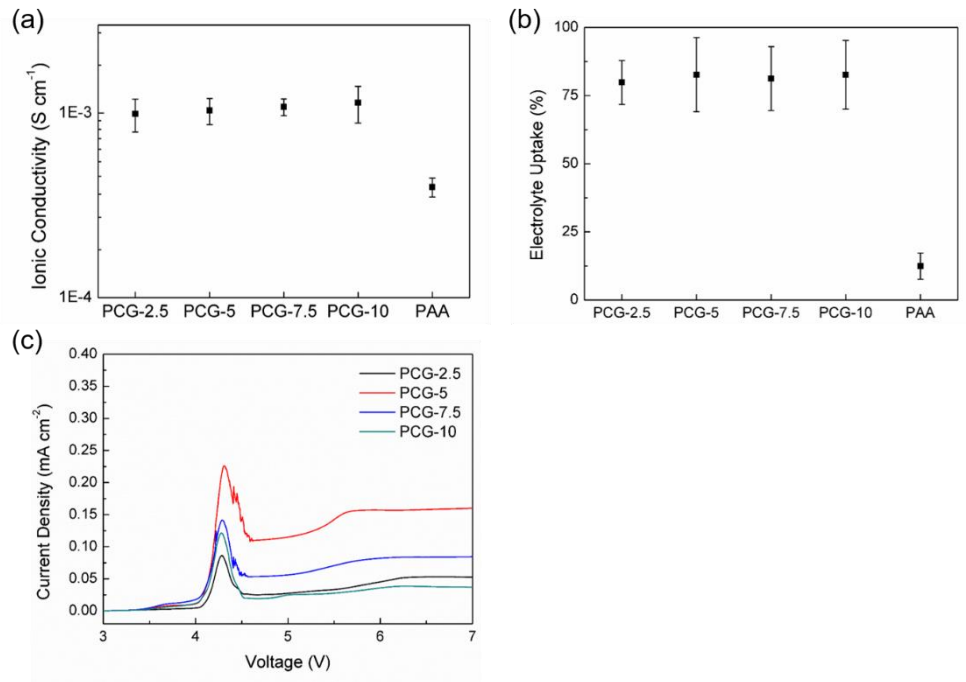

Figure 3.14. (a) Ionic conductivities and (b) electrolyte uptake of PCG-Xs and PAA at 25 °C. (c) Electrochemical stability of PCG-Xs at 25 °C.

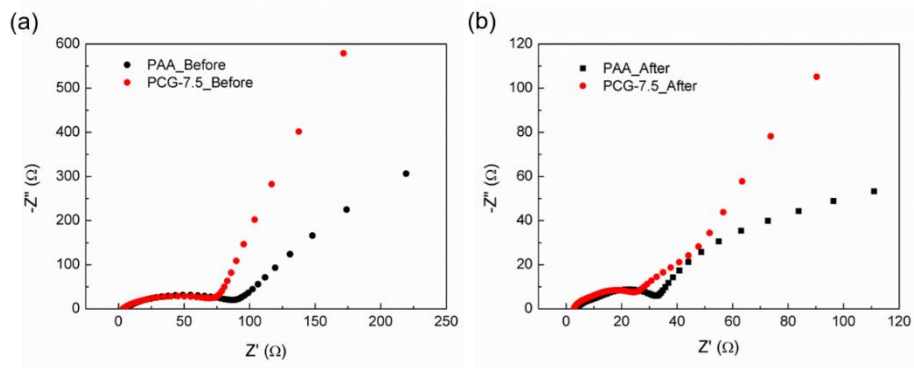

Figure 3.15. Nyquist plots of the cells with Si anode using PAA and PCG-7.5 binders (a) before and (b) after cycling.

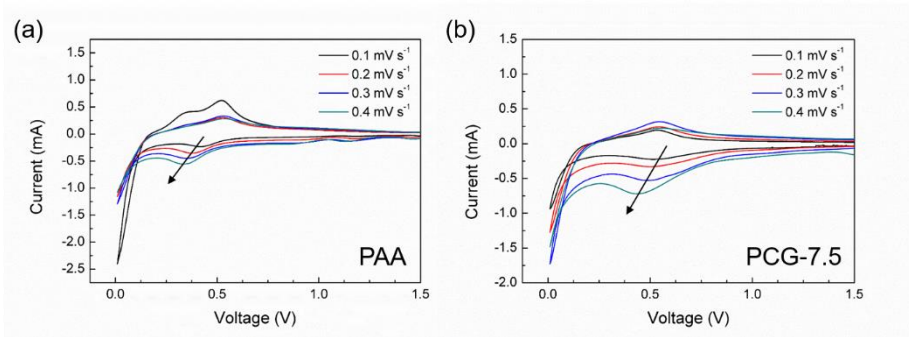

Figure 3.16. Cyclic voltammetry curves of the cells with Si anode using (a) PAA and (b) PCG-7.5 binders at different scan rates.

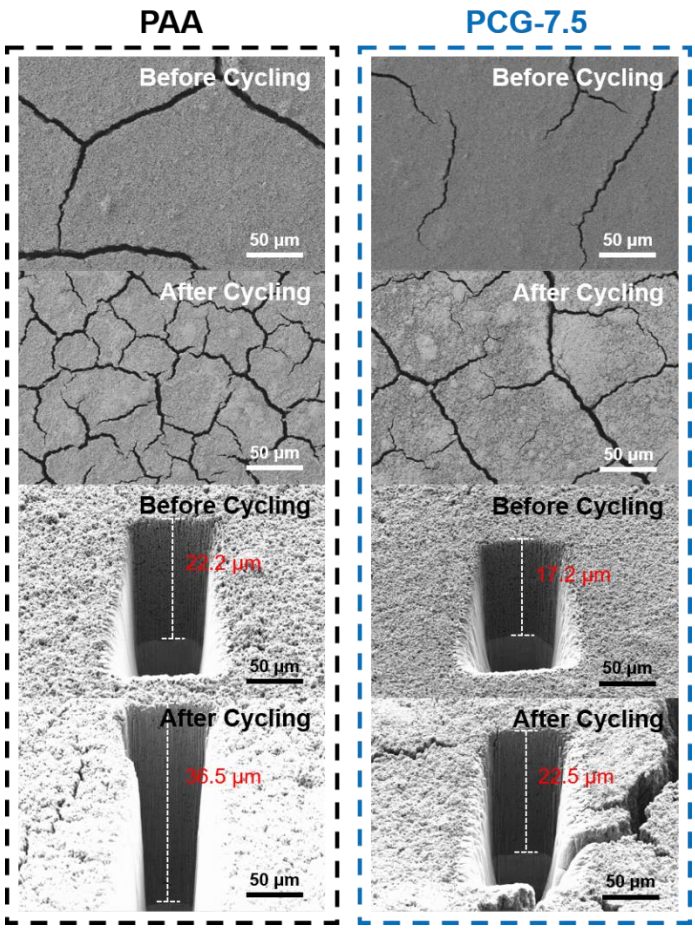

Figure 3.17. Top-view SEM images of Si anodes with (a) PAA and (b) PCG-7.5 binders before cycling. Top-view SEM images of Si anodes with (c) PAA and (d) PCG-7.5 binders after 50 cycles. Cross-sectional SEM images of Si anodes with (e) PAA and (f) PCG-7.5 binders before cycling. Cross-sectional SEM images of Si anodes with (g) PAA and (h) PCG-7.5 binders after 50 cycles.

초 록

본 연구에서는 이온 전도성을 갖는 가교 고분자 재료의 합성과 분석, 그리고 리튬 이차 전지 전해질 및 바인더로의 응용에 대하여 기술하였다. 첫째, 이온 전도성 poly(ethylene glycol) (PEG), 유연한 폴리 실록산, 그리고 음이온 포착성 붕소 가교제 (BPC) 간의 싸이올-이중결합 클릭 반응을 통하여 리튬 금속 전지의 가교된 고체 고분자 전해질 (SPE)을 제조하였다. BPC 함량에 따른 SPE의 다양한 열 및 전기화학적 성질을 체계적으로 분석하였다. 가교 구조에 의해 열적으로 안정한 SPE를 얻을 수 있음과 동시에, 유연한 폴리실록산의 도입으로 60° C 에서 1.3×10^{-4} S cm^{-1} 의 비교적 높은 이온 전도도를 얻을 수 있었다. BPC에 포함된 붕소 작용기는 붕소 원자의 음이온 포착 능력으로 인해 붕소를 포함하지 않는 SPE와 비교하여 리튬 이온 운반율을 높일 수 있었다. SPE의 음이온 포착 능력과 기계적으로 안정한 가교 구조에 의해 리튬 덴드라이트의 형성 및 성장이 효과적으로 억제되

었다.

둘째, 가교된 폴리포스파젠 기반 고분자 재료는 NH_3 에 의해 중화된 poly[bis(4-carboxyphenoxy)phosphazene] (PCPP-NH_3) 를 가교제인 poly(ethylene glycol) bisamine (PEG-NH_3)으로 가교하여 제조하였으며, 이를 리튬 이온 전지의 규소 음극 바인더로 사용하였다. 최적 비율의 PEG-NH_3 (7.5 wt% of PCPP-NH_3) 가교제를 갖는 가교 폴리포스파젠은 가장 높은 유리 전이 온도, 탄성 모듈러스, 접착력 값을 보여주었다. 이러한 가교 폴리포스파젠 기반 바인더로 제조된 규소 음극을 갖는 전지의 전지 성능이 PAA 바인더를 활용한 규소 음극을 갖는 전지보다 더 우수함을 확인할 수 있었다. 폴리포스파젠 바인더를 갖는 전지의 우수한 성능은 유연한 폴리포스파젠 주쇄, 카복시산 기의 수소결합 능력, 가교 구조에 따른 전지 구동 과정에서의 전극 구조 유지 등과 같은 바인더 재료의 성분 및 구조에 의한 것이라 할 수 있다. 더욱이, 이온전도성 PEG는 규소 음극 내부에서의 이온 전도도를 더 높여주었다.

주요어: 가교 고분자, 고체 고분자 전해질, 음이온 포착, 규소 음극 바인더, 폴리포스파젠, 리튬 금속 전지, 리튬 이온 전지

학번: 2017-27567 성명: 홍동기